SELF REPAIR IN A ZEBRAFISH MODEL FOR SLOW-CHANNEL MYASTHENIC SYNDROME

By

Michael D. Walogorsky

A Dissertation

Presented to

the Program in Neuroscience

and

Oregon Health and Science University
School of Medicine

in partial fulfillment of the requirements for the degree of

Doctor of Philosophy

April 2012

School of Medicine

Oregon Health and Science University

We, the dissertation committee, hereby certify that the Ph.D. dissertation of

Michael D. Walogorsky

has been approved

_____

Paul Brehm, Ph.D., Senior Scientist, Dissertation Advisor
Vollum Institute for Advanced Biomedical Research

_____

Laurence Trussell, Ph.D., Senior Scientist, Dissertation Chairman
Vollum Institute for Advanced Biomedical Research

_____

Gail Mandel, Ph.D., Senior Scientist
Vollum Institute for Advanced Biomedical Research

_____

James Maylie, Ph.D., Professor
Department of Obstetrics & Gynecology

TABLE OF CONTENTS

ABSTRACT

Slow channel syndrome (SCS) is a congenital form of myasthenia resulting from point mutations in muscle nicotinic acetylcholine receptor (AChR) subunits. These mutations prolong the open duration of the AChR, and consequently increase the decay time constant of endplate currents. Clinically, SCS is characterized in patients by muscle weakness and fatigue, muscle degeneration and endplate myopathy. Although symptoms can be managed with pharmaceutical interventions, there is currently no cure for this progressively debilitating disease.

The zebrafish motility mutant *twister* carries a point mutation in the alpha (α) subunit of the AChR that recapitulates both the aberrant single receptor properties and compromised voluntary movement seen in humans. Unlike the human condition, however, symptoms manifest transiently, and animals undergo a homeostatic recovery process that renders them asymptomatic for the remainder of their lifespan. The goal of this dissertation work is to progress our understanding of the pathogenesis of SCS by examining the consequences of the mutation in zebrafish and uncover the mechanism of this recovery process.

Electrophysiological recording of synaptic currents during the period of compromised motility reveals that two unique kinetic components are introduced to the decay process. Addition of these two components results in persistent current entry and maintained muscle depolarization, preventing the cell from following the high-frequency trains of action potentials necessary for swimming. These components, termed intermediate and slow, have time constants that are approximately 10-and 100-fold

longer than those recorded at wild-type neuromuscular junctions. The molecular basis for these two components was determined by reconstitution of single AChRs. These studies revealed that the gating of the embryonic AChR isoform accounts for the slow kinetic component; gating of the adult AChR isoform underlies the intermediate component. Additionally, both receptor subtypes displayed an increased apparent affinity to acetylcholine, and significant numbers of spontaneous openings were observed in the embryonic form.

Recovery from SCS, and improvement of swimming function in zebrafish occurs through the natural developmental switch from the embryonic (γ) to the adult (ε) subunit. Reducing the fraction of embryonic AChRs at the synapse effectively accelerates synaptic current decay and allows the muscle cell to follow high-frequency trains of action potentials. When γ-subunit translation was blocked using morpholinos, the recovery process was accelerated, supporting the finding that the embryonic subunit is responsible for the motility defect. This distinction makes *twister* both a genetic model for SCS and a functional model for Escobar Syndrome, a myasthenic syndrome resulting from mutations in the γ-subunit. Although gene knockdown technology was effective in the zebrafish, it has limited application in humans. Therefore, we tested quinidine, a long-lived open-channel blocker currently administered to human patients. These studies demonstrated that quinidine improved neuromuscular function in zebrafish as well. We further demonstrate that the mode of quinidine action is an acceleration of synaptic current decay to near wild type levels. Additionally, quinidine was shown to be an effective blocker of the persistently open embryonic AChR.

ACKNOWLEDGEMENTS

I would like to express my gratitude to those individuals whose sacrifice, patience, hard work and understanding helped to bring this study to its present format. First, to my mentor, Paul Brehm, I have derived many years of first-class entertainment during my time in your lab and I will miss the daily discussions and sense of humor that you bring every day. I am grateful for the constant guidance, encouragement and advice both within the laboratory and for navigating the world outside of science. I would consider myself lucky to have a scientific career that mirrors yours.

To the members of the Brehm lab, colleagues, and classmates, I would like to thank you for the constant discussions that have influenced my life in ways that you may never know, but in a way I will always be grateful for.

To my parents, Rosemary and Leo and to my brother Tom, I want to thank you for the years of support and constant encouragement, the perspective you helped bring to my graduate career and the sacrifices you made so that I could realize this goal.

And finally, to Becky, my wife, life-long collaborator and best friend, my heartfelt thanks for your endless patience and dedication to making this project and also my life a success. I am grateful for your decision to not only marry me, but to work alongside me as well.

LIST OF FIGURES

CHAPTER I

General Introduction

Slow Channel Syndrome is a congenital myasthenic syndrome

Congenital myasthenic syndromes are inherited disorders that result from mutations in proteins essential for neuromuscular transmission. These are rare disorders that occur in approximately 1-2 million births. Genetic mutations that alter receptor structure and functionally enhance its opening are further classified as slow channel syndrome (SCS). Currently, 25 kinships harboring SCS mutations in each of the AChR subunits have been identified (Figure 1.1; Engel et al., 1993; Ohno et al., 1995; Sine et al., 1995; Engel et al., 1996; Gomez et al., 1996; Milone et al., 1997; Reviewed in Engel 2003). Many of these mutations are located in or near the pore forming domains, a key functional region for the AChR (Engel et al., 2003). Due to the gain of function nature of these mutations, the syndrome generally exhibits dominant inheritance, but occasional recessive inheritance has also been documented (Croxen, 2002). In heterozygous carriers, SCS is characterized clinically by skeletal muscle fatigue and progressive weakening, often accompanied by muscle atrophy (Engel et al., 1982). The extraocular muscles, as well as the muscles of the face and forelimb are often affected (Engel et al., 1982; Oosterhuis 1987).

Structural damage is observed at the neuromuscular junction of SCS carriers. This is often characterized by a loss of the post-synaptic folds, reduced density of post-synaptic receptors, widening of the synaptic cleft, an accumulation of debris within the

Figure 1.1. The location of human Slow Channel Syndrome and Escobar Syndrome mutations:

Schematic of individual acetylcholine receptor subunits showing the locations of single nucleotide polymorphisms identified in human patients afflicted with slow channel syndrome (red dots) and the zebrafish L258P mutation (red asterisk). Mutations causal to slow channel syndrome are located in the α, β, δ and ε subunits while mutations found in the γ subunit are causal to Escobar syndrome. SCS mutations are most commonly located in two functional domains, the ligand binding pocket (green ovals) and the M2 transmembrane alpha helix, which makes the major contribution ion conducting pore (orange ovals). Currently, no mutations have been identified in the M2 domain of the γ subunit.

(Adapted from Engel et al, 2003 and Hoffman et al. 2006)

Figure 1.1

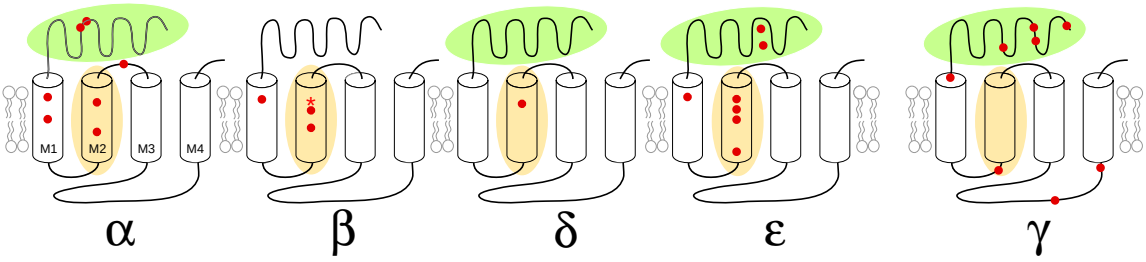

cleft, deterioration of the basement membrane, and degenerating nuclei and mitochondria (Engel et al., 1982; Gomez et al., 1996; Gomez et al., 2002). Motor endplate degeneration is attributed to calcium overload in the sarcoplasm and the subsequent activation of calcium activated proteases (Gomez et al., 1996, Gomez et al., 2002, Groshong 2007). The loss of structural integrity leads to impaired synaptic transmission and reduces the efficiency of neuromuscular communication.

The pathogenesis of SCS depends, to some extent, on the particular mutation found within the kinship. As a result, there is a wide range for both onset time and severity of symptoms, which makes this disease difficult to diagnose clinically (Reviewed in Engel et al., 2003). Currently there is no cure for SCS, but effective therapies have been administered to human patients, and generally, these are well tolerated. Surprisingly, while the efficacy of these therapies is known, their mode of action had not been demonstrated before this present study.

Progress in SCS research

Due to the limited ability to perform electrophysiological studies on human SCS muscle tissue, most of the mechanistic information about SCS-causing mutations derives from expressing the mutant channels in heterologous cells and recording single-channel currents. Indeed, there have been many very high-quality structure-function studies that have revealed both the diverse molecular basis for SCS, as well as the role of specific amino acid residues in conferring receptor function (Sine et al., 1995, Wang et al., 1997; reviewed in Engel et al., 2003). Most importantly, these studies have led to an

effective therapy, in the form of long-lived open-channel blockers, which are currently used to treat human patients. One of these blockers, quinidine sulfate, is commonly prescribed to SCS patients due to its ability to attenuate the prolonged burst-duration of single receptors and its presumed ability to attenuate prolonged synaptic currents (Harper and Engel, 1998; Fukudome et al., 1998). This treatment would reduce cationic overload and calcium entry into the muscle cell, two presumed underpinnings of the myopathy. Although much progress has been made in uncovering the pathogenesis of SCS, the manifestations of these mutations directly on synaptic transmission are largely unknown. This is due to the technical difficulties associated with voltage-clamp of mammalian muscle and the fact that afflicted muscle is obtained through biopsy (Sine et al., 1995; Ohno et al., 1996). This block has impeded further progress in understanding the basis of the syndrome, and in particular the physiological consequences at the synapse.

Advantages of the zebrafish SCS model system

Using the zebrafish model, we have been able to circumvent several technical limitations to achieve a better understanding of the physiological effects of SCS mutation. First, zebrafish muscle cells are electrically compact and amenable to voltage-clamp using a single electrode in the patch configuration. Second, we are able to record from muscle cells from the intact zebrafish with little-to-no disturbance of innervation or connection with other muscle cells. Third, our studies and others have demonstrated that synaptic transmission at zebrafish NMJ is characterized by large quantal size (mEPC

~500pA), but a small quantal content, yielding a favorable signal-to-noise ratio, which allows for excellent resolution of synaptic current decays. Fourth, recording from the intact preparation makes it possible to perform paired motorneuron muscle recordings in living animals (Wen and Brehm, 2005), and allows, for the first time, simultaneous examination of the consequences of an SCS mutation on pre-and post-synaptic function.

Other advantages of the zebrafish model have also contributed to the success of this research; unlike the murine model of SCS, which relies on the overexpression of a transgene (Gomez et al., 1996), the *twister* mutant α-subunit expression is controlled via native regulatory mechanisms. Zebrafish are able to survive for several days without muscle function, making them well suited for experiments designed to reduce or alter neuromuscular transmission (Westerfield et al., 1990; Ono et al., 2001). Importantly, since the publication of the Lefebvre study (Lefebvre et al., 2004), each of the individual ACh receptor subunits have been molecularly cloned, allowing the heterologous reconstitution of ACh receptors for single-channel analysis (Mongeon et. al., 2011). Finally, RNA knockdown has proven to be a successful molecular technique to assess the specific contribution of ACh subunits to synaptic function in embryonic zebrafish (Westerfield et al., 1990; Ono et al., 2001; Mongeon et al., 2011)

Twister as a model for SCS

Twister was identified in a screen for dominant mutations affecting locomotor behavior (van Eeden et al., 1999). Unlike wild-type siblings, heterozygous carriers for the *twister* allele (*twi* $^{+/-}$) are unable to perform coordinated swimming behaviors during

early developmental stages (Figure 1.2, top panel). Instead, movement during the first 24-48 hours after fertilization is restricted to spontaneous sustained unilateral contractions of the axial musculature. When stimulated by electrical or tactile means, animals are unable to mount effective escape behaviors and are largely immotile during this developmental window.

The initial characterization of the *twister* mutant was published through a collaboration between the Brehm and Granato labs (Lefebvre et al., 2004). Morphological examination of *twister* muscle cells using antibody staining against muscle myosin as well as electron microscopy revealed that the severity of the *twister* phenotype is dependent on the inherited number of *twister* alleles (Lefebvre et al., 2004). Homozygous larvae (*twi* $^{-/-}$) exhibited the severest pathology, and showed signs of disrupted myofiber organization and muscular deterioration very early in development (Lefebvre et al., 2004). These animals were rendered paralytic throughout their extremely short lifespan, typically less than 7 days (168 hpf). In heterozygous animals, however, the key anatomical features of muscle cells remained largely intact, but muscle fiber organization and ultrastructure was more disorganized when compared to wild type (Lefebvre et al., 2004).

Positional mapping revealed that the *twister* allele contained a point mutation in the α-subunit of the nicotinic acetylcholine receptor (Lefebvre et al., 2004). The result is a leucine-to-proline substitution of residue 258, a highly conserved pore lining amino acid. The nature of the amino acid substitution suggested that the motility defects and the muscle degeneration might have been direct consequences of disrupted muscle

Figure 1.2: Stimulus induced escape response in *twi* $^{+/-}$ and wild-type zebrafish: 100 ms of stimulus induced swimming behavior is shown for 48 hpf (top) and 120 hpf (bottom) animals. In 48 hpf wild-type zebrafish, swimming is initiated with a powerful musculature contraction followed by alternating contractions of the axial musculature. At the same age, swimming in *twi* $^{+/-}$ is limited to a single prolonged contraction. By 120 hpf, both *twi* $^{+/-}$ and wild-type animals can perform alternating muscular contractions and the swimming behavior in *twi* $^{+/-}$ is indistinguishable from the wild-type animals.

Figure 1.2

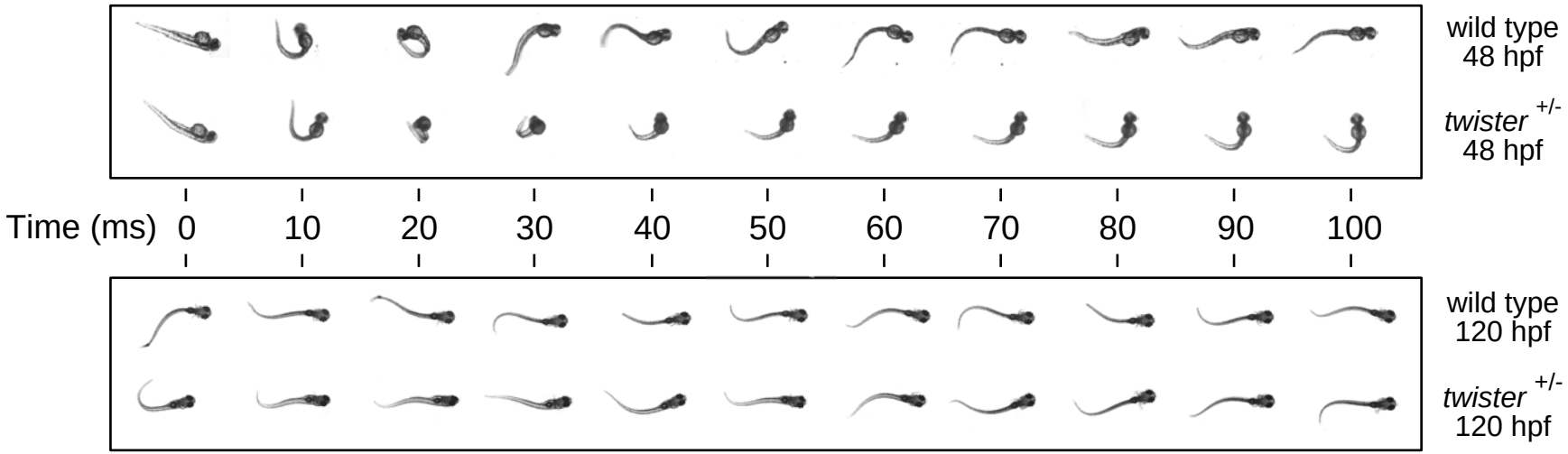
wild type
48 hpf
twister +/-
48 hpf
Time (ms) 0 10 20 30 40 50 60 70 80 90 100
wild type
120 hpf
twister +/-
120 hpf

AChR channel function. Blocking neuromuscular activity with the irreversible AChR antagonist α-bungarotoxin (α-BTX) was sufficient to rescue the structural defects seen in homozygous muscle at 24 hpf, supporting the idea that increased AChR activity is causal to the muscular degeneration and altered motility (Lefebvre et al., 2004).

Whole-cell recording from 72 hpf *twi* $^{+/-}$ muscle cells revealed that the synaptic current duration was greatly prolonged (Lefebvre et al., 2004). When muscle cells were directly stimulated at frequencies similar to those achieved during swimming, end-plate currents summated, resulting in maintained depolarization and prolonged current entry into the muscle cell (Lefebvre et al., 2004). While this research suggested that *twister* is both a genetic and behavioral animal model for SCS, these findings represented the extent of our molecular and electrophysiological understanding of *twister* when I initiated my studies.

Twister recovery process

I felt that the homeostatic recovery process was the most remarkable aspect of the *twister* model, yet this aspect of the zebrafish was underrepresented in the Lefebvre study. Starting at the third day after fertilization (72 hpf) animals can, for the first time, respond to touch with bilateral contractions and can use these small undulatory movements to generate locomotion. Coordination steadily improves throughout the next two days of development until ~120 hpf when *twi* $^{+/-}$ larvae fully recover the ability to perform both escape responses and swimming behaviors similar to their wild type counterparts (Figure 1.2, bottom panel). Beyond this initial 120-hour developmental

period, *twister* ceases to be a motility mutant, displays a normal lifespan, and is otherwise indistinguishable from wild type.

This *twister* SCS model exhibits a unique recovery process not previously reported in any case of human SCS. We had no understanding of the inherent recovery process that the animal underwent, and it raised the possibility that it represents an unappreciated aspect of SCS. Uncovering the mechanism of this recovery process had the potential to both further the basic understanding of nerve-muscle function, and also to identify a new course of intervention for the human condition.

Using the combination of electrophysiological and molecular biology tools available in the Brehm-Mandel labs, I undertook the experiments presented herein to address several outstanding questions: What changes underlie the "self-healing" process, considering that the *twister* mutation is present throughout the lifetime of the animal? Why does the developmental progression of SCS in zebrafish appear to follow the opposite time course observed in humans and mice with similar mutations? What can we learn about the mechanisms of dysfunction and subsequent recovery in zebrafish SCS that can be applied to the human condition? Gaining insight into these questions provided the impetus for the studies presented throughout the remaining chapters of this thesis, and provided a broad platform for training during my graduate career.

CHAPTER II

Materials & Methods

Zebrafish animal care

All experiments utilized zebrafish (*Danio rerio*) as the animal model system. The wild type (WT) and mutant lines were maintained in an OHSU approved facility, in accordance with the standards set forth in the International Animal Care and Use Committee. The methods used were consistent with the Panel on Euthanasia of the American Veterinary Facility. The motility mutant *twister* line carries the formal nomenclature of *nic1*$^{\text{twister dbn12}}$ (Lefebvre et al., 2004), but for the purposes of the present study will be referred to as either *twi* $^{-/-}$ for homozygous carriers or *twi* $^{+/-}$ for heterozygous carriers. Animals of either sex were used for all experiments.

Whole-cell recordings from zebrafish muscle

Preparation

Zebrafish embryos between the ages of 48 and 120 hours post fertilization (hpf) were prepared for all whole-cell voltage-clamp recording from muscle cells. Embryos were decapitated just rostral to the pec-fin segment, and the tail portion was pinned to a recording chamber with fine tungsten wire directly through the notochord. The skin on the topside of the tail was removed between the two pins using fine forceps. To inhibit muscle contraction, preparations were immersed in 1:10 V/V formamide in bath

recording solution for ~ 2 min, and then rinsed extensively. Bath recording solution contained, in mM: 135 NaCl, 10 mM Na-HEPES, 3 mM KCl, 2 mM $CaCl_2$ and 1 mM $MgCl_2$, pH 7.4 and 278 mOsm. 1μM tetrodotoxin was added for spontaneous synaptic current recordings. Unless otherwise noted, chemicals were purchased from Sigma-Aldrich (St Louis, MO).

Recording and data acquisition

Glass recording pipettes (1.5 mm; World Precision Instruments, Sarasota, FL) were pulled to a short taper and a tip inner diameter measuring approximately 3-4 um. For whole-cell recordings, pipettes were filled with a solution containing in mM: 120 KCl, 10 KHEPES, and 5 BAPTA, pH 7.4 and osmolarity was increased to ~278 mOsm with sorbitol. Electrodes generally had tip resistances between 1.8-3 MOhms.

Synaptic currents were recorded using a HEKA Instruments EPC-10/2 amplifier using Pulse or Patchmaster acquisition software (Instrutech Corp., Bellmore, NY). Data was acquired at 100 kHz, and initially filtered at 8.3 kHz with an analog Bessel filter. All muscle cells were held at -90mV. Once in the whole-cell configuration, series resistance estimates were generally between 3-6 MΩ. Series resistance was not compensated, because the voltage error (estimated by $I*R_s$ = 1 nA * 6 MΩ = 6 mV) was ~5%. The time constant of the patch clamp (τ) was estimated by $\tau=R_s*C$ = 6 MΩ * 59 pF = 354 μs. A second method for estimating τ was performed by fitting the transient due to cell capacitance in response to a 10 mV rectangular input with a duration of 20 ms. By this procedure, τ was estimated to be 408.5± 122.8 μs (n=4).

Muscle cells recordings usually lasted 3-10 minutes after entering the whole-cell configuration. As the recordings continued, muscle cell membranes demonstrated a tendency to seal-over the tip of the patch pipette. This manifested as a time dependent decrease in miniature amplitude, concurrent with a slowing of both rise and decay times. Only synaptic events exhibiting stable and fast rise times were considered for analysis, and recordings exhibiting time-dependent changes were not included.

Synaptic event analysis

Raw data was exported from Pulse and individual spontaneous synaptic currents were detected using the Mini Analysis software (Synaptosoft, Decatur, GA). After event detection, current kinetics were extracted by fitting IGOR software (Wavemetrics, Lake Oswego, OR). In IGOR, decay constants were determined by the exponential fit over the entire decay amplitude (peak to end fitting). Data was reported as mean $\pm$ standard deviation, and data sets were compared using a two-tailed Student's t-test to determine significance. For both single-channel and synaptic recordings the overall mean ± standard deviation was computed on the basis of the mean value for individual recordings. The *n* values refer to the number of recordings and the range of events used to compute the means are presented in the figure legends. The methods for paired motorneuron-muscle recording were identical to those previously published (Wen and Brehm, 2005).

On-cell single-channel recordings from zebrafish muscle

Preparation

Preparation of the embryonic fish for on-cell muscle recordings was similar as described for whole-cell recordings. Sometimes, when muscle cells failed to provide high-quality seals, tails were treated with 1X trypsin EDTA for ~1 min, to help clean the muscle cell surface. This treatment helped produce high resistance seal formation. For recordings from fast muscle, fish were prepared similarly, and then individual slow muscle cells were removed from entire segments using a large bore pipette (~10 to 20 μm) under gentle suction.

Recording and data acquisition

Single-channel recording electrodes were pulled to a tip diameter of ~1-3 μm, coated with Sylgard elastomer (Dow Corning, Auburn, MI), and lightly fire polished. Pipettes were filled with bath solution and different concentrations of ACh as indicated. Single-channel recordings were made in the on-cell configuration using an Axopatch 200B amplifier (Molecular Devices, Sunnyvale, CA). Pulse software was used for all single-channel data acquisition at a sampling rate of 100 kHz, and low-pass filtered at 10 kHz with a Bessel analog filter. Single-channel recordings were generally acquired in thirty-second segments at every 10 mV over a range of applied potential between +150 and -100 mV.

Single-channel event analysis

Raw data were imported into TAC software (Bruxton Corporation, Seattle, WA) for event detection, and digitally filtered at 5 kHz. Event detection was undertaken separately for each membrane potential. Recordings often contained more than one amplitude class, but in all cases, event duration was measured at half amplitude. Detected events were exported to TACFIT software (Bruxton Corporation, Seattle, WA) for analysis.

Visual inspection of the relationship between event amplitude and duration was used to determine the minimum duration cutoff for a single opening. The amplitude of events with durations below ~150 μs was typically decreased, reflecting the limitations of the equipment in fully resolving the amplitude of very brief events. The value of 200 μs was used in all recordings as the lower-duration limit for all single-channel analysis, representing the minimum duration for which the event amplitude was fully resolved. The event amplitude was determined by the difference between the baseline (closed) and first level (open) values, and simultaneous openings by multiple-channels were not included in analysis. Amplitude histograms were constructed and fit with a Gaussian function to determine the mean amplitude of the events. Each amplitude class was fit individually with a single Gaussian function.

The burst-duration histograms were constructed and fit in TAC by the method described in Sigworth and Sine, 1987. The burst-duration histogram for each amplitude class was analyzed separately by first separating the individual amplitude classes. The

peak of the transformed exponential fit of each duration histogram provided the mean as determined by the method of maximum likelihood.

Analysis values determined by TACFIT were exported, and data plots were constructed using either IGOR or Microsoft Excel software. Data plots were fit by regression analysis in Excel or IGOR. Data values were reported as mean ± standard deviation, and data sets were compared using a two-tailed Student's t-test to determine significance.

Heterologous expression of reconstituted AChRs

RNA preparation and injection

Stocks of 1 μg/μL RNA were generated for each subunit (mMESSAGE machine, Invitrogen, Carlsbad, CA). RNA stock aliquots were mixed in the combinations indicated for each experiment just prior to injection. The *Xenopus laevis* oocytes were generously provided by Dr. David Dawson. Oocytes were stored in OR3 solution (50% Leibowitz media, 15 mM Na-HEPES, 1 mg/mL gentamycin, pH 7.6) and stage VI and V oocytes were prepared for injection by manual removal of the follicle cell layers. Finely tapered glass injection pipettes were broken to a tip outer diameter of ~10-15 μm, and filled with RNA combinations. Individual oocytes were injected (Drummond Nanoject, Broomall, PA) with ~36 ng of total RNA.

Two-electrode voltage-clamp current analysis

Two-to-five days after RNA injection, oocytes were tested for responsiveness to ACh using two-electrode voltage-clamp measurements. Finely tapered glass recording electrodes were filled with 3 M KCl, and current responses were obtained using the TEV200 amplifier (Dagan Instruments, Minneapolis, MN) and recorded with Pulse acquisition software. A specially designed chamber allowed measurements of ACh-activated current by switching perfusion between bath solution and bath solution containing 30 μM ACh. Three consecutive applications of ACh were examined to determine the amplitude of the maximum current response. The ACh was applied at a flow rate that resulted in complete exchange within 2 seconds. The dose-response curves for each isoform were fit by the Hill equation using IGOR Pro 5.05 (Paradiso and Brehm, 1998). Quinidine sulfate, choline chloride and d-tubocurare were all obtained from Sigma Chemical (St. Louis, MO) and made fresh in recording solution prior to each experiment. Alpha-bungarotoxin was obtained from Molecular Probes (Eugene, OR).

Single-channel recordings from oocytes

Oocytes were prepared as described for macroscopic recordings, except that just before use the vitelline membrane was removed manually in the manner described by Mishina et al, 1986. A specially designed apparatus allowed the oocyte to rest in one well, while a newly formed outside-out patch was brought to a separate well for perfusion with bath solution containing different concentrations of ACh, as indicated.

Single-channel event acquisition and analysis

Single-channel data was acquired using an Axopatch 200B amplifier, and Pulse software. Data analysis methods were the same as described for the on-cell single-channel recordings of muscle.

Quantitative real-time polymerase chain reaction (qPCR)

Whole-fish qPCR

Total RNA was extracted from pools of 20 zebrafish embryos/larvae (for each time point, 24, 48, 72, 144, and 192 hpf) using RNeasy mini kit (Qiagen, Germantown, MD). Total RNA was DNAse treated with TURBO DNAse. Treated RNA was then reverse transcribed using High Capacity cDNA Reverse Transcription kit (Applied Biosystems, Foster City, CA). First strand was used as a template for subsequent qPCR.

Transcript quantity was measured using the StepOnePlus system (Applied Biosystems, Foster City, CA). Amplification of transcripts was detected by the fluorescence of sequence-specific probes (Taqman technology, Invitrogen, Carlsbad, CA). The sequences of the primers and probes used for each transcript are as follows:

SUBUNIT	SENSE PRIMER	PROBE	ANTISENSE PRIMER
γ	agtggcgctctatgctaacacact	aagctcctgcgccatcaaagtcaact	tgctgcaattctgccagtcaaagg
ε	Dr03115283_g1	gcacactggtcttcaggtctcagac	
elf1a	ttgatgcccttgatgccattctgc	attggaactgtacctgtgggtcgtgt	acaaccataccaggcttgaggaca

Whole Fish qPCR transcript quantification

Absolute transcript copy numbers were determined using the standard curve method. Quantification of known amounts of target DNA was used to establish a comparative for unknown transcript levels of specific subunits at various developmental stages (24, 48, 72, 144, and 192 hpf). From the standard curve quantification of the transcript number was determined. Numbers were normalized to the endogenous control elongation factor1 1-alpha (elf1-a) to account for variations in concentration (quantity) of starting template. E1f1-a has been previously characterized as a transcript expressed at constant levels throughout the developing zebrafish embryos (Tang et al, 2007). This normalization generates a ΔCt value ($Ct_{Experimental}$-Ct_{e1f1a}) and controls for variations in quantity of input material. After normalization, transcript levels were found using the following equation; copy number = $2^{(-\Delta Ct)}$. Experimental variation was measured by calculating the standard deviation (SD) of copy number: SD = $(\ln 2)(stdev_{\Delta Ct})(2^{(-\Delta Ct)})$. To adjust for the variability in overall signal between embryo collections, the copy number for each target was normalized to the total copy number of all targets in each experiment and the relative copy number was reported.

Morpholino RNA knock-down in vivo

Morpholino preparation and design

Morpholinos (GeneTools, Philomath, OR) are modified antisense oligonucleotides designed to anneal to mRNA and interfere with protein synthesis either by directly hindering translation initiation or by causing splicing errors. Morpholinos

(MOs) were designed for each target in accordance with the manufacturer's suggestions. The sequence of the γ subunit morpholino was TAATTAAGGCACATACTCA-CTTCCC. MOs were resuspended in 1 mM stock solutions in water, and 0.5 to 1.5 nL volume droplets were pressure injected into newly fertilized zebrafish eggs at the one or two cell stage. The final amount injected (in ng) was empirically determined the morphology was normal and muscle cells were amenable for recordings. Final amounts ranged between 1 and 12 ng of MO per embryo.

Whole-cell recordings from MO injected fish

Fish were prepared for whole-cell muscle recordings as specified for WT fish. Unless otherwise indicated, whole-cell recordings were performed on the fast and slow muscle of fish between 48 and 54 hours post injection. Recording setup, acquisition parameters and data analysis were all as previously described for WT whole-cell recordings.

Motion Analysis

Fish movements were tracked at 1000 frames per second using a Fastcam 512-PCI camera (Photron Instruments, San Diego, CA) and were quantitated using Flote zebrafish behavioral analysis software (Burgess and Granato, 2007). Escape responses were elicited by a rapid mechanical tap on the recording dish, or an electrical stimulation.

CHAPTER III

Swimming behavior in the *twister* motility mutant

General overview

Zebrafish anatomy

The muscle of the larval zebrafish shares many anatomical and morphological features with other vertebrates, including humans (Lefebvre et al., 2004). In the zebrafish, skeletal muscle cells comprise the bulk of the tail, and the myotome resembles interlocking chevron repeats, with anterior facing points. Each chevron contains two types of skeletal muscle, termed fast and slow, which can be distinguished based on several anatomical and electrophysiological features (reviewed in Sanger and Stoiber, 2001). Slow muscle is mononucleated and forms a superficial monolayer that runs parallel to the axis of the tail (Devoto et al., 1996). It is innervated by secondary motor neurons and generates tension slowly in response to neuronal activity. Also known as slow tonic muscle, it is inexcitable and depends on the depolarization derived from synaptic input for contraction (Buckingham and Ali, 2004). Fast muscle cells comprise the deeper layers of the myotome. In contrast to slow muscle cells, they are multinucleated and oriented obliquely. They are innervated by a primary motor neuron and up to three secondary motor neurons. Also known as fast twitch muscle, these cells are able to generate and propagate sodium action potentials and contract quickly, but are unable to maintain these contractions for extended periods (Ono and Brehm, 2001).

In mammals, tonic muscle has been best described in the extraocular muscles, but is also found in the ear, esophagus and larynx (Hess, 1970). Generally, tonic muscle is more prevalent in non-mammalian vertebrates and is thought to be involved in maintaining posture. Fast twitch muscle in the fish is homologous to human muscle used in sprinting. Fast and slow muscle types are not spatially segregated in most vertebrates, including humans; the distinct layering of the two muscle types in fish provides an advantage for these physiological studies.

Zebrafish locomotion

Zebrafish locomotion is generated through alternating contraction of the axial muscle cells. This rhythmic tail-beat exerts force on surrounding water molecules and determines both the speed and direction of body displacement. Larval zebrafish can perform a variety of locomotor behaviors at very early developmental stages (48 hpf), including forward swims, turns, escapes and prey captures. Kinematic analysis using high-speed video analysis and motion tracking software reveals that these locomotor behaviors are highly stereotyped, making them a good diagnostic tool to gauge the overall function of the nervous system (Burgess and Granato, 2007). Here, they are used to gauge the recovery process that *twister* undergoes during the first week of development.

For analysis of *twister* locomotion, I selected two behaviors that are indicative of normal neuromuscular function; a stimulus-induced escape response and a

spontaneously generated slow swim. These behaviors are characterized by a different activation pattern of both spinal motor neurons as well as skeletal muscle cells.

The escape response

The escape response is a defense mechanism that allows zebrafish to rapidly retreat from a threatening stimulus. The behavior can be evoked by a variety of stimuli including tactile (O'Malley et al., 1996; Liu and Fetcho, 1999), auditory (Zottoli, 1977) visual (Preuss et al., 2006) and electrical. It begins with an initial prolonged contraction of the axial musculature called the C-Start whose purpose is to generate propulsion away from the stimulus, followed by a bout of burst swimming. Burst swimming involves rapid, high-angular bends of the tail (up to 70 Hz) resulting in a high-velocity swim where speeds of 100 mm/s can be reached and a large degree of yaw (Budick and O'Malley, 2000; Thorsen et al., 2004). Studies using electromyographs and intracellular recordings indicate that the escape response is largely driven by the firing of primary motor neurons and the contractions of fast muscle cells (Liu and Westerfield, 1988).

Kinematic analysis of stimulus-induced escape responses were first performed in wild-type animals (Figure 3.1 A). A small electrical stimulation or a mechanical tap on the dish was used to evoke the response, which was recorded at 1000 frames-per-second using a high-speed camera. Body curvature, or the total head-tail bend angle, was a defined as the sum of the two angles formed between the head and tail segments compared to a middle body segment (Budick and O'Malley, 2000; Burgess and Granato, 2007). Measurements were made for each image, which was a sufficient sampling

frequency (1 kHz) to produce smooth oscillations for the responses (Burgess and Granato, 2007). The initial contraction (C-start) exhibited the largest degree of curvature, frequently producing head-to-tail contact and the maximum angle (220^{o}) measurable with Flote software. The bend direction of the C-start was random, and for the purposes of comparison, was assigned a positive value. The C-start was followed by a period of burst swimming characterized by a large body-bend angle (>60^{o}) and a tail-beat frequency of nearly 60 Hz.

Sinusoidal spontaneous slow swims

Spontaneous slow swims are characterized as mild caudal bending of the tail at low frequency (25-40 Hz) resulting in a slow velocity swim and little yaw (Budick and O'Malley, 2000; Buss and Drapeau, 2001; Muller and van Leeuwen, 2004). Electromyograph analysis showed that secondary motor neurons are activated during slow swims and propulsion is driven by the activation of both fast and slow muscle (Liu and Westerfield, 1988). Unlike during burst swimming, the pectoral fins are used in alternation to assist in slow forward swimming (Thorsen et al., 2004), a feature also associated with prey capture swimming.

Kinematic analysis of a wild-type spontaneous slow swim illustrates the sinusoidal swimming motion for this second form of zebrafish locomotion (Figure 3.1 B). This swimming event occurred in the absence of an external stimulus and was initiated by the animal. Slow swimming is characterized by a smaller body-bend angles (~30^{o}) and tail-beat frequency of ~30 Hz, half that of the escape response.

Figure 3.1: Two modes of swimming behavior in 72 hpf wild-type zebrafish.

(A) A stimulus-induced escape response from a 72 hpf wild-type animal was filmed at 1000 frames/s and movements were quantitated using motion tracking software. Curvature was measured for each image, and each point represents the sum of the head and tail bend angle relative to the central body axis. The initial bend, the C-start, exhibited the highest degree of curvature. The direction was arbitrary, and was assigned a positive value for consistency. The C-start was followed by a bout of swimming characterized by a large tail bend angle and a tail-beat frequency that could reach 70 Hz. (B) A spontaneous swim initiated by the animal without an external stimulus. The initial bend had a lower degree of curvature than the escape response, and the tail-beat is lower in both amplitude and frequency.

Figure 3.1

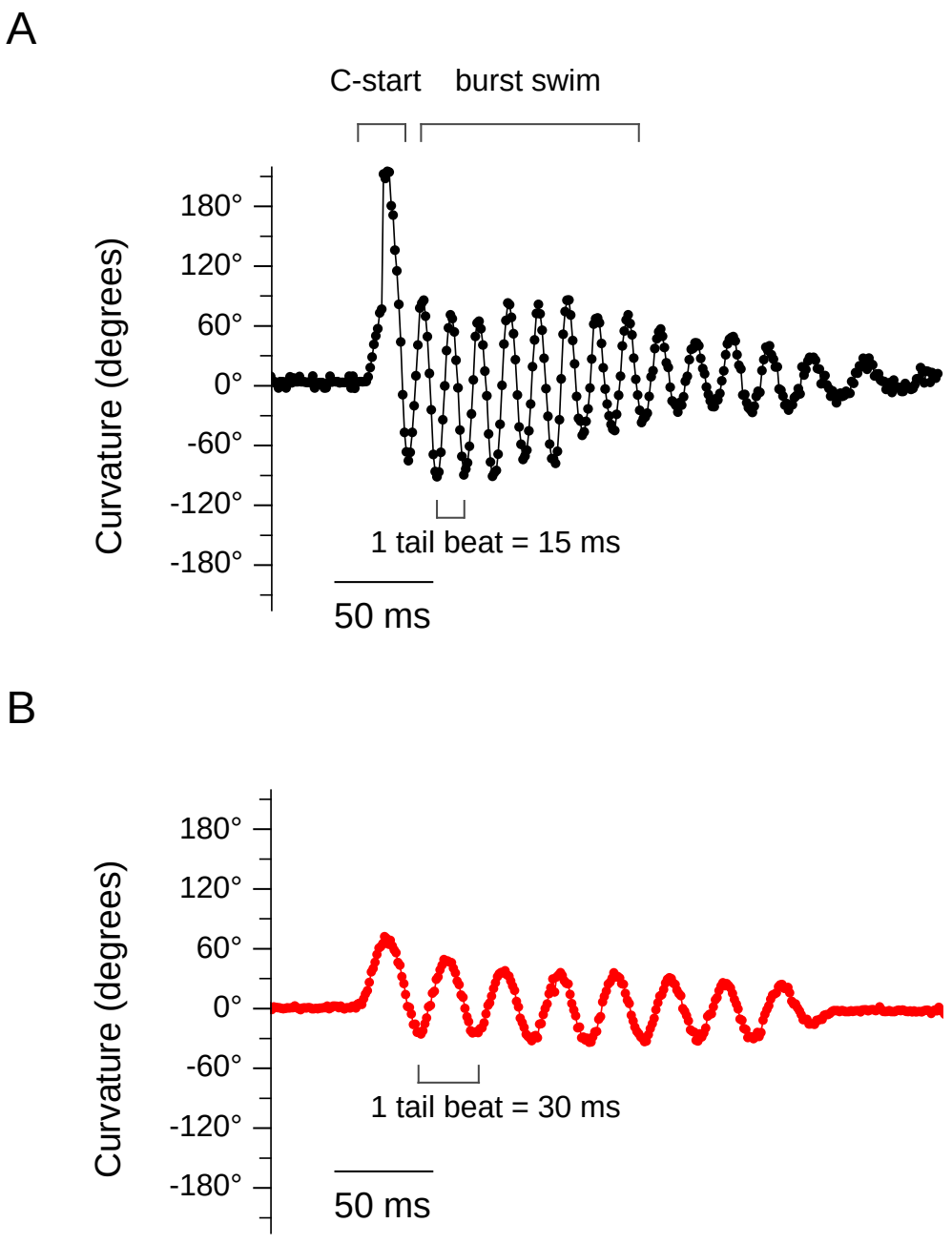
A
C-start
burst swim
180°
120°
60°
0°
-60°
-120°
-180°
Curvature (degrees)
1 tail beat = 15 ms
50 ms
B
180°
120°
60°
0°
-60°
-120°
-180°
Curvature (degrees)
1 tail beat = 30 ms
50 ms

Results

Wild type and twister escape responses

I performed kinematic analysis on zebrafish movement at three developmental time points. In wild-type animals, stimulus-induced escape responses were highly reproducible at all developmental stages (Figure 3.2 A). Even at stages before the swim bladder is fully inflated (48 and 72 hpf), animals were able to overcome the additional friction from laying against the recording dish and produced tail-beat frequencies identical to older animals (Figure 3.2, top & bottom; 48 hpf: 22 ± 5 ms, *n*=10; 72 hpf: 18 ± 3 ms, *n*=10). The distortion produced by this friction can be seen in the final 200 ms of the top trace in Figure 3.2A. The initial beat series (defined as the first two body-bends the animal performs) typically has a higher frequency (65 vs. 55 Hz) and this was consistent at all stages. The degree of curvature in the C-Start was identical in 72 hpf (167.3 ± 28.7°, *n*=9), and 120 hpf animals (153.8 ± 33.2°, *n*=7).

Escape responses in *twister* heterozygotes (*twi* $^{+/-}$) at 48 hpf consisted of a single maintained contraction that lasted for hundreds of milliseconds (703 ± 292 ms, *n*=25; Figure 3.2B, top panel). Two additional responses were frequently observed but could not be quantified with the Flote software. The first was a C-Start that exceeded the maximum bend angle of 220^{o} and was observed to reach 1.5 helical turns (540^{o}). The second was a simultaneous bilateral contraction of the axial musculature resulting in an accordion-like shortening of the body axis. Visual inspection of the high-speed movies showed that these contractions were similar in duration to the escape response, often

Figure 3.2: Stimulus-induced escape response in wild-type and *twi* $^{+/-}$ animals at three developmental time points.

(A) Escape responses in wild-type animals at 48 hpf (top), 72 hpf (middle) and 120 hpf (bottom). Each response was characterized by an initial C-start that exhibited the highest degree of curvature (167.3 ± 28.7°, *n*=9) followed by a bout of burst swimming. The tail-beat frequency and amplitude was lower at 48 hpf (top panel) because the animal had not yet developed a swim bladder and was resting on the bottom of the recording dish. (B) Escape response in *twi* $^{+/-}$ animals at 48 hpf (top panel), 72 hpf (middle panel) and 120 hpf (bottom panel). At 48 hpf, the response consisted of a single contraction that lasted on average for 703 ± 292 ms (*n*=25). By 72 hpf, the initial contraction was shorter in duration and the animal was able to perform a counterbend by contracting the musculature on the alternate side of the body. At 120 hpf the animal performed a C-start and counterbend similar to that of wild-type animals. These animals were delayed in developing a swim bladder, making the subsequent swimming response similar to the 48 hpf wild-type animal (compare to top panel in A).

Figure 3.2

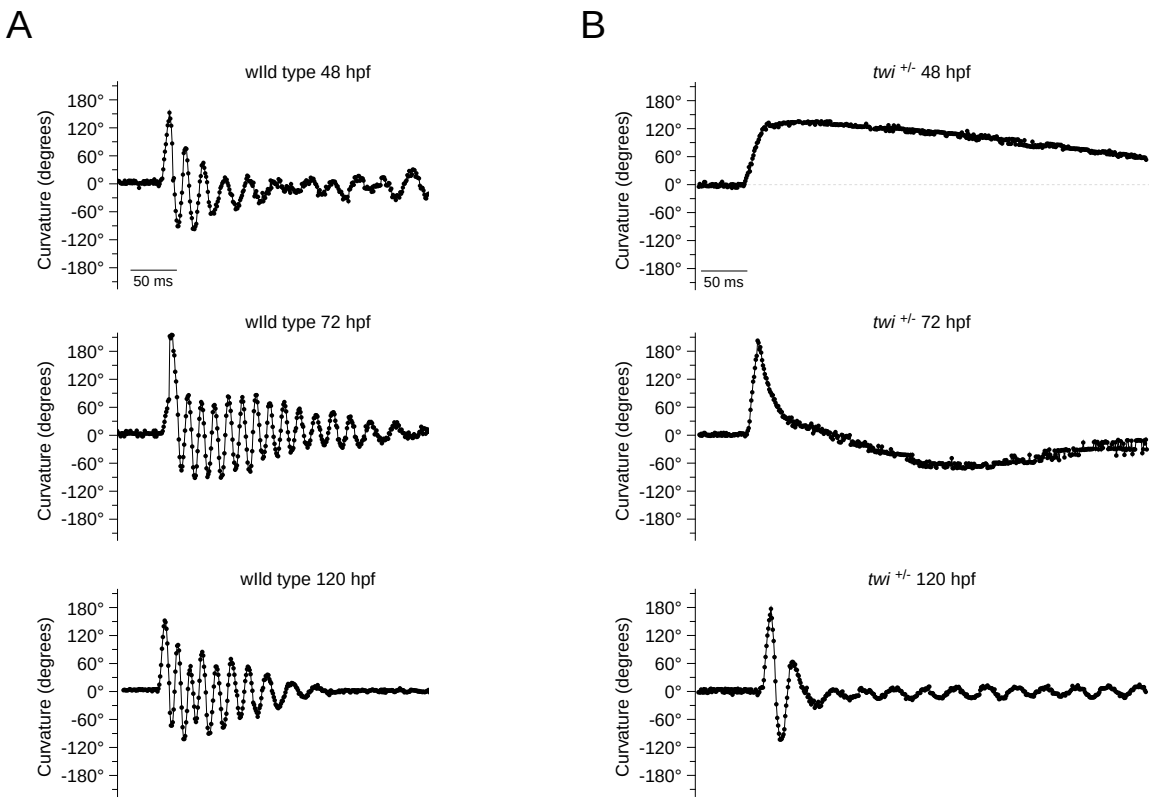
A
wIld type 48 hpf
wIld type 72 hpf
wIld type 120 hpf
B
twi +/- 48 hpf
twi +/- 72 hpf
twi +/- 120 hpf
Curvature (degrees)
180°
120°
60°
0°
-60°
-120°
-180°
50 ms

lasting for hundreds of milliseconds. At 72 hpf, *twi* $^{+/-}$ animals were able to make bilateral contractions (Figure 3.2 B, middle panel), but these bends were slower in duration than their wild-type counterparts (382 ± 151 ms, *n*=20). By 120 hpf, *twi* $^{+/-}$ were able to perform a C-start that had similar a degree of curvature (148.4 ± 33.1°) and beat frequency (20 ± 5 ms) to wild-type siblings (Figure 3.2 B, bottom panel). Although these animals were delayed in developing swim bladders (thus, friction is still a contributing factor) the initial movements demonstrated that *twi* $^{+/-}$ animals could indeed produce high-frequency swimming. By 168 hpf, swimming patterns of wild type and *twi* $^{+/-}$ were indistinguishable (data not shown).

Wild-type and twister spontaneous slow swims

Spontaneous forward swims were observed in wild-type animals beginning at 48 hpf (Figure 3.3 A, top panel). These movements consisted of low body-bend angles and tail-beat frequencies of 30 Hz. Body-bend angles were largest in the 48 and 72 hpf animals (Figure 3.3 A, top and middle panels). Visual inspection of high-speed movies revealed that animals used their pectoral fins to stabilize body movements during this swimming behavior, a distinguishing feature of slow swims. With the swim bladder fully inflated, low-amplitude body-bends at frequencies of 30 Hz propelled the animal through the water. Spontaneous slow swimming beat series consisted of 5-7 cycles, followed by a period of inactivity.

48 hpf *twi* $^{+/-}$ animals were unable to generate slow-swim movements. Spontaneous coiling contractions, reminiscent of earlier developmental stages

Figure 3.3: Spontaneous swimming in wild-type and *twi* $^{+/-}$ animals at three developmental time points.

(A) Spontaneous swimming behavior in wild-type animals at 48 hpf (top panel), 72 hpf (middle panel) and 120 hpf (bottom panel). At each time point, animals generated swimming behavior in the absence of an external stimulus. These responses had body-bend angles with a small degree of curvature (30-60°) and a low frequency of (25-40 Hz). (B) *twi* $^{+/-}$ generated slow swims only at 72 and 120 hpf (middle and bottom panels). The responses in these animals were similar to the wild-type response at the same developmental time point.

Figure 3.3

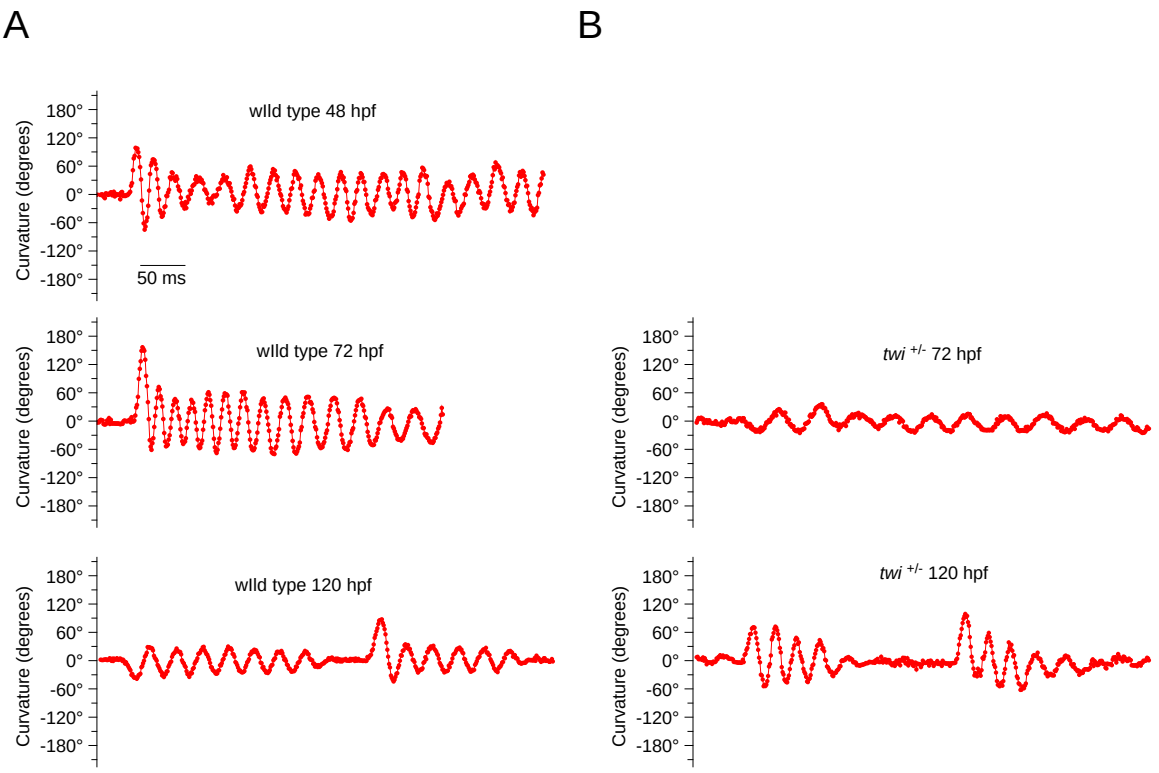
A
B
wIld type 48 hpf
wIld type 72 hpf
wIld type 120 hpf
twi +/- 72 hpf
twi +/- 120 hpf
Curvature (degrees)
180°
120°
60°
0°
-60°
-120°
-180°
50 ms

(24-36 hpf), occurred infrequently and the larvae were largely immobile. Beginning at 72 hpf, animals were able to generate slow swims (Figure 3.3 B, middle panel) where body-bend angles and tail-beat frequencies were identical to wild type. These responses could last for several seconds. Slow swimming in 120 hpf *twi* $^{+/-}$ animals were similar in both amplitude and frequency to wild type.

Conclusions Chapter III:

This analysis defined the developmental window for each stage of the *twister* recovery process:

- At 48 hpf, the *twister* escape response consists of prolonged coils that last for several hundred ms, accordion-like contractions and inability to perform bilateral contractions.
- 72 hpf marks the start of *twister* behavioral recovery with the first bilateral contractions and low-amplitude slow swimming.
- 120 hpf marks full functional recovery with ability to perform both high-frequency escape response and slow swimming.

CHAPTER IV

Characterization of synaptic current waveform at twister neuromuscular junctions

General overview

Neuromuscular transmission

The neuromuscular junction stands as one of the premier models for studying synaptic transmission. Its large size, relative simplicity, and accessibility make it amenable to electrophysiological recording as well as imaging studies. The roots of synaptic physiology are ingrained in the neuromuscular junction and many fundamental principles of synaptic transmission have been elucidated using this prototypical synapse. This chapter will introduce the factors underlying the synaptic current waveform, with an emphasis on those that shape its time course, as well as present evidence that the unusual synaptic kinetics of *twister* lead to aberrant muscle function and the observed motility defect.

A series of papers appearing between 1937 and 1941 led to the first identification of a chemical synaptic potential that resulted in the generation of muscle action potential and subsequent muscle contraction (Eccles et al., 1941a,b; Eccles and Kuffler 1941). One group was formed by the team of Eccles, Katz and Kuffler while a second was led by Te-Pei (TP) Feng (Feng and Shen, 1937; Feng, 1937; Feng, 1940). The early identification of curare as an antagonist of the ACh receptor catalyzed the dissection of the endplate potential (EPP) by lowering the amplitude to avoid generation of a muscle action potential (Eccles et al., 1941 a,b). This was critical, because in non-curarized

preparations, the EPP was sufficient in amplitude to generate an action potential, which obscured the EPP (Eccles et al., 1941b). Use of curarized muscle revealed a chemical synaptic potential that was local to the region of nerve-muscle contact and was non-propagating. Over the next two decades, Katz and colleagues systematically unraveled the basic mechanisms of nerve muscle transmission from quantal theory to calcium dependence of transmitter release.

Studies in the 1930s and 1940s were limited to intracellular voltage recordings of synaptic potentials rather than synaptic current. This greatly limited insights into the time course of synaptic transmission and the elementary events underlying the synaptic potential. Subsequent years led to the emergence of current recording rather than voltage recording techniques. The time course of the end plate current (EPC; Takeuchi and Takeuchi, 1959) and spontaneous miniature endplate currents (mEPC; Gage and Armstrong, 1968) revealed a fast rising and slowly decaying time course, and ushered in the era of synaptic current analysis. The nature of the underlying events and particularly the mechanisms dictating the time course of synaptic currents have been under investigation ever since their initial description.

Events underlying synaptic current kinetics

The release and diffusion of transmitter across the synaptic cleft occurs quickly (del Castillo and Katz, 1955; Eccles and Jaeger, 1958; Land et al., 1984) and transmitter rises to concentrations that support the binding of ACh to the receptor. The rising phase of the mEPC is influenced by both the diffusion constant for ACh ($4*10^{-6}$ cm^2 sec^{-1})

as well as the time it takes for the AChR to open once agonist is bound (Land et al., 1980). The concentration has never been determined due to the complications imposed by both channel block by ACh and receptor desensitization. However, it is generally thought that the ACh concentration reaches levels greater than the receptor Kd value (~10 μM) and may well locally saturate the receptors (Land et al., 1980; 1981). The concentration rapidly drops, due to hydrolysis by the enzyme acetylcholinesterase as well as association with the receptor (Katz, 1996).

After the rising phase, the remainder of the synaptic current time course is determined by the intrinsic properties of the activated receptors. The work that supports these findings was initiated in the early 1970's; the lab of Chuck Stevens combined the emerging techniques of voltage-clamp and fluctuation analysis and launched the current field of receptor biophysics. Noise analysis revealed an elementary component (the AChR) with a small, fixed conductance and whose kinetics were voltage-dependent in a similar way to synaptic current decay (Katz and Miledi 1971; Katz and Miledi 1972; Anderson and Stevens, 1973). However, the elementary conductance had a linear dependence on membrane potential while the relationship between amplitude of synaptic current and membrane potential was highly nonlinear. Under voltage-clamp, the slowing of elementary kinetics with membrane hyperpolarization was shown to be responsible for the nonlinear increase in EPC amplitude (Anderson and Stevens, 1973). Because the mean burst-duration was longer at hyperpolarized membrane potentials, there was more overlap of channel opening and thus larger EPC amplitude. This work also served to further refute the idea that the

decay phase refelcts the hydrolysis rate of ACh; the voltage-dependence of the synaptic current kinetics was not related to the ACh elimination processes, and the kinetics of the elementary event did not depend on AChE activity (Anderson and Stevens, 1973; Magleby and Stevens, 1972 a)

The exact nature of the elementary event underlying the synaptic current waveform was defined shortly after this time. Prior to the advent of single-channel recording, the two state (open and closed) models for ACh gating originally proposed for the Ach receptor was untested (del Castillo and Katz, 1957). It remained possible that the elementary event had rise and decay phases similar to that of the macroscopic synaptic current rather than occurring through discreet open and closed states. This issue was resolved, however, when the first single-channel recordings demonstrated that the elementary event had a 'square pulse-like shape' (Neher and Sakmann, 1976). While state diagrams have evolved to increasingly complicated schemes, certain fundamental features remain generally accepted. First, the channel must close before ACh can unbind as evidenced in the concentration independence of the single-channel open time and synaptic current decay (Magleby and Stevens, 1972 a,b). Second, the voltage dependence of the ACh receptor lies principally in the closing rate constant (Anderson and Stevens, 1973). The time course of the decay phase of the synaptic current reflects the inherent closing rate constant (α) of the ACh receptor, as well as the opening rate constant (β) and the dissociation rate constant (k_{-1}). These transitions are illustrated in the following simple scheme of ACh receptor gating, which will be revisited in chapter V:

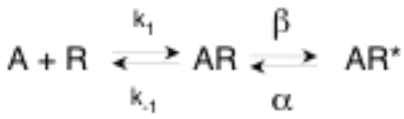

Evidence that twister mutation alters channel gating

The mutation in *twister* was identified to be in a region of the ACh receptor known to be important for channel gating (see Chapter 5 for more details). It was not surprising, therefore, that the initial electrophysiological characterization of *twister* demonstrated that the decay rates for EPCs were greatly prolonged compared to wild type (Lefebvre et al., 2004). However, this original work did not analyze the decay time constants of the synaptic currents, so our understanding of the mutation effect on channel gating and synaptic currents was limited. Furthermore the recordings were restricted to a single developmental time point (72 hpf), and the recordings were likely performed on slow muscle cells. To begin to understand the physiological effects of the *twister* mutation on synaptic function, I undertook a quantitative analysis of the synaptic current kinetics of fast muscle at 48 hpf, corresponding to the height of the behavioral defect. In this chapter, I present the evidence supporting a complex synaptic decay in *twister* mutants, and also directly examine the effect of the current waveform on the muscle depolarization.

Results

Wild-type synaptic current characteristics

Zebrafish offer a unique opportunity to explore the kinetics of synaptic current in wild type and mutant animals. A large quantal size renders the recordings of mEPCs an effective and simple means to measure synaptic current kinetics. Comparison of mEPCs and evoked synaptic currents (EPCs), show good agreement in decay kinetics (Wen and Brehm, 2005). However, the mEPCs are subject to less distortion by inadequate voltage-clamp due to their comparably much smaller amplitude. Past studies from our lab have shown that whole-cell voltage-clamp measurements of synaptic current mirrored the extracellularly recorded counterpart, which provides an unbiased reflection of the true synaptic waveform (Luna and Brehm, 2006). Under voltage-clamp, at a holding potential of -90 mV, the resulting mEPC averaged ~750 pA and the decay is fully described by a single exponential function with a time constant of 0.58 ± 0.10 ms (Figure 4.1). The mEPP counterpart averaged ~14 mV (Figure 4.1).

Characterization of twister mEPC kinetics

All of the synaptic current recordings for *twister* mutants were performed on heterozygous fish, as the homozygous muscle suffered too much deterioration, even at early time points, to permit recording currents in the whole-cell configuration.

At 48 hpf the mEPC decay time course was greatly prolonged compared to those recorded from wild-type muscle (Figure 4.2 A). At this stage of development, all spontaneous synaptic currents in *twi* $^{+/-}$ fish required the sum of three exponentials for

Figure 4.1: Synaptic currents and potentials in zebrafish fast muscle.

Whole-cell recording from a 72 hpf wild-type fast muscle cell showing a miniature end-plate current (mEPC), and a miniature end-plate potential (mEPP) that arise from the spontaneous fusion of a single vesicle. Under voltage-clamp, at a holding potential of -90 mV, the mEPC that has an average amplitude of 750 pA and a decay that is fit peak-to-end with a single exponential function (red overlay) with a time constant of ~0.5 ms. Under current clamp, the average amplitude of the mEPP is 20 mV, and the decay is complete within several milliseconds. The end-plate current (EPC) was evoked by stimulation of the primary motor neuron. The EPC has an average amplitude of 6 nA at a holding potential of -50 mV, and a decay time constant similar to the mEPC. Under current clamp, stimulation of the motor neuron results in the generation of an action potential in the muscle cell that causes the membrane potential to become positive, and repolarization occurs within 10 ms.

Figure 4.1

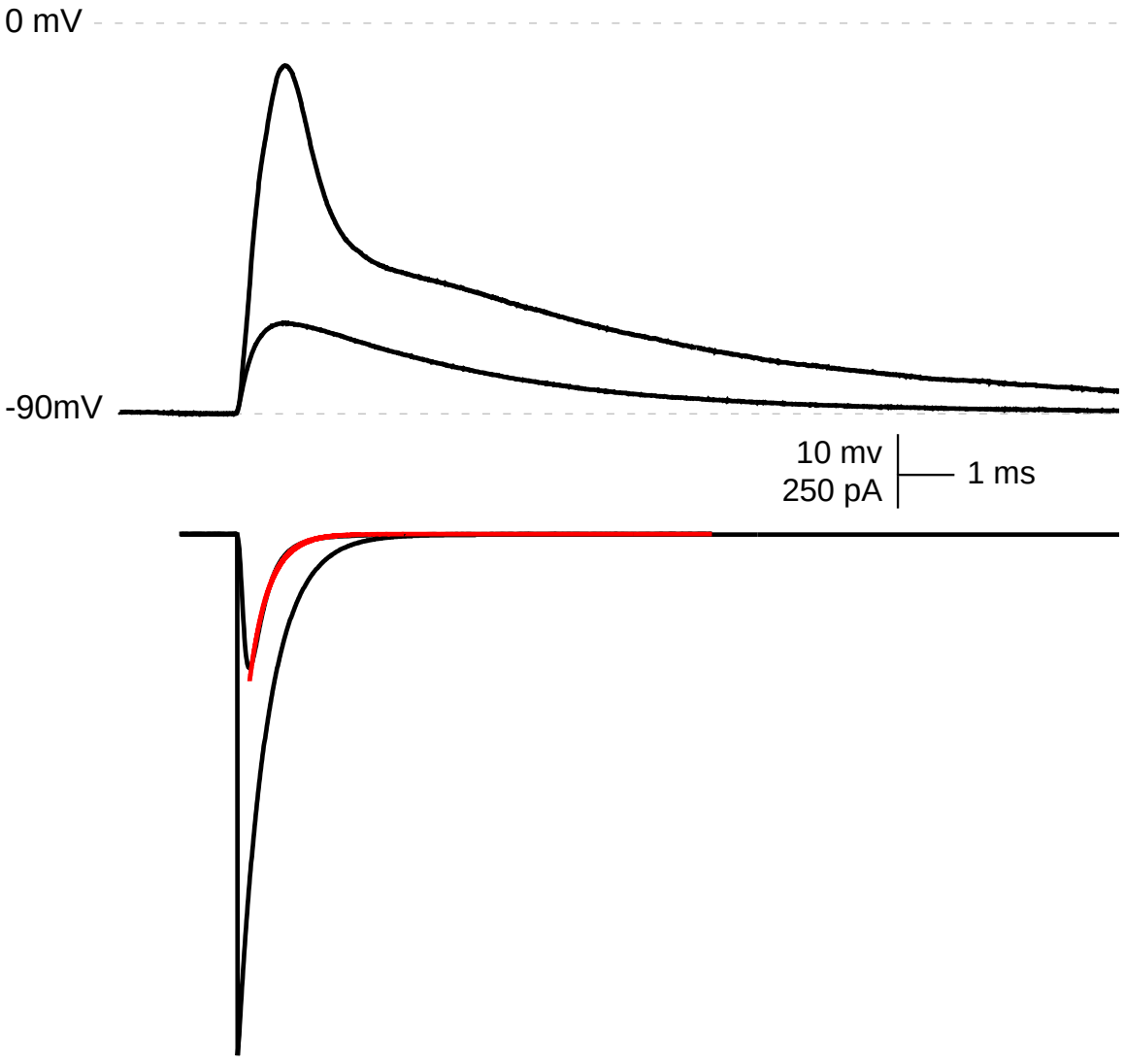

Figure 4.2: Kinetics of spontaneous end-plate currents in wild-type and *twi* $^{+/-}$ fast muscle.

(A) Representative mEPCs recorded from 48 hpf wild-type and *twi* $^{+/-}$ fast muscle. Synaptic current decays (black) were fit peak-to-end (red overlay) by either a single exponential function for wild type or by the sum of 3 exponential functions for *twi* $^{+/-}$. The insets show the individual components of each fit. (B) The mean decay time constants computed for each recording are indicated by filled circles and the overall mean ± SD by an open circle (wild type, *n*=9; *twi* $^{+/-}$, *n*=14). Between 7 and 115 events were measured for each recording. (C) Fractional contribution to overall amplitude by each exponential component in *twi* $^{+/-}$. Values for B and C are provided in Table 4.1.

Figure 4.2

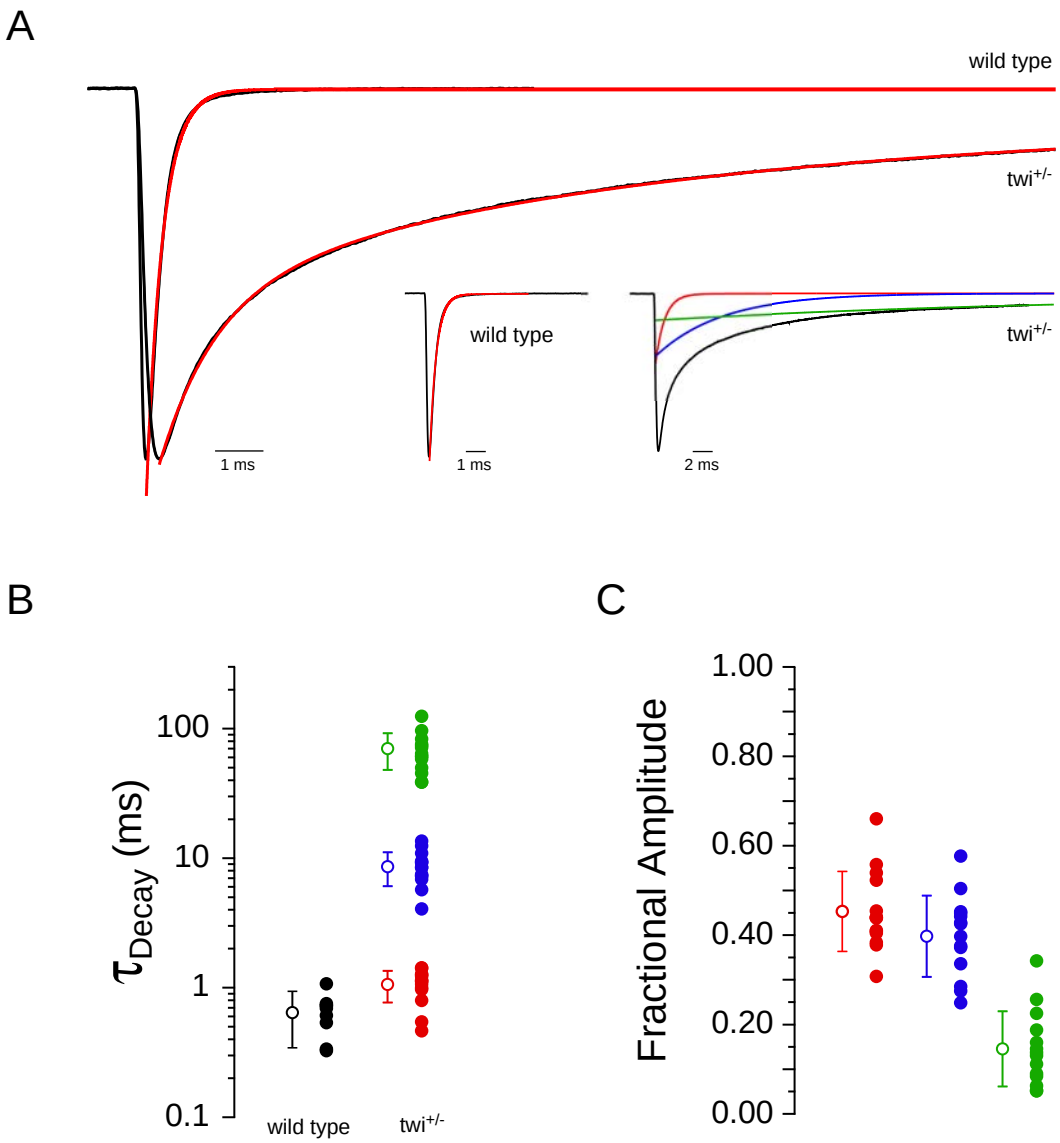
A
wild type
twi+/-
1 ms
wild type
1 ms
twi+/-
2 ms
B
τDecay (ms)
100
10
1
0.1
wild type
twi+/-
C
Fractional Amplitude
1.00
0.80
0.60
0.40
0.20
0.00

proper fit of the decay phase. Fitting by the sum of two exponentials consistently failed to adequately fit the fast component of decay, and often underestimated the return to baseline (Figure 7.2 A & B). The average time constants at 48 hpf corresponded to 1.1 ± 0.3 ms, 8.6 ± 2.5 ms, and 70.2 ± 22.0 ms for the fast (τ_f), intermediate (τ_i), and slow (τ_s) time constants respectively (*n*=14; Figure 4.2 A & B). The average fractional contribution to overall peak synaptic current in *twi* $^{+/-}$ corresponded to 0.45 ± 0.09 for τ_f, 0.40 ± 0.09 for τ_i and 0.15 ± 0.08 for τ_s (Figure 4.2 C). The complex decay of *twister* stands in contrast to wild-type mEPCs, which decay along a single exponential time course with a mean time constant of 0.6 ± 0.3 ms (*n*=9) at 48 hpf (Figure 4.2 B; Table 4.1).

Hypotheses for the three components of decay

I propose that the three components of decay represent kinetically distinct receptor processes, likely related to the mixture of wild-type and mutant α subunits. However, it is possible that one or more of the prolonged components represents activation of a secondary conductance other than the ACh receptor. Previous studies of EPC kinetics on wild type receptors, employing the paired motor neuron-muscle recording technique, demonstrated that EPCs readily reverse sign above and below the reversal potential (Wen and Brehm, 2005). Moreover, the EPC decay conformed to a single exponential function at both positive and negative potentials, and the time constant of the decay was voltage dependent, with faster time constants recorded at more positive holding potentials (Wen and Brehm, 2005). To determine whether the

three kinetic processes represent intrinsic receptor gating, I examined the decay kinetics of *twister* mEPCs recorded at +60 mV and -60 mV holding potential (Figure 4.3). Fitting synaptic current decays at positive potentials revealed that all the three kinetic components were present. The time constant each component of the synaptic decay was also faster at the positive holding potential (Table 4.2), a property that has been well described for the AChR (Magleby and Stevens, 1972). Therefore, these experiments provided two pieces of evidence in support the idea that the three kinetic components represent intrinsic receptor gating properties.

Effect of prolonged synaptic current decay on postsynaptic potential

The consequences of the complex synaptic current kinetics on action potential generation in fast muscle cells were determined under current-clamp recording using two approaches. First, simulated command-voltage waveforms based on *twi* $^{+/-}$ and wild-type synaptic current waveforms were injected directly into 48 hpf wild-type muscle (Figure 4.4 A & B). The current amplitudes were based on evoked synaptic currents obtained using motor neuron-muscle paired recording. The decay time course was based on the mean time constants and fractional contribution by each exponential component. Both wild-type and *twi* $^{+/-}$ synaptic currents consistently generated a single action potential (Figure 4.4 A & B). However, wild-type repolarization was rapid compared to *twi* $^{+/-}$, which exhibited a prolonged after-depolarization. Next, muscle responses were recorded in paired motor neuron-muscle current clamp recordings

Figure 4.3: mEPCs recorded at positive and negative holding potentials.

Top: Example mEPCs recorded from a 48 hpf *twi* $^{+/-}$ animal at a negative holding potential of -60 mV (red traces) mirror those recorded at a positive holding potential of +60 mV (black traces). Bottom, a single mEPC recorded +60 mV (black) fit by a triple exponential function (red overlay). The average time constants and fractional contributions of each component to the overall decay at the positive holding potential are provided in Table 4.2.

Figure 4.3

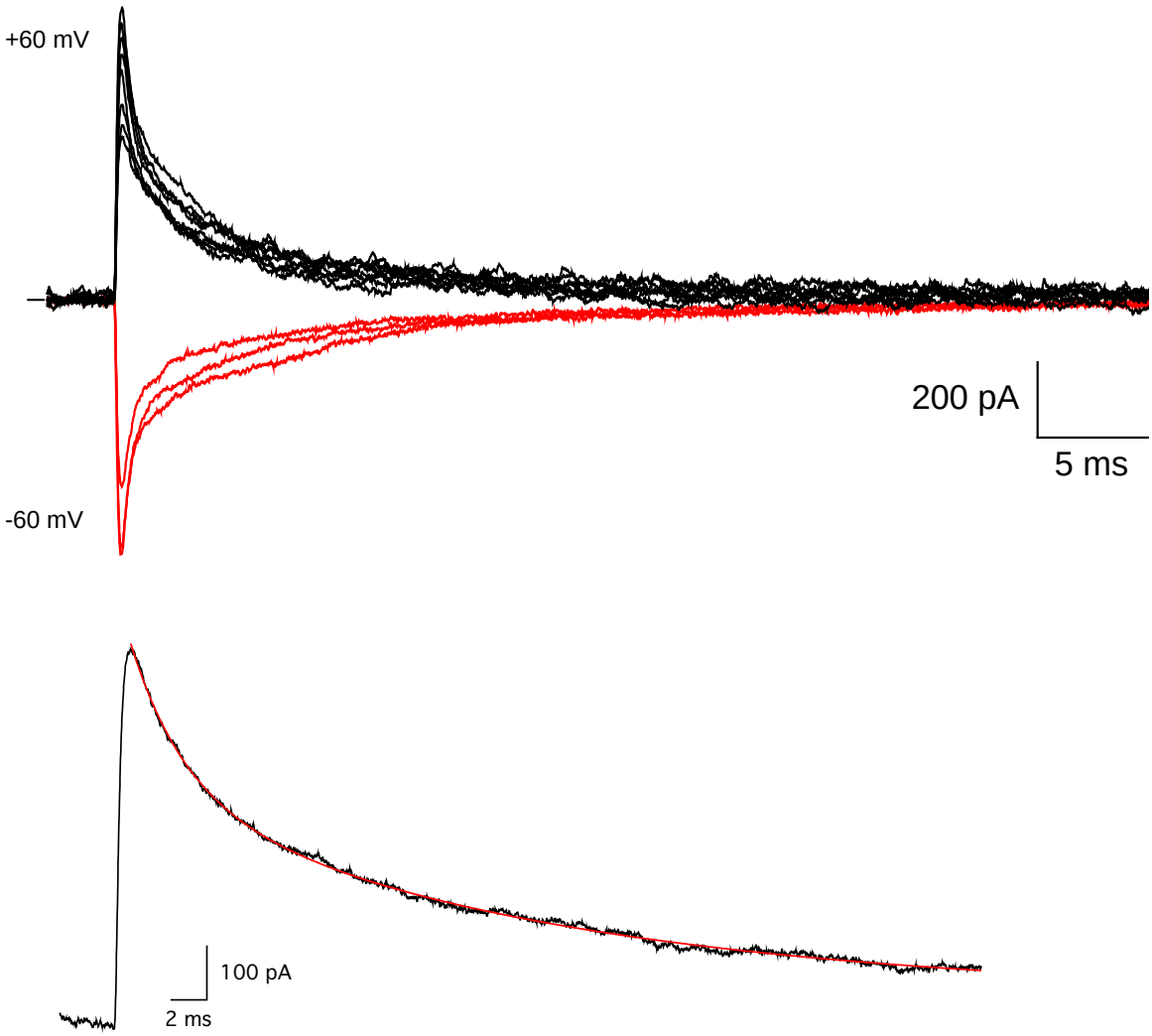

Table 4.1: Characteristics of 48 hpf wild-type and *twi* $^{+/-}$ fast muscle mEPC decays

	Decay Time constant (ms)			Fractional Contribution		
	τ_{fast}	$\tau_{intermediate}$	τ_{slow}	Fast	Intermediate	Slow
wild type 48 hpf	0.64 ± 0.23			1.00 ± 0.00		
$twi^{+/-}$ 48 hpf	1.06 ± 0.29	8.61 ± 2.53	70.21 ± 22.04	0.45 ± 0.09	0.40 ± 0.09	0.15 ± 0.08
$twi^{+/-}$ 48 hpf +60 mV	0.70 ± 0.29	4.40 ± 1.51	39.06 ± 23.58	0.39 ± 0.10	0.47 ± 0.07	0.13 ± 0.10

Figure 4.4: Effect of prolonged synaptic currents on post-synaptic potential.

Representative action potential waveforms recorded from 48 hpf wild type fast muscle were elicited using voltage command waveforms based on the average synaptic current decays for (A) wild type and (B) *twi* $^{+/-}$. Waveforms were based on recordings as shown in Figure 4.2. The command waveforms are shown in red and the associated muscle responses are shown in black (*n*=5 cells; between 12 and 20 action potentials were averaged for each cell). Paired current-clamp recordings of motor neuron (red) and muscle action (black) potentials for (C) 48 hpf wild-type (*n*=4 pairs; 7-28 action potentials per cell) and (D) *twi* $^{+/-}$ (*n*=6 pairs; 8-26 action potentials per cell) fast muscle.

Figure 4.4

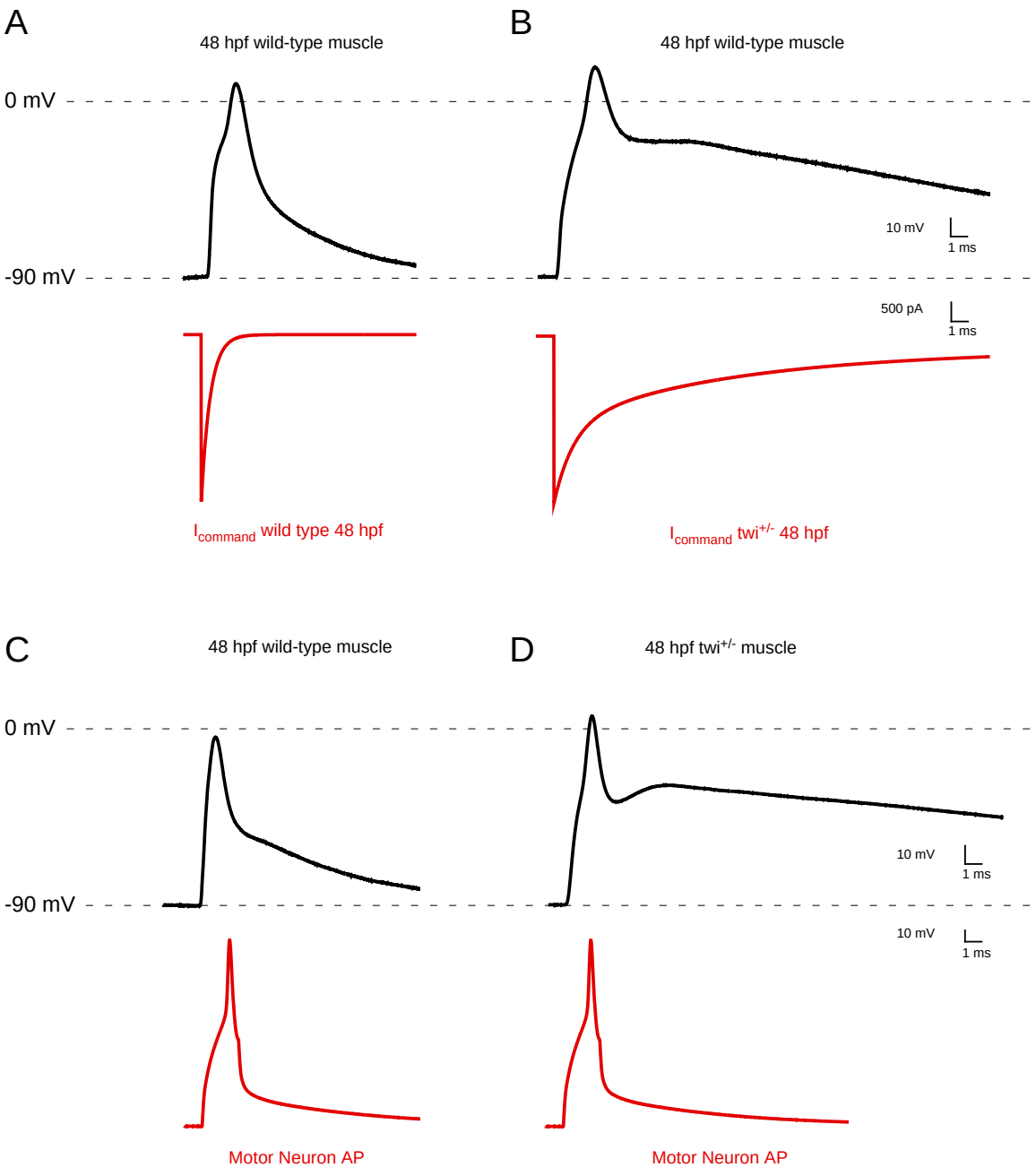
A
48 hpf wild-type muscle
0 mV
-90 mV
I command wild type 48 hpf
B
48 hpf wild-type muscle
10 mV
1 ms
500 pA
1 ms
I command twi+/- 48 hpf
C
48 hpf wild-type muscle
0 mV
-90 mV
Motor Neuron AP
D
48 hpf twi+/- muscle
10 mV
1 ms
10 mV
1 ms
Motor Neuron AP

(Figure 4.4 C & D). Once again, only a single action potential was observed. The action potential in *twi* $^{+/-}$ was followed by a greatly prolonged depolarization. Thus, both approaches point to a maintained contraction in *twi* $^{+/-}$ that results from prolonged depolarization and not from repetitive firing of muscle action potentials.

The prolonged depolarization could potentially lead to prolonged contraction by two mechanisms. First, because zebrafish fast muscle is nearly isopotential, the synaptic depolarization will spread to all muscle membrane, including the T-tubules. Normally, a sodium action potential in muscle is required for depolarization to reach the T-tubules. The ensuing activation of the DHP receptor and subsequent release of intracellular calcium could proceed in zebrafish in the absence of an action potential. In wild-type fish, a fast repolarization would prevent this prolonged calcium release. Alternatively, calcium entering through the ACh receptors may directly contribute to prolonged contraction. The muscle ACh receptor is permeable to calcium and with such long openings the direct calcium entry may be considerable (Decker and Dani, 1990; Gomez et al., 2002).

Conclusions Chapter IV:

- *twister* synaptic decay is comprised of three distinct kinetic components:
    1. τ_{fast} is 1.1 ms and 45% of the mEPC amplitude
    2. $\tau_{intermediate}$ is 8.6 ms and 40% of the mEPC amplitude
    3. τ_{slow} is 70.2 ms and 15% of the mEPC amplitude
- Each of the three kinetic components are likely to represent ACh receptors with unique gating properties.
- *twister* synaptic current waveforms result in a single muscle action potential followed by an excessively long membrane depolarization.

CHAPTER V

The characteristics of *twister* ACh receptor isoforms

General overview

Muscle nicotinic ACh receptors belong to the cis-loop superfamily of receptors, which includes the neuronal ACh, $GABA_A$, glycine, serotonin and invertebrate glutamate and histidine receptors (Karlin, 2002; Sine and Engel, 2006, for individual references see Akabas, 1994). These receptors generate the fast synaptic current that depolarizes the muscle membrane and initiates the cascade leading to muscle contraction. This chapter will discuss the general structural and functional features of the ACh receptor, and introduce experiments that explore how these features are altered by the *twister* mutation.

Structural studies

Biochemical purification of receptors from the electric organ of the ray *Torpedo* in the 1960s indicated that receptors are formed by the association of 4 distinct subunits, termed α, β, δ, γ (Reynolds and Karlin, 1978). The information provided by the purification led to the cloning of individual subunits, first from *Torpedo* (Noda and Numa, 1983b), and later from mammals. A fifth subunit, termed ε, was later identified from cloning studies of the skeletal muscle ACh receptor subunits (Mishina et al., 1986). Information from sequencing and hydropathy plots revealed similarities in both the primary structure and membrane topology of all subunits (Noda and Numa, 1983b; Steinbach, 1989; Karlin and Akabas, 1995; Karlin, 2002). Each subunit has 4

transmembrane alpha helical domains (M1-M4) oriented in the membrane such that the large N-terminus (~200 amino acids) and C-terminus are both extracellular (Noda and Numa, 1983a; Figure 5.1 A). Functional receptors require two copies of α, and one each of β, δ and either γ or ε in the final position (Figure 5.1 B). Individual subunits associate in a cylindrical arrangement, with the alpha helices of the second transmembrane domain (M2) of each subunit packed around a central channel (Figure 5.1 B). The M2 domain has been well characterized, particularly because these helices make the major contribution to the channel gate, pore, and charge selectivity filters (Imoto et al., 1986; Villarroel et al., 1991; Galzi et al., 1992; Akabas et al., 1994; Wilson and Karlin, 1998; reviewed in Karlin, 2002; Miyazawa et al., 2003). This region of the channel is highly conserved, as evidenced by the high degree of sequence homology across species (Figure 5.2). One of the most surprising discoveries was that the two binding sites formed by identical α-subunits were non-equivalent (Damle and Karlin, 1978). The difference in binding characteristics was shown to result from the association of the α subunit with different neighboring subunits where two hydrophobic binding pockets for ACh are formed by the interfaces of the α-δ and α-γ or α-ε subunits (Brisson and Unwin, 1985; Blount and Merlie, 1989; Figure 5.1 B).

ACh receptor isoforms and gating

The biochemical purification of the receptor subunits from *Torpedo* in the 1960s and 1970s did not provide evidence for the coexistence of functionally distinct isoforms. That discovery came from application of noise analysis to developing rat (Sakmann and Brenner, 1978; Fischbach and Schuetze, 1980) and *Xenopus* (Kullberg et al., 1981; Brehm

Figure 5.1: Schematic of the ACh receptor.

(A) Representation of a single subunit of the ACh receptor. Four transmembrane alpha helical domains (M1-M4) are represented as cylinders crossing the lipid bilayer. The N and C termini are located in the extracellular space. (B) Arrangement of the 5 subunits of the pentameric receptor. Individual subunits are arranged such that the M2 helices make the primary contribution to the pore. ACh binding pockets are located at the interfaces of the α-δ and α-γ or α-ε interfaces.

Figure 5.1

A

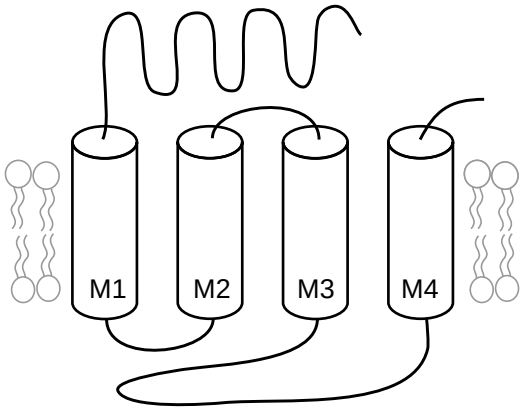
M1
M2
M3
M4

B

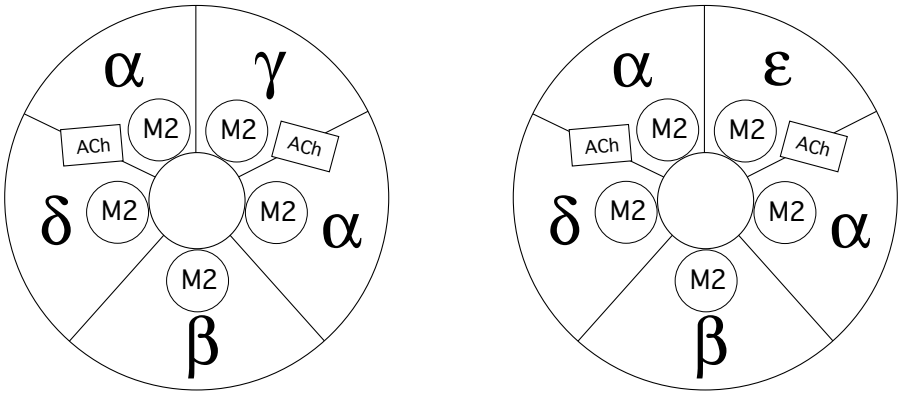
α
γ
ACh
M2
M2
ACh
δ
M2
M2
α
M2
β
α
ε
ACh
M2
M2
ACh
δ
M2
M2
α
M2
β

Figure 5.2: Amino acid alignment of the M2 alpha helix.

The protein sequence for the M2 alpha helix is highly conserved among vertebrates. The location of the leucine to proline mutation of *twister* is indicated in red. Three numbering systems are employed for the receptor. The top is the residue number for the location within the entire α subunit while a second and third are specific for the M2 alpha helical region. Residues that are accessible to the extracellular space are indicated by an asterisk, and this includes position 258 or 16', where the *twister* mutation is found.

Figure 5.2

	241	242	243	244	245	246	247	248	249	250	251	252	253	254	255	256	257	258	259	260	261	262	263	264	265	266	267	268
M2 Helix	1	2	3	4	5	6	7	8	9	10	11	12	13	14	15	16	17	18	19	20	21	22	23	24	25	26	27	28
M2 Helix*				4				8			11	12			15			18				22						

	-2'	-1'	1'	2'	3'	4'	5'	6'	7'	8'	9'	10'	11'	12'	13'	14'	15'	16'	17'	18'	19'	20'	21'	22'	23'	24'	25'	26'
Zebrafish (*twister*)			M	T	L	S	I	S	V	L	L	S	L	T	V	F	L	P	V	I	V	E	L	I	P	S	T	S
Zebrafish (wild type)			M	T	L	S	I	S	V	L	L	S	L	T	V	F	L	L	V	I	V	E	L	I	P	S	T	S
Torpedo Ray			M	T	L	S	I	S	V	L	L	S	L	T	V	F	L	L	V	I	V	E	L	I	P	S	T	S
Frog			M	T	L	S	I	S	V	L	L	S	L	T	V	F	L	L	V	I	V	E	L	I	P	S	T	S
Chick			M	T	L	S	I	S	V	L	L	S	L	T	V	F	L	L	V	I	V	E	L	I	P	S	T	S
Mouse			M	T	L	S	I	S	V	L	L	S	L	T	V	F	L	L	V	I	V	E	L	I	P	S	T	S
Human			M	T	L	S	I	S	V	L	L	S	L	T	V	F	L	L	V	I	V	E	L	I	P	S	T	S

et at., 1983) skeletal muscle. In both cases, analysis of noise spectra pointed to a developmental shift to higher cutoff frequencies, suggesting a time-dependent shortening of ACh receptor event lifetime. The development of the patch-clamp technique and single-channel recordings made it possible to directly observe the single ACh receptor lifetime on muscle (Neher and Sakmann, 1976). Single-channel kinetics of developing muscle indicated a change in open time that corresponded to the developmental alteration in synaptic currents (Siegelbaum et al., 1984; Brehm et al., 1984). The mechanisms causal to the shift, however, remained a point of contention throughout the decade. In rat, the mechanism was thought to involve a chemical modification of the receptor, presumably phosphorylation, which depended on the proximity to the nerve terminal (Michler and Sakmann, 1980). In *Xenopus*, however, evidence pointed to two functionally distinct isoforms, and the process of change in ACh channel kinetics did not depend on the proximity to the site of nerve-muscle contact (Kullberg et al., 1981; Brehm et at., 1983).

The cloning and expression of bovine muscle ACh receptors later that decade provided the solution. A newly described receptor subunit, termed ε, was coexpressed in *Xenopus* oocytes along with α,β,δ and was shown to confer fast channel gating (Takai et al., 1985; Mishina et al., 1986; Jackson et al., 1990). Measurements of γ and ε mRNA revealed a developmental change in expression that coincided with the shift to fast gating (Witzemann et al., 1987). Therefore, the fast and slow components of the noise spectrum were identified as resulting from a γ to ε switch. The structural basis for the functional distinctions conferred by ε or γ has not been firmly established for any

species, however at least one study has shown that αβδε and αβδγ can both adopt the functional properties of the other through a shift in the gating mode (Naranjo and Brehm, 1993).

The finding that subunit composition can dictate channel kinetics has subsequently been shown for $GABA_A$ receptors (Reviewed in Wisden and Seeburg, 1992), glutamate receptors (Reviewed in Nakanishi et al., 1994) and voltage-dependent potassium channels (Reviewed in Pongs and Schwarz, 2010). Additionally, the finding prompted many studies that used mutagenesis to identify the role of key residues in channel function (Imoto et al., 1986; Leonard et al., 1988; Villarroel et al., 1991). Mutations in the M2 domain of ACh receptors (also the location of the *twister* mutation site) are often associated with altered gating kinetics (Leonard et al., 1988; Villarroel et al., 1991; Reviewed in Bouzat, 1997). The exact effects of the *twister* T to P mutation in the M2 region on single-channel function were not known when I began these studies; however, it seemed likely that the altered synaptic current decays would be due to alterations in channel gating kinetics. Additionally, because subunit composition plays a key role in determining decay kinetics of ACh receptors, I was interested to examine whether different mutant *twister* α subunit containing isoforms could account for the complexity of the synaptic decay profile.

I first provide a characterization of the effects of the *twister* on single-channel conductance and burst-duration for the two receptor isoforms containing γ or ε. These fingerprints are then used to identify the receptor types present on twister muscle during single-channel recordings. Ultimately, this analysis provided a molecular basis

for the three components of synaptic decay in *twister* heterozygous fish.

Results

Identifying the effects of the L258P mutation on single-channel function

To characterize the function of ACh receptors containing the *twister* subunit, I reconstituted zebrafish receptors in *Xenopus* oocytes. Fortunately, the full complement of zebrafish subunits α, β, δ, γ and ε had been recently cloned and expressed heterologously (Mongeon et al., 2011). This paved the way for comparisons of the following major isoforms: $\alpha\beta\delta\varepsilon$, $\alpha\beta\delta\gamma$, $\alpha_{twi}\beta\delta\gamma$ or $\alpha_{twi}\beta\delta\varepsilon$. Single-channel currents from identified isoforms were recorded using outside-out patches of oocyte membrane. Receptors were present at all positions along the cell surface, and no effort was made to localize recordings to a specific region of the cell. Visual inspection of sample traces for each of the four isoforms pointed to large differences in burst-duration between wild-type and mutant receptors (Figure 5.3 A-D). These events reflect the transition of a single AChR between the closed and open state. Occasionally, the openings are interrupted by extremely brief closures termed 'nachschlags' (Colquhoun and Sakmann, 1981; 1985). Due to the frequency response of these recordings, extremely brief closures (<200 μs) were not resolved, and two transitions separated by nachschlags were counted as one. Because of this limitation, the measurement of event duration represents the burst duration, rather than the open duration. The term "mean channel open time" is commonly used in ACh receptor literature, but this implies that all closures are resolved. Openings by both $\alpha_{twi}\beta\delta\gamma$ (Figure 5.3 D) and $\alpha_{twi}\beta\delta\varepsilon$ (Figure 5.3 B)

Figure 5.3: ACh-activated single-channel currents associated with different receptor isoforms.

Representative single-channel recordings of ACh-activated currents from outside-out patches of *Xenopus* oocytes expressing either (A) $\alpha\beta\delta\varepsilon$ (B) $\alpha_{twi}\beta\delta\varepsilon$ (C) $\alpha\beta\delta\gamma$ or (D) $\alpha_{twi}\beta\delta\gamma$ receptors. Example semi-log burst-duration histograms for each receptor isoform fit with either a single exponential (A,B & D) or bi-exponential (C) function. (E) Cumulative current-voltage relations showing mean ± SD for $\alpha_{twi}\beta\delta\varepsilon$ (filled circles, *n*=8 recordings) and $\alpha_{twi}\beta\delta\gamma$ (open circles, *n*=8 recordings) with linear fits. (F) Scatterplot of mean slope conductance obtained for individual recordings from $\alpha_{twi}\beta\delta\varepsilon$ (filled circles) and $\alpha_{twi}\beta\delta\gamma$ (open circles) shown alongside the overall mean ± SD for each distribution. The mean ± SD for wild-type counterparts are shown as open squares (taken from Mongeon et al., 2011). Between 31 and 111 events were used to generate each point in E and F. (G) Scatterplot of mean burst-duration from $\alpha_{twi}\beta\delta\varepsilon$ (filled circles, *n*=7 recordings) and $\alpha_{twi}\beta\delta\gamma$ (open circles, *n*=10 recordings) receptors along with the overall mean ± SD. Between 659 and 1147 events for each recording were used to generate the individual mean values. The mean ± SD values for the wild-type counterpart are shown as open squares (taken from Mongeon et al., 2011).

Figure 5.3

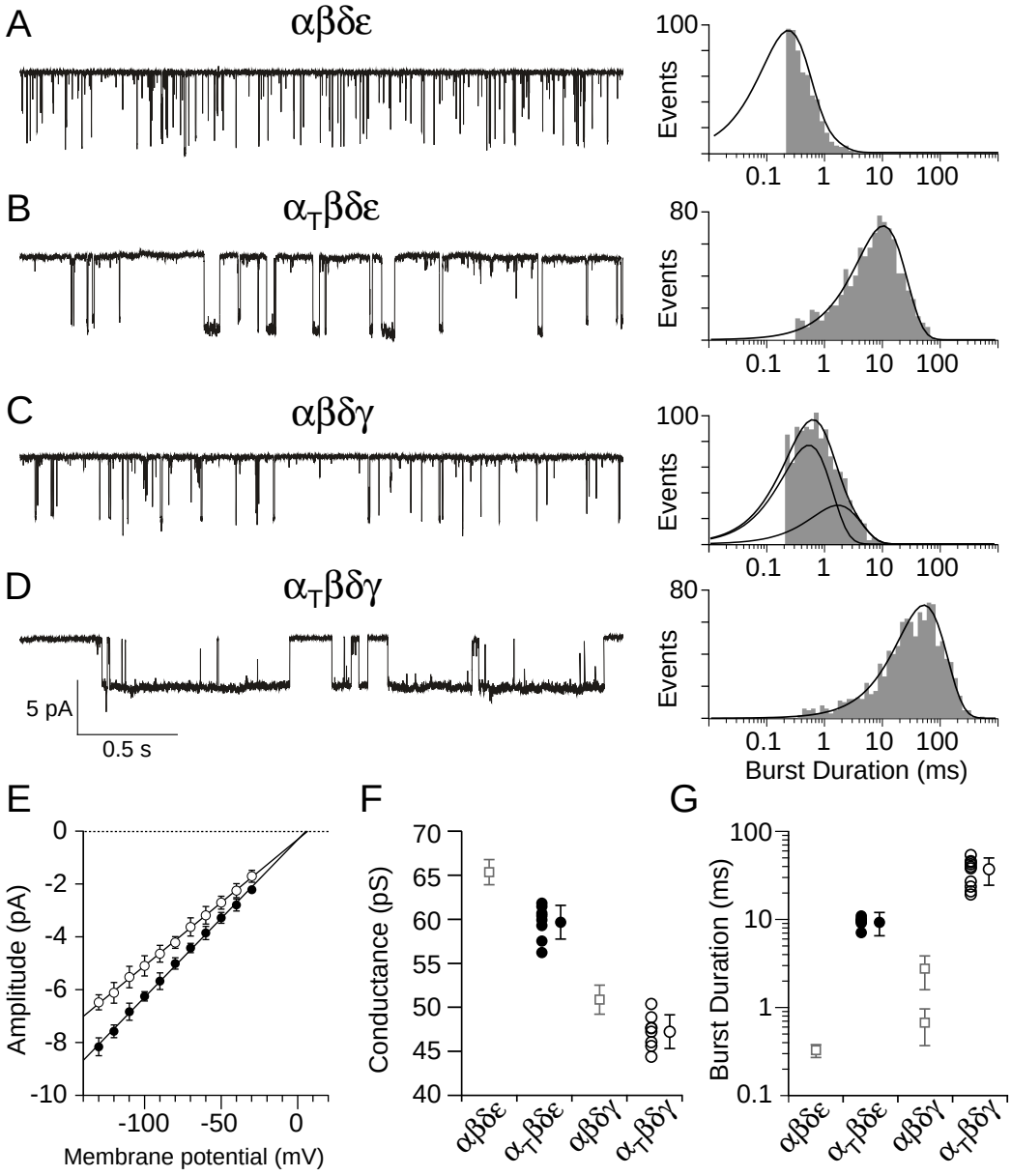
A
αβδε
B
αTβδε
C
αβδγ
D
αTβδγ
5 pA
0.5 s
Events
100
80
0.1
1
10
100
Burst Duration (ms)
E
Amplitude (pA)
0
-2
-4
-6
-8
-10
-100
-50
0
Membrane potential (mV)
F
Conductance (pS)
70
65
60
55
50
45
40
αβδε
αTβδε
αβδγ
αTβδγ
G
Burst Duration (ms)
100
10
1
0.1

receptors were considerably longer than wild-type αβδγ (Figure 5.3 C) and αβδε (Figure 5.3 A). Current-voltage relations obtained for both α_{twi}βδγ and α_{twi}βδε single-channel currents were linear and yielded slope conductances of 48 pS and 60 pS, respectively (Figure 5.3 E). Both values were slightly lower than the wild-type αβδε and αβδγ counterparts (Figure 5.3 F). The burst-duration histograms for αβδε and α_{twi}βδε were each fit with a single exponential (Figure 5.3 A & B) with overall mean time constants corresponding to 0.32 ± 0.05 ms and 9.27 ± 2.74 ms, respectively. In the specific case of αβδε, the fast kinetics limited full resolution of the primary component of burst-duration, so the mean time constant could potentially be even briefer than our estimate. The burst-duration distribution for the αβδγ isoform required two exponentials for fit (Figure 5.3 C). The predominant component for αβδγ corresponded to 0.67 ± 0.30 ms and contributed 75 ± 11% of total events whereas the minor slower component was 2.7 ± 1.1 ms and contributed 25 ± 11% of total events. The overall mean values for both wild-type αβδε and αβδγ receptors were extracted from a large published database generated previously (Mongeon et al., 2011). The burst-duration for the α_{twi}βδγ isoform was well described by a single exponential fit with a mean time constant of 37.28 ± 12.66 ms, reflecting a 56-fold and 14-fold increase over the wild-type αβδγ fast and slow components respectively (Figure 5.3 G).

Single-channel analysis of twister muscle ACh receptors

Single-channel recordings of ACh-activated currents from *twi* $^{+/-}$ fast muscle were used to render assignment of the muscle receptors to specific receptor isoforms.

Unfortunately, it was not possible to record ACh-activated currents from outside-out patches derived from muscle so we turned to on-cell patch recordings. Recordings were first performed on *twi* $^{+/-}$ fish at 48 hpf, the time corresponding to the height of the motility defect and the analysis of synaptic current time course (Figure 5.4 A). The electrode contained 300 nM ACh in order to activate all of the isoforms. Two amplitude classes could be observed with slope conductances of 44.1 and 58.5 pS, corresponding to γ and ε containing receptors respectively (Figure 5.4 A & B). The cumulative burst-duration histograms in Figure 5.4 C were complex and required three exponentials to fit; the mean time constants corresponding to 0.5, 3.4, and 44.8 ms. The individual burst components were next assigned to either ε or γ containing receptors by separating the event classes on the basis of amplitude (Figure 5.4 D & F). The burst-duration for the large amplitude class was fit by two exponentials with time constants of 0.5 and 4.8 ms (Figure 5.4 E). These time constants correspond to the $\alpha\beta\delta\varepsilon$ and $\alpha_{twi}\beta\delta\varepsilon$ receptors heterologously expressed in oocytes. The burst-duration of the small amplitude class (Figure 5.4 F) was also fit by two exponentials with time constants of 1.6 ms and 47.1 ms (Figure 5.4 G), corresponding to the $\alpha\beta\delta\gamma$ (as fit with a single exponential function) and $\alpha_{twi}\beta\delta\gamma$ receptors isoforms.

These results were further validated by single-channel examination of 24 hpf muscle (Figure 5.5). This time point maximizes the expression of γ-containing receptors based on the transcript profile of γ mRNA during early zebrafish development (see Chapter 6). The first recordings of ACh-activated single-channel currents came from *twi* $^{-/-}$ (Figure 5.5 A-C). In these fish lacking wild-type receptors, $\alpha_{twi}\beta\delta\gamma$ were expected

Figure 5.4: ACh-activated single-channel currents from 48 hpf *twi* $^{+/-}$ fish.

(A) A ~3 second sample trace of channel openings to two amplitude levels in the presence of 300 nM ACh. (B) Amplitude histogram for all openings in A required the sum of two Gaussian distributions with means of -3.5 pA and -2.7 pA (*n*=1796 events). (C) The burst-duration histogram for all openings from A, fit to three exponential components corresponding to 0.5 ms, 3.4 ms and 44.8 ms. (D) The distribution of large amplitude openings used to generate the burst-duration in E (*n*=1065 events). (E) The burst-duration for large amplitude events was fit with two exponential components corresponding to 0.5 ms and 4.8 ms. (F) The distribution of small amplitude openings used to generate the burst-duration in G (*n*=731 events). (G) The burst-duration for small amplitude events was fit with two exponential components corresponding to 1.6 ms and 47.1 ms.

Figure 5.4

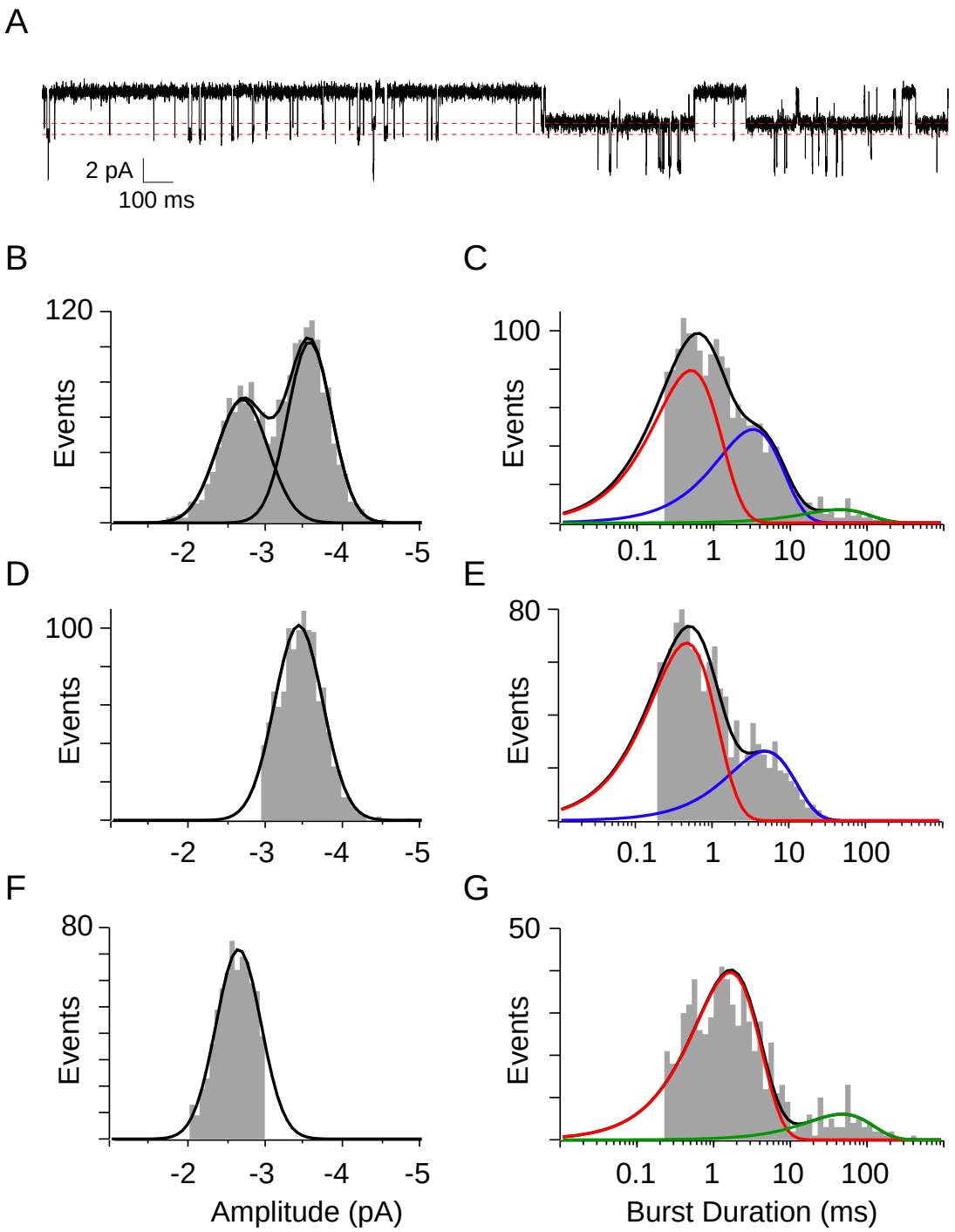
A
2 pA
100 ms
B
120
Events
-2
-3
-4
-5
C
100
Events
0.1
1
10
100
D
100
Events
-2
-3
-4
-5
E
80
Events
0.1
1
10
100
F
80
Events
-2
-3
-4
-5
Amplitude (pA)
G
50
Events
0.1
1
10
100
Burst Duration (ms)

Figure 5.5. Cell-attached ACh-activated single-channel currents from 24 hpf and 120 hpf *twister* muscle.

Sample traces of ACh activated channels in (A) 24 hpf *twi* $^{-/-}$, (D) 24 hpf *twi* $^{+/-}$ and (G) 120 hpf *twi* $^{+/-}$ fish. Amplitude distributions for (B) 24 hpf *twi* $^{-/-}$ and (E) 24 hpf *twi* $^{+/-}$ fish fit to single Gaussian distributions. Example semi-log burst-duration histograms fit to a single exponential function with time constants corresponding to 24.8 ms (*n*=904 events) and 23.8 ms (*n*=970 events) for (C) 24 hpf *twi* $^{-/-}$ and (F) 24 hpf *twi* $^{+/-}$ fish, respectively. (H) Amplitude distribution for 120 hpf *twi* $^{+/-}$ fish fit with a single Gaussian function. (I) Example burst-duration histogram for 120 hpf *twi* $^{+/-}$ fish fit by the sum of two exponential components with time constants corresponding to 0.4 ms and 8.3 ms. (J) Cumulative current-voltage relations comparing 24 hpf *twi* $^{-/-}$ (grey open circles; *n*=7), 24 hpf *twi* $^{+/-}$ (black open circles; *n*=9) and 120 hpf *twi* $^{+/-}$ (filled circles; *n*=10) fish. (K) Mean slope conductance ± SD calculated for 24 hpf *twi* $^{-/-}$ (43.7 ± 4.0 pS), 24 hpf *twi* $^{+/-}$ (44.7 ± 3.1 pS), and 120 hpf *twi* $^{+/-}$ (62.3 ± 3.6 pS) shown alongside individual slope conductance values. A range of 17-140 events was used to calculate each point on the current-voltage relationship. (L) The mean burst-durations ± SD for 24 hpf *twi* $^{-/-}$ (25.6 ± 3.4 ms; *n*=5), 24 hpf *twi* $^{+/-}$(23.2 ± 3.9ms; *n*=5) and 120 hpf *twi* $^{+/-}$ (7.4 ± 1.9 and 0.41 ± 0.12 ms; *n*=10) are shown along with the individual cell averages. A range of 376-1170 events was used to calculate the burst-duration. All data was obtained using 30 nM ACh.

Figure 5.5

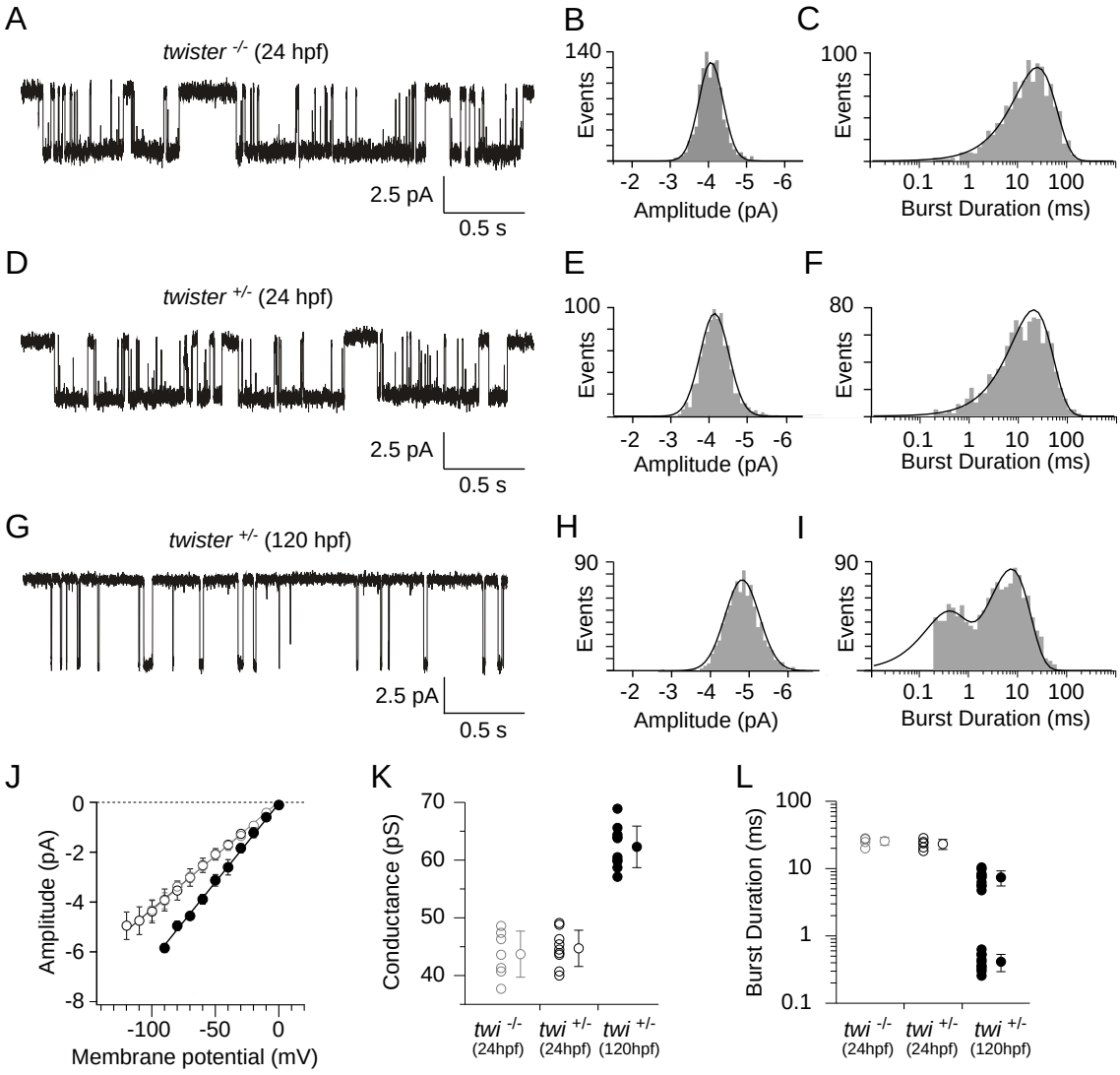
A
twister -/- (24 hpf)
2.5 pA
0.5 s
B
140
Events
-2 -3 -4 -5 -6
Amplitude (pA)
C
100
Events
0.1 1 10 100
Burst Duration (ms)
D
twister +/- (24 hpf)
2.5 pA
0.5 s
E
100
Events
-2 -3 -4 -5 -6
Amplitude (pA)
F
80
Events
0.1 1 10 100
Burst Duration (ms)
G
twister +/- (120 hpf)
2.5 pA
0.5 s
H
90
Events
-2 -3 -4 -5 -6
Amplitude (pA)
I
90
Events
0.1 1 10 100
Burst Duration (ms)
J
0 -2 -4 -6 -8
Amplitude (pA)
-100 -50 0
Membrane potential (mV)
K
70 60 50 40
Conductance (pS)
twi -/- (24hpf)
twi +/- (24hpf)
twi +/- (120hpf)
L
100 10 1 0.1
Burst Duration (ms)
twi -/- (24hpf)
twi +/- (24hpf)
twi +/- (120hpf)

to be the predominant isoform. To maximize the openings at this early stage and minimize desensitization, the recordings were performed using 30 nM ACh (see Chapter 6 for details concerning increased sensitivity of *twister* receptors to ACh).

In each of 7 recordings a single amplitude class was observed (Figure 5.5 A & B) which corresponded to 44 pS (Figure 5.5 J & K), which was not significantly different from the 48 pS value measured for $\alpha_{twi}\beta\delta\gamma$ receptors (p=0.0865; paired t-test). The open burst-duration distribution for this class was well described by a single exponential function with time constant corresponding to 23.18 ± 3.92 ms (Figure 5.5 C & L). Thus, on the basis of slope conductance and burst-duration, this class corresponds to $\alpha_{twi}\beta\delta\gamma$ receptors. Recordings from 24 hpf *twi* $^{+/-}$ fish showed a class with similar amplitude (Figure 5.5 D & E) and conductance (Figure 5.5 J & K). The burst-duration histogram was also fit by a single exponential (Figure 5.5 F) with time constants similar to the homozygous fish (Figure 5.5 L).

Confirmation of the high conductance class assignment to ε-containing receptors was made using 120 hpf *twi* $^{+/-}$ fish; at this stage, most receptors would be expected to contain the ε subunit based on the mRNA expression profile (see Chapter 6). On-cell recordings revealed a single amplitude class of openings (Figure 5.5 G & H), with a slope conductance that corresponded to 62 pS (Figure 5.5 J & K). The burst-duration of this class required two exponentials to fit with mean time constants corresponding to 0.41 ± 0.12 ms and 7.38 ± 1.86 ms (Figure 5.5 I & L). These likely reflect mixed openings by $\alpha_{twi}\beta\delta\varepsilon$ and $\alpha\beta\delta\varepsilon$ receptors on the basis of conductance and burst-duration.

Conclusions Chapter V:

- Each of the three kinetic components of the synaptic decays is represented by a unique class of ACh receptor on the muscle cell.
- Comparison of single-channel conductance and burst-duration of heterologously expressed isoforms to on-cell muscle receptors identified a candidate ACh receptor isoforms that underlie each of the three kinetic components of the synaptic decay at 48 hpf:
    1. τ_{fast} is likely due to a mixture of wild-type $\alpha\beta\delta\varepsilon$ and $\alpha\beta\delta\gamma$ receptors
    2. $\tau_{intermediate}$ is likely due to the $\alpha_{twi}\beta\delta\varepsilon$ receptor isoform
    3. τ_{slow} is likely due to the $\alpha_{twi}\beta\delta\gamma$ receptor isoform

CHAPTER VI

Effects of *twister* mutation on receptor gating

General overview

Receptor gating models

The prolonged burst-duration of the *twister* receptor isoform is likely responsible for the prolonged synaptic decay in muscle cells that leads to aberrant behavior. It is the prolonged burst-duration that links the dysfunction in *twister* to other SCS-causing ACh mutations. As with other SCS-causing mutations, however, the burst-duration is not the only aspect of channel function that is altered in *twister* receptors. To understand the different aspects of channel behavior that are impacted by the *twister* mutation it is useful to consider a more detailed scheme of channel function.

The state diagram to represent ACh receptor function began as a simple scheme, known as the linear model (del Castillo and Katz, 1957; Adams, 1975; Reviewed in Adams 1981):

$$A + R \underset{k_{-1}}{\overset{2k_1}{\rightleftharpoons}} A + AR \underset{2k_{-2}}{\overset{k_2}{\rightleftharpoons}} A_2R \underset{\alpha}{\overset{\beta}{\rightleftharpoons}} A_2R^*$$

This model implies that the transition of the receptor from the unliganded state (R), to the active, or open state (R*) is composed of a certain number of discrete steps. Furthermore, it makes the important distinction between the association of agonist with the receptor (occupation) and receptor opening (Stephenson, 1956; del Castillo and Katz, 1957). This model encompasses situations where the receptor transitions from a

closed to open state by binding ligand. These kinetic processes can be described by a series of rate constants and channel states, and in the linear scheme, includes the two ligand binding (k_1 and k_2) and unbinding (k_{-1} and k_{-2}) rate constants, as well as the rate constants for the transitions between the open and closed conformations (α and β). Early studies on the ACh receptor indicated that binding of 2 ACh molecules was required to activate the receptor (Adams, 1975; Dionne et al., 1978). This was subsequently confirmed when two copies of the α subunit were found associated with purified receptor (Reynolds and Karlin 1978). Studies using active site labels like alpha bungarotoxin (α-btx) also confirmed the presence of two binding sites, both present on the α subunit.

The same year, Katz and Thesleff reported the details of a third functional state, the desensitized state, where the receptor becomes non-reactive when exposed to a steady 'conditioning' pulse of agonist (Katz and Thesleff, 1957). Therefore, the linear model must include the desensitization state (A_2R^D):

$$A + R \underset{k_{-1}}{\overset{k_1}{\rightleftharpoons}} A + AR \underset{k_{-2}}{\overset{k_2}{\rightleftharpoons}} A_2R \underset{\alpha}{\overset{\beta}{\rightleftharpoons}} A_2R^* \underset{k_{-D}}{\overset{k_{+D}}{\rightleftharpoons}} A_2R^D$$

Soon, however, competitive binding assays indicated that one binding site had an approximately 100-fold greater affinity for ACh than the other (Sine et al., 1994). This was difficult to explain, given that the α subunits were identical. Arthur Karlin and his associates resolved this apparent paradox when they found that ACh binding occurred at the interface of the α subunit and its neighboring subunit; the affinity was

conferred by differences between the αδ interface binding region and the αε or αγ region.

Non-liganded and singly-liganded channel opening

According to the linear model, the AChR can only adopt the open conformation (R*) when two agonist molecules are bound, and these transitions must occur in succession. Katz and Thesleff recognized that these linear schemes were insufficient to account for experimental measurements for the onset and recovery from desensitization; this observation led to the first proposition of a cyclical model for the transition of the AChR between functional states (Katz and Thesleff, 1957). The cyclic model appears below, in a form referred to as the Monod-Wyman-Changeux (MWC) model (Monod et al., 1965):

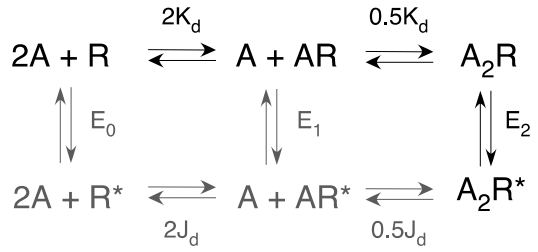

The MWC model contains the original linear model (highlighted in black) and includes two additional transitions to R* (highlighted in gray) one where the ACh receptor is not occupied by ligand, and a second when a single molecule of ACh is bound. Meyer Jackson provided the first experimental evidence for the non-liganded openings of an ACh receptor during single-channel patch clamp recording of embryonic mouse muscle (Jackson, 1984). It is not surprising that these states were absent from the first linear

models, because for the adult wild-type form of the receptor, these transitions occur rarely. Indeed, the probability of this transition remains low for the embryonic receptor studied by Jackson (Jackson et al, 1986; Jackson 1989). Singly liganded receptor openings can be observed at low ACh concentrations, and these openings can form an additional (albeit very brief in duration) component of the open burst-duration histogram (Jackson et al, 1986).

The MWC model has led to the development of the concept of 'gating equilibrium' to provide a more complete description of the transitions between R and R* (Auerbach 2003; Changeux 2011; Auerbach 2012). In the cyclic model, E_0 is referred to as the non-liganded gating equilibrium constant, E_2 is the di-liganded equilibrium constant and K_d and J_d are the equilibrium dissociation constants (Grosman and Auerbach, 2000a,b; Jadey et al., 2011). The di-liganded equilibrium gating constant (E_2) is defined as the ratio of the forward and backward opening rate constants (β/α) and represents the product of E_0 and λ (where λ equals the ratio of K_d/J_d the equilibrium dissociation constants; Jadey et al., 2011).

For wild type receptors, transitions to R* in the absence of agonist occur with a very low probability, because the closed conformation is energetically favored, hence a very low value for E_0 and E_1 (Purohit and Auerbach, 2009; Auerbach, 2010). Therefore, these states have a negligible effect on wild type synaptic transmission. When mutations arise in AChR subunits, however, several changes to receptor function can arise. In human SCS mutations, increases in apparent affinity (Ohno et al., 1995; Engel et al., 1996; Milone et al., 1997), the efficacy of weak agonists and competitive

antagonists (Milone et al., 1997) and spontaneous openings (Ohno et al., 1995; Engel et al., 1996; Grosman and Auerbach, 2000b) have all been reported for the AChR. These changes are proposed to result from changes in the di-liganded (E_2) and non-liganded (E_0) gating equilibrium constants (Jackson, 1984; Jackson, 1986; Grosman and Auerbach, 2000b).

The experiments presented in the previous chapter demonstrated that the burst duration of and AChR containing the L258P mutation was prolonged. In this chapter, my approach will be to investigate whether this mutation renders the AChR more sensitive to ACh, if molecules other than ACh, such as a weak agonists can gate the AChR, and if the probability of spontaneous openings are increased. These functional properties have been reported for other SCS-causing mutations and could potentially play a role in the synaptic and behavioral defects of *twister* fish. The implications of these alterations to the receptor function in patients with SCS are discussed in the final chapter.

Results

The effect of the L258P mutation on sensitivity to ACh

Macroscopic current responses to applied ACh were used to generate dose-response curves for oocytes expressing each of these different receptor isoforms. To do this, ACh was perfused over the entire oocyte with full solution exchange typically occurring in 1-2 sec. At this perfusion rate, it is likely that a fraction of the receptors were desensitized by the peak of the observed current response, particularly at the higher concentrations. Therefore, although we refer to responses as peak current

amplitude, they more accurately represent steady-state activation at a given ACh concentration. The sensitivity of *twister* containing receptors to ACh was much greater than wild type, as evidenced by the left shift in the dose-response curve for $\alpha_{twi}\beta\delta\varepsilon$ and $\alpha_{twi}\beta\delta\gamma$ (Figure 6.1). The dose-response data were fit using the Hill equation and half-maximum values were determined for each isoform (Figure 6.1). The average half-saturating ACh concentrations for wild-type $\alpha\beta\delta\gamma$ and $\alpha\beta\delta\varepsilon$ receptors corresponded to 2.4 µM and 1.7 µM, respectively. By contrast, the dose-response curves for all receptor isoforms containing two α_{twi} subunits were shifted to lower concentrations. The mean half-maximum concentration corresponded to 12 nM for $\alpha_{twi}\beta\delta\gamma$ and 39 nM for $\alpha_{twi}\beta\delta\varepsilon$. Overall, this reflected a 200-fold increase in apparent sensitivity to ACh for $\alpha_{twi}\beta\delta\gamma$ and a 44-fold increase for $\alpha_{twi}\beta\delta\varepsilon$. This increased sensitivity was seen at the single-channel level as well (see Chapter 5).

Spontaneous receptor openings

Alterations in the gating equilibrium were first suggested by single-channel recordings of twister $\alpha\beta\delta\gamma$ channels in outside-out patches from oocytes. I consistently observed openings by both $\alpha_{twi}\delta\gamma$ and $\alpha_{twi}\beta\delta\varepsilon$ receptors in the absence of ACh. These recordings utilized a recording chamber and perfusion system where ACh or choline had not been previously introduced. At the single-channel level, non-liganded openings corresponding to either $\alpha\beta\delta\varepsilon$ or $\alpha\beta\delta\gamma$

Figure 6.1: Dose-response curves obtained for receptor subunit combinations expressed in *Xenopus* oocytes.

Oocytes expressing either $\alpha\beta\delta\gamma$ (red), $\alpha\beta\delta\varepsilon$ (black), $\alpha_{twi}\beta\delta\gamma$ (green) or $\alpha_{twi}\beta\delta\varepsilon$ (blue) were voltage-clamped at -50 mV and current responses to different ACh concentrations were determined. Each point represents the mean ± SD of the percent of peak current measured for 6-7 oocytes at each ACh concentration. The dose-response relationships between peak ACh-activated current and ACh concentration were fit to the Hill equation $I = I_{max} / (1 + (K_{1/2}/[A])^n)$, where I is the current at a given concentration of agonist A, I_{max} is the peak ACh-activated current, $K_{1/2}$ is the half-maximal concentration, and n is the Hill coefficient.

Figure 6.1

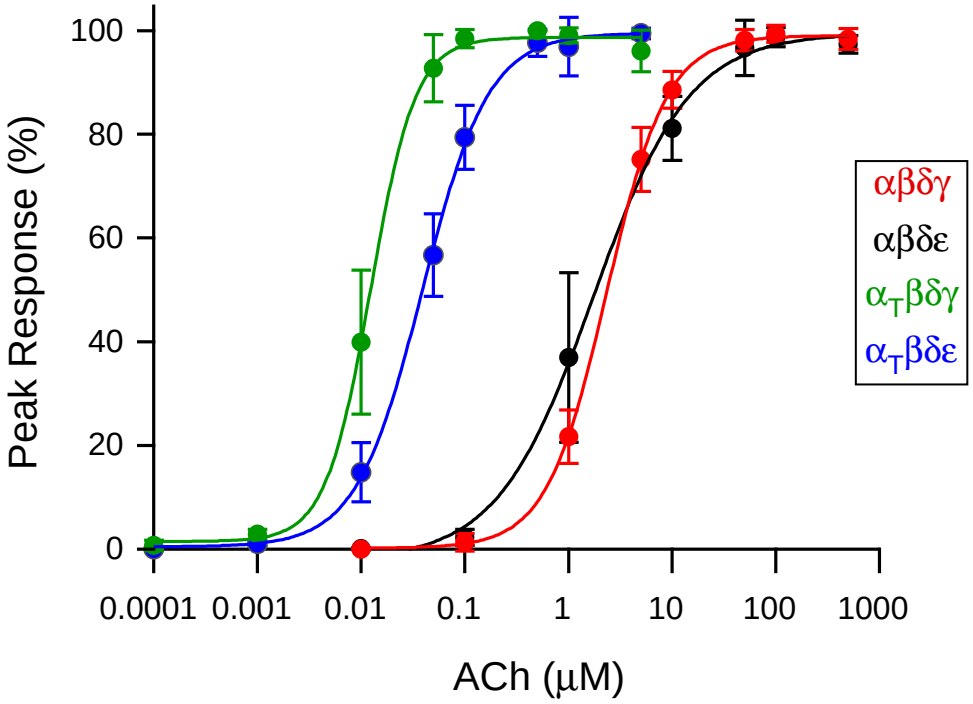
Peak Response (%)
100
80
60
40
20
0
0.0001
0.001
0.01
0.1
1
10
100
1000
ACh (μM)
αβδγ
αβδε
αTβδγ
αTβδε

receptors were too rare to be annotated. The frequency of the openings for $\alpha_{twi}\beta\delta\gamma$ however, was appreciable (Figure 6.2). The burst-duration was brief in the absence of ACh compared to that seen in the presence of ACh, likely reflecting further stabilization of the open state in the presence of ACh (Figure 6.2 A). The openings in the absence of ACh points towards altered gating rather than altered binding as responsible for increased sensitivity to ACh (Jackson, 1984).

Next, I searched for evidence of a macroscopic equivalent of non-liganded ACh receptor openings in oocytes expressing $\alpha_{twi}\beta\delta\gamma$ receptors. If mutant receptors are often open in the absence of ACh, I expected there might be a standing current. As a measure of non-liganded openings, I tested two blockers of ACh receptors, the open-channel blocker quinidine and the irreversible blocker α-bungarotoxin (α-BTX). α-BTX was tested at 1 µM, while quinidine was tested at 100 µM corresponding to 20-fold higher concentration than used previously in single-channel studies (Fukudome et al., 1998). This quinidine concentration was chosen in order to provide maximal block of spontaneous receptor openings by use of a slow channel blocker. In oocytes expressing either $\alpha\beta\delta\gamma$ or $\alpha\beta\delta\varepsilon$ receptors, neither agent had an effect on the holding current (Figure 6.2 C). By contrast, both agents led to large decreases in holding current in oocytes expressing $\alpha_{twi}\beta\delta\gamma$ receptors (Figure 6.2 B-D). Pretreatment with α-BTX occluded the effects of quinidine, demonstrating that the two agents were working through the same population of ACh receptors (Figure 6.2 D). To estimate the fraction of total available ACh-activated current contributed by spontaneous openings, we first determined the amplitude of quinidine-sensitive holding current, then washed out the

Figure 6.2: Openings by non-liganded $\alpha_{twi}\beta\delta\gamma$ receptors expressed in *Xenopus* oocytes. (A) Example outside-out patch recording of $\alpha_{twi}\beta\delta\gamma$ receptors before (top trace) and after (bottom trace) addition of ACh. (B) Recordings of macroscopic current in oocytes expressing $\alpha_{twi}\beta\delta\gamma$ and held at -50 mV. Shown are the baseline current in the absence of ACh, the decrease in holding current upon addition of 100 μM quinidine (arrow) and, following wash out of the quinidine, the large inward current that occurred following addition of 300 nM ACh (arrow). (C) Overall comparisons of the effect of quinidine to reduce the baseline holding current of oocytes expressing the different receptor isoforms. The fractional peak current was determined on the basis of reduction in holding current in the presence of 100 μM quinidine relative to peak ACh-activated current (following washout of quinidine). The mean ± SD are shown and the number of oocytes tested is indicated. (D) Representative traces from an oocyte expressing $\alpha_{twi}\beta\delta\gamma$ receptors demonstrating the decrease in holding current in response to application of either 1 μM α-BTX (black trace) or 100 μM quinidine. The response to the first application of quinidine was allowed to recover before the oocyte was treated with α-BTX. Following treatment with α-BTX, the oocyte showed no response to further application of quinidine (grey arrow).

Figure 6.2

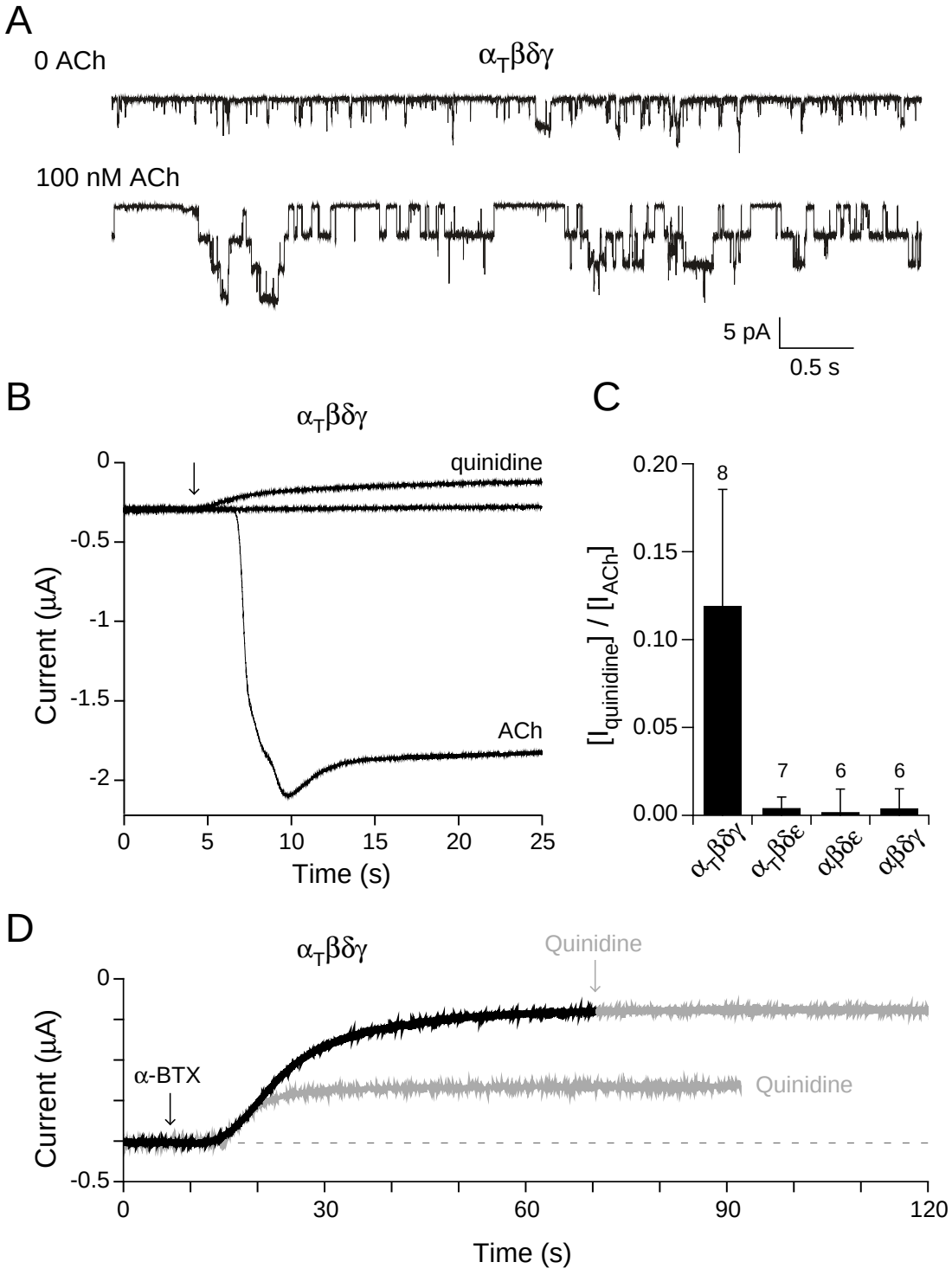
A
0 ACh
$\alpha_T\beta\delta\gamma$
100 nM ACh
5 pA
0.5 s
B
$\alpha_T\beta\delta\gamma$
quinidine
ACh
Current (μA)
Time (s)
C
$[I_{quinidine}] / [I_{ACh}]$
8
7
6
6
$\alpha_T\beta\delta\gamma$
$\alpha_T\beta\delta\varepsilon$
$\alpha\beta\delta\varepsilon$
$\alpha\beta\delta\gamma$
D
$\alpha_T\beta\delta\gamma$
Quinidine
α-BTX
Quinidine
Current (μA)
Time (s)

quinidine and applied 300 nM ACh to activate all available receptors (Figure 6.2 D). The ratio of quinidine-sensitive holding current to peak ACh-activated current for $\alpha_{twi}\beta\delta\gamma$ averaged 0.12 ± 0.07 (*n*=8; Figure 6.2 C). This ratio is remarkably high in light of the fact that the burst-duration for spontaneous events is much briefer than in the presence of ACh (Figure 6.2 A). Only small decreases in holding current were observed following quinidine treatment for $\alpha_{twi}\beta\delta\varepsilon$ receptors.

Agonist and antagonist receptor gating

Choline, a weak agonist of muscle nicotinic receptors, was tested for activation of mutant receptors (Figure 6.3). Application of 1 mM choline to oocytes expressing wild-type receptors resulted in weak fractional activation corresponding to 0.04 ± 0.01 for $\alpha\beta\delta\gamma$ and 0.03 ± 0.02 for $\alpha\beta\delta\varepsilon$ (Figure 6.3 B). By contrast, application of choline to either $\alpha_{twi}\beta\delta\gamma$ or $\alpha_{twi}\beta\delta\varepsilon$ receptor isoforms resulted in strong activation of inward current (Figure 6.3 A & B). The fractional activation for $\alpha_{twi}\beta\delta\gamma$ and $\alpha_{twi}\beta\delta\varepsilon$ receptors corresponded to 0.92 ± 0.05 and 0.95 ± 0.04, which were both comparable to ACh activation (Figure 6.3 B).

The antagonist d-tubocurare (curare) was also tested for partial agonist action (Figure 6.3 A). Application of 10 µM curare failed to significantly activate either $\alpha\beta\delta\gamma$ or $\alpha\beta\delta\varepsilon$ receptors (Figure 6.3 B). However, significant responses were observed for both $\alpha_{twi}\beta\delta\gamma$ and $\alpha_{twi}\beta\delta\varepsilon$ receptor isoforms (Figure 6.3 A & B). The mean fractional activation corresponded to 0.17 ± 0.08 for $\alpha_{twi}\beta\delta\gamma$ and 0.35 ± 0.09 for $\alpha_{twi}\beta\delta\varepsilon$ receptors (Figure 6.3 B).

Figure 6.3: Activation of receptors isoforms by ACh, choline, and curare.

(A) Example recording of macroscopic currents in an oocyte expressing $\alpha_{twi}\beta\delta\gamma$ and held at -50 mV. Application of 10 μM curare, 1 mM choline or 300 nM ACh effectively evoked an inward current. (B) Overall comparisons of activation by choline (black) and curare (gray) on each of the different receptor isoforms. The bar graph reflects the mean fractional activation ± SD of peak ACh-activated current and the number of oocytes tested is indicated.

Figure 6.3

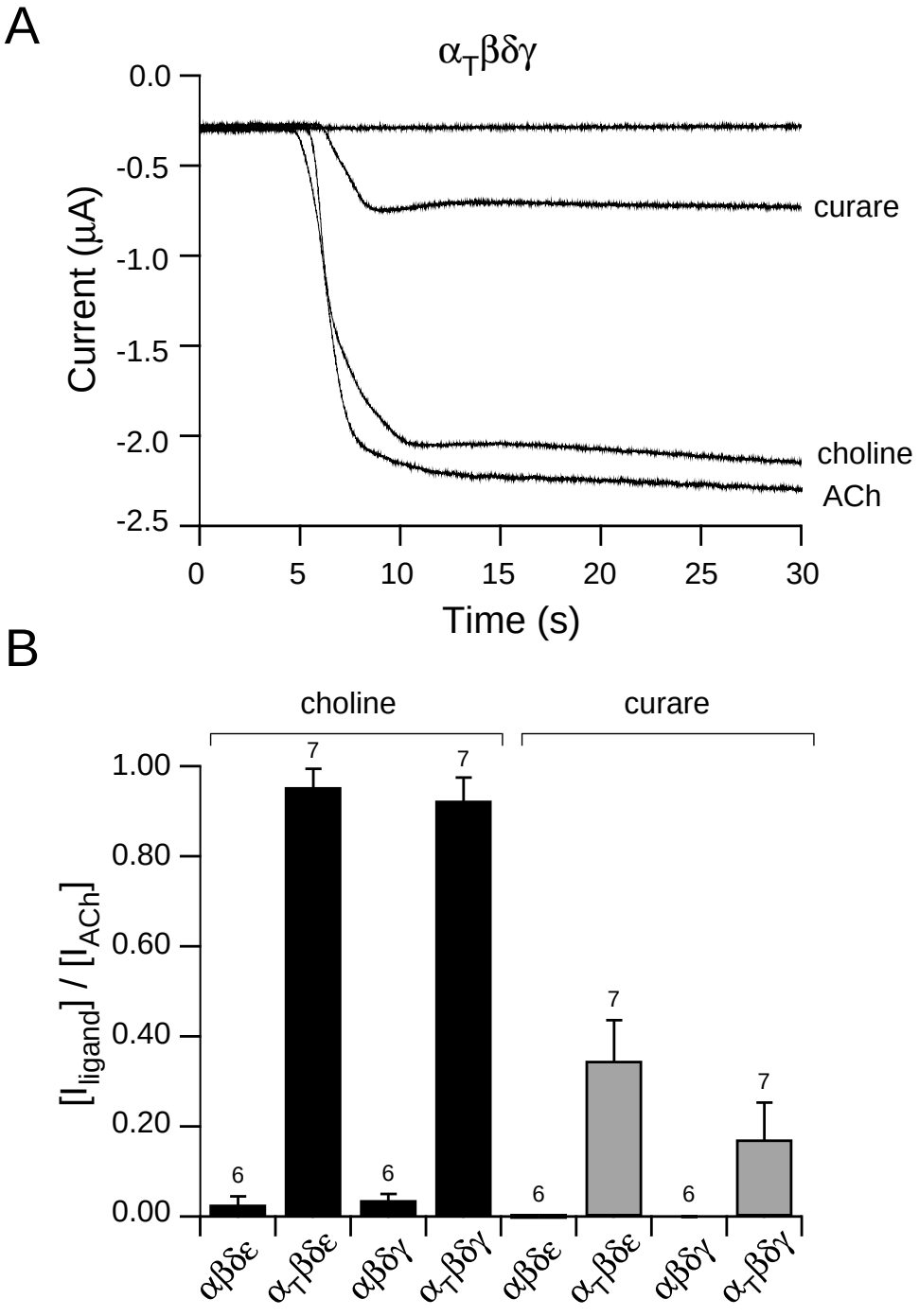
A
$\alpha_T\beta\delta\gamma$
0.0
-0.5
-1.0
-1.5
-2.0
-2.5
Current (μA)
curare
choline
ACh
0
5
10
15
20
25
30
Time (s)
B
choline
curare
1.00
0.80
0.60
0.40
0.20
0.00
$[I_{ligand}] / [I_{ACh}]$
7
7
7
6
6
6
6
αβδε
$\alpha_T\beta\delta\varepsilon$
αβδγ
$\alpha_T\beta\delta\gamma$
αβδε
$\alpha_T\beta\delta\varepsilon$
αβδγ
$\alpha_T\beta\delta\gamma$

Conclusions Chapter VI:

The *twister* mutation imparts a shift in gating equilibrium that destabilizes the closed state of the channel and increases the likelihood of achieving the open state.

- *twister* ACh receptors have an increased apparent affinity (44 and 200-fold) for ACh
- *twister* ACh receptors, in particular the γ isoform, are spontaneously open (greater than 10% of the total steady state current)
- Both ε and γ isoforms of *twister* ACh receptors open in response to the weak agonist choline
- Both ε and γ isoforms of *twister* ACh receptors are partially activated by the competitive antagonist d-tubocurare.

Chapter VII:

Recovery

General overview

At the onset of this work, I found that the most fascinating aspect of the *twister* mutant line was the recovery process that these animals undergo during the first week of development. Understanding this 'self-healing' process held the potential for a new therapeutic treatment for SCS and elucidating this mechanism has remained the focus of my dissertation work. Experiments in the previous chapters were aimed at characterizing the alterations in both synaptic transmission and single-channel function that are brought about by the *twister* mutation. Experiments in this chapter will explore the electrophysiological and molecular aspects of the behavioral recovery process that was discussed and quantified in Chapter 3 as well as directly test possible mechanisms that are causal to the improved swimming.

Results

Synaptic recovery

Electrophysiological recordings were performed on *twi* $^{+/-}$ muscle at two additional developmental time points, 72 and 120 hpf, chosen on the basis of the motion analysis performed in Chapter 2. These recordings revealed that synaptic current decays are gradually accelerated during the developmental period during which the recovery process occurs (Figure 7.1). This raised the possibility that changes in

Figure 7.1. Developmental acceleration of synaptic current decay in *twi* $^{+/-}$ fish.

Three normalized mEPCs are shown for each of the indicated developmental time points. The synaptic currents were aligned at the beginning on the rising phase.

Figure 7.1

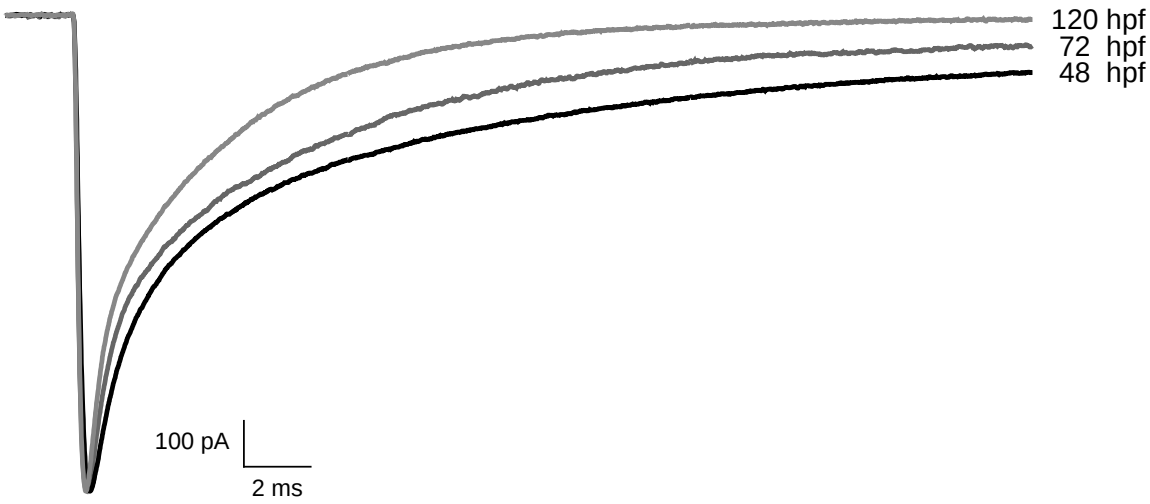

synaptic current decay could account for the improved swimming and the behavioral recovery.

Synaptic current decays were analyzed in an identical manner to those presented in Chapter 4, and all events were fit using three exponential components. (Figure 7.2 A-C). Fit in this manner, the mean time constants at 48 hpf corresponded to 1.06 ± 0.29 ms for τ_f, 8.64 ± 2.53 ms for τ_i and 70.21 ± 22.04 ms for τ_s (Figure 7.2 D & H) Table 7.1; *n*=14 recordings). The average fractional contribution to the decay was 0.45 ± 0.09 for τ_f, 0.40 ± 0.09 for τ_i, and 0.15 ± 0.08 for τ_s (Figure 7.2 D & G). At 72hpf, τ_f corresponded to 0.78 ± 0.36 ms, τ_i corresponded to 7.18 ± 1.56 ms and τ_s corresponded to 69.81 ± 29.67 ms (Figure 7.2 E & H; Table 7.1; *n*=22 recordings) . The average fractional contribution to the decay was 0.40 ± 0.08 for τ_f, 0.51 ± 0.10 for τ_i, and 0.09 ± 0.04 for τ_s (Figure 7.2 E & G). At 120 hpf, τ_f corresponded to 0.51 ± 0.09 ms, τ_i corresponded to 5.54 ± 0.93 ms and τ_s corresponded to 67.62 ± 11.39 ms (Figure 7.2 F & H; Table 7.1; *n*=11 recordings). The average fractional contribution to the decay was 0.49 ± 0.09 for τ_f, 0.50 ± 0.09 for τ_i, and 0.02 ± 0.01 for τ_s (Figure 7.2 F & G). The values for each of the decay constants are summarized in Table 7.1.

These recordings revealed a downward trend in the fractional contribution by τ_s. The reduction from 48 to 72 hpf is statistically significant (p=0.0201; unpaired two-tailed t-test) while the reduction from 48 to 120 hpf is extremely statistically significant (p<0.0001; unpaired two-tailed t-test; Figure 7.2 G). By 120 hpf, τ_s accounts for less than 2% of the total amplitude of the mEPC when the decay is fit with a triple exponential function. The decay of most synaptic currents in these animals could also

Figure 7.2. Developmental acceleration in synaptic current decay in *twi* $^{+/-}$ fish results from a loss of the slow component of decay.

The same sample mEPCs from 48 hpf (A), 72 hpf (B) and 120 hpf (C) *twi* $^{+/-}$ fish fit by the sum of 2 (left trace) versus 3 (right trace) exponential components. The mEPC decay is shown in black and the sum of the fitted exponentials is shown in red. The mean time constants and fractional amplitude contribution for the τ_f (red), τ_i (blue) and τ_s (green) components are shown for each recording at 48 hpf (D), 72 hpf (E) and 120 hpf (F). The overall means ± SD for each distribution are shown in black. (G). Histogram of overall mean ± SD values of fractional amplitudes showing a significant reduction in the slow component (green) at 72 hpf (* p=0.0201; paired two tailed t-test) and extremely statistically significant at 120 hpf (** p<0.0001; paired two tailed t-test). (H). The time constants for τ_f (red), τ_i (blue) and τ_s (green) at 48 hpf, 72 hpf and 120 hpf.

Figure 7.2

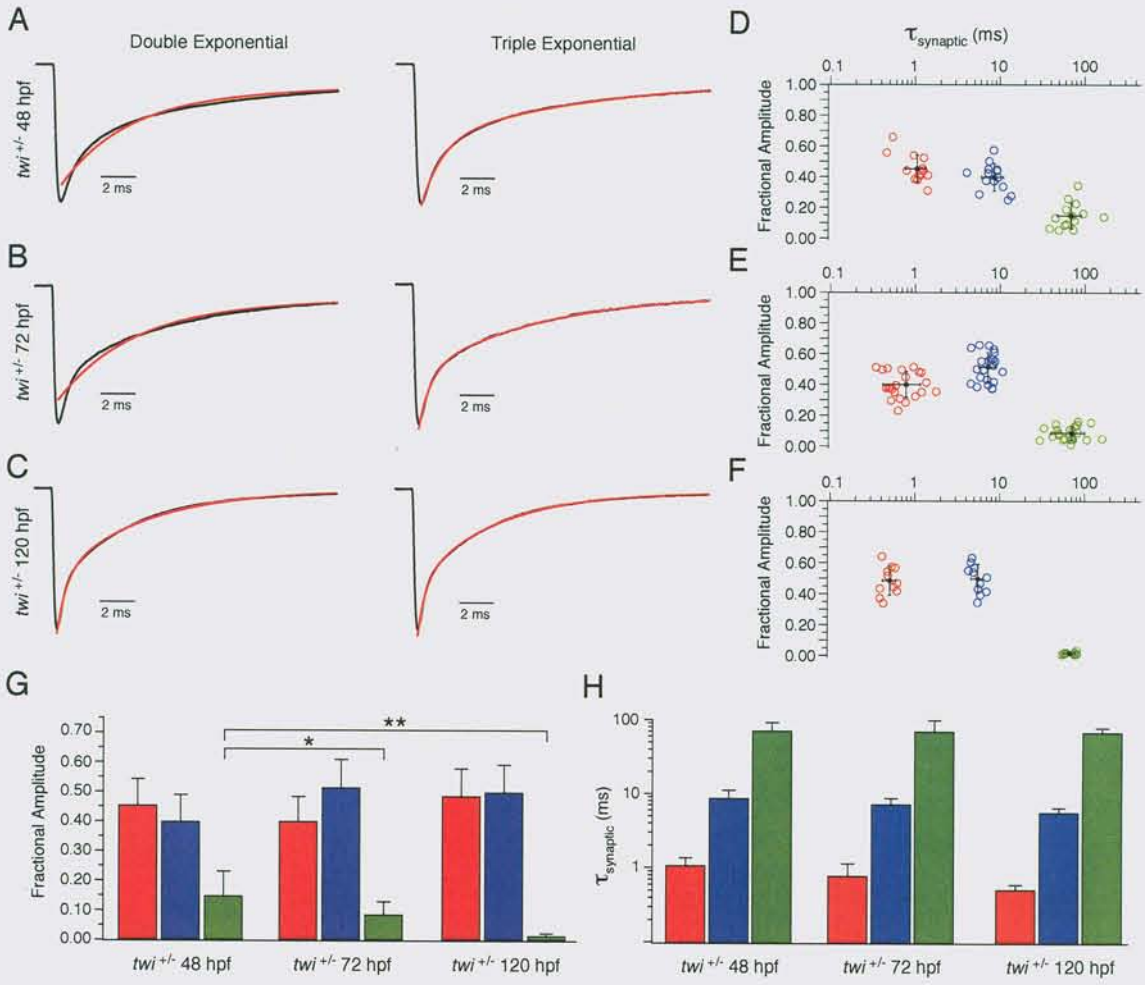
A
Double Exponential
Triple Exponential
twi +/- 48 hpf
2 ms
B
twi +/- 72 hpf
C
twi +/- 120 hpf
D
τsynaptic (ms)
0.1
1
10
100
Fractional Amplitude
1.00
0.80
0.60
0.40
0.20
0.00
E
F
G
0.70
0.60
0.50
0.40
0.30
0.20
0.10
0.00
*
**
twi +/- 48 hpf
twi +/- 72 hpf
twi +/- 120 hpf
H
100
10
1
τsynaptic (ms)

Table 7.1: Characteristics of *twi*$^{+/-}$ fast muscle mEPC analysis at three developmental timepoints

	Decay Time constant (ms)			Fractional Contribution		
	τ_{fast}	$\tau_{intermediate}$	τ_{slow}	Fast	Intermediate	Slow
twi$^{+/-}$ 48 hpf	1.06 ± 0.29	8.61 ± 2.53	70.21 ± 22.03	0.45 ± 0.09	0.40 ± 0.09	0.15 ± 0.08
twi$^{+/-}$ 72 hpf	0.78 ± 0.36	7.18 ± 1.56	69.81 ± 29.67	0.40 ± 0.08	0.51 ± 0.10	0.09 ± 0.04
twi$^{+/-}$ 120 hpf	0.50 ± 0.09	5.54 ± 0.93	67.62 ± 11.39	0.49 ± 0.09	0.50 ± 0.09	0.02 ± 0.08

be well fit by two exponentials, corresponding to τ_f and τ_i measured for the triple exponential fit (values not shown; Figure 7.2 C). Fitting synaptic currents at 48 or 72 hpf with two exponential components results in a poor fit, especially at the peak and end of the decay (Figure 7.2 A & B).

The acetylcholinesterase hypothesis

Experiments presented in Chapter 6 demonstrate that receptors containing the α_{twi} subunit are sensitive to 44- and 200-fold lower concentrations of ACh than those containing wild-type α subunits. This raises the possibility that τ_s represents the persistent re-opening of mutant receptors by lingering ACh in the synaptic cleft. Re-opening might be especially prevalent at early developmental time points if acetylcholinesterase (AChE) expression is initially low. Previous studies support the occurrence of a developmental increase in AChE levels; it was demonstrated in *Xenopus* that AChE inhibitors had only a small effect on the time course of synaptic events at early developmental stages (Kullberg et al., 1980) and in zebrafish it was found that AChE levels are too low to be detected by fasciculin staining at 48 hpf (Drapeau et al., 2001). A developmental increase in AChE levels would be expected to maintain lower cleft concentrations of ACh and prevent the selective reactivation of mutant receptors, potentially leading to the disappearance of τ_s. It follows, therefore, that if τ_s is due to re-opening of mutant receptors, then it should re-emerge following pharmacological block of AChE at the 120 hpf time point.

To test this hypothesis, I recorded mEPCs from fast muscle cells of 120 hpf animals before and after the addition of neostigmine, an AChE inhibitor. In a small number of recordings, AChE inhibition resulted in an increase in peak current amplitude, the duration of the rising phase of the current, and a two-fold increase in both τ_f and τ_i; however, none of these recordings showed the re-emergence of τ_s. The increases in event amplitude suggest that this effect is not due to a loss of voltage control of the muscle cell, which would as also be expected to result in a prolongation of the time constant of decay. The 2-fold increase in decay time is in good agreement with recordings from the AChE null motility mutant *zieharmonika,* where a similar ~2-fold prolongation was observed for mEPC decay time constants (Mongeon et al., 2011). This finding supports the idea that τ_s is not due to the persistent re-opening of mutant ACh receptors that is eliminated by the developmental increase in AChE expression.

The embryonic receptor hypothesis

Single-channel recordings in Chapter 5 demonstrated that the mean burst-duration for the $\alpha_{twi}\beta\delta\gamma$ ACh receptor is in good agreement with τ_s. The selective reduction in the fractional contribution of τ_s to the synaptic current decay could arise from a selective elimination of the $\alpha_{twi}\beta\delta\gamma$ ACh receptor at the neuromuscular junction during development. This hypothesis is consistent with the findings in other vertebrate systems that demonstrate the embryonic γ subunit is replaced during development by receptors containing an adult ε subunit (Mishina et al., 1986; Owens et al., 1993).

In a collaboration with Drs. Fumihito Ono, Jason Urban, and Rebecca Mongeon, the developmental disappearance of the γ subunit in zebrafish was investigated using quantitative PCR. The abundance of each subunit transcript was measured from total RNA extracts of whole embryos between the ages of 24 and 144 hpf (Figure 7.3). The transcript levels are indicated as the relative abundance (in copy number) of the target transcript compared to the copy number of the control transcript elongation factor 1 (elf1a; see Materials and Methods). Elf1a represents a validated reference gene for qPCR analysis of zebrafish tissue (Tang et al., 2007). Quantitation of transcript levels indicated that the levels ε transcript increased dramatically between 24 and 48 hpf, over which time the γ transcript levels were constant (Figure 7.3). This corresponded to ε/γ ratios of 1.63 at 24 hpf, 4.46 at 48 hpf, 3.99 at 72 hpf, and 8.21 by 144 hpf. This increase in relative abundance of ε transcripts is coincident with the change in synaptic current decay.

I directly tested the idea that decreased γ subunit levels is causal to behavioral recovery by reducing the early expression of the γ subunit using antisense morpholinos. This treatment favors specific assembly of receptors containing the ε subunit. 4 ng of γ subunit morpholino was injected into the fertilized *twister* eggs at the one- or two-cell stage, and the effects on both motility and synaptic currents were tested at 48 hpf (Figure 7.4). Visual inspection revealed that the mEPC decay was much faster in morpholino injected fish than non-injected *twi* $^{+/-}$ fish (Figure 7.4 A). mEPC decays were fit with three exponential components, with average time constants of 0.57 ± 0.13 ms for τ_f, 7.93 ± 0.92 ms for τ_i, and 58.49 ± 15.33 ms for τ_s (*n*=8 recordings). The fractional

Figure 7.3

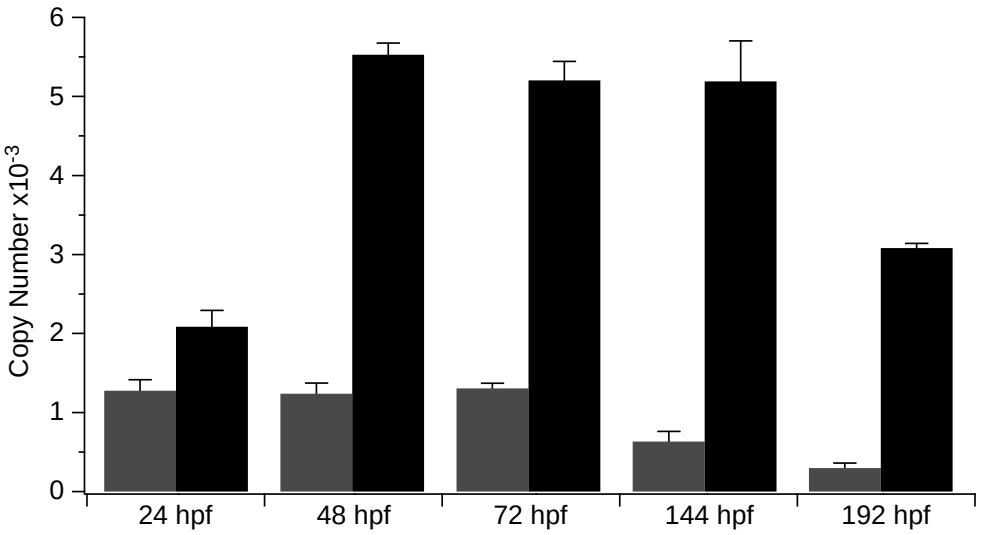

Figure 7.3. Developmental pattern of zebrafish γ and ε subunit expression

Quantitative PCR measurements from cDNA pools of ~20 zebrafish embryos. Target transcript levels are expressed as copy number relative to an elf1a transcript that is expressed uniformly throughout development. Gray boxes denote γ subunit expression and black boxes denote ε subunit expression. Mean ± SD are shown for 3 independent measurements at each indicated time point.

Figure 7.4

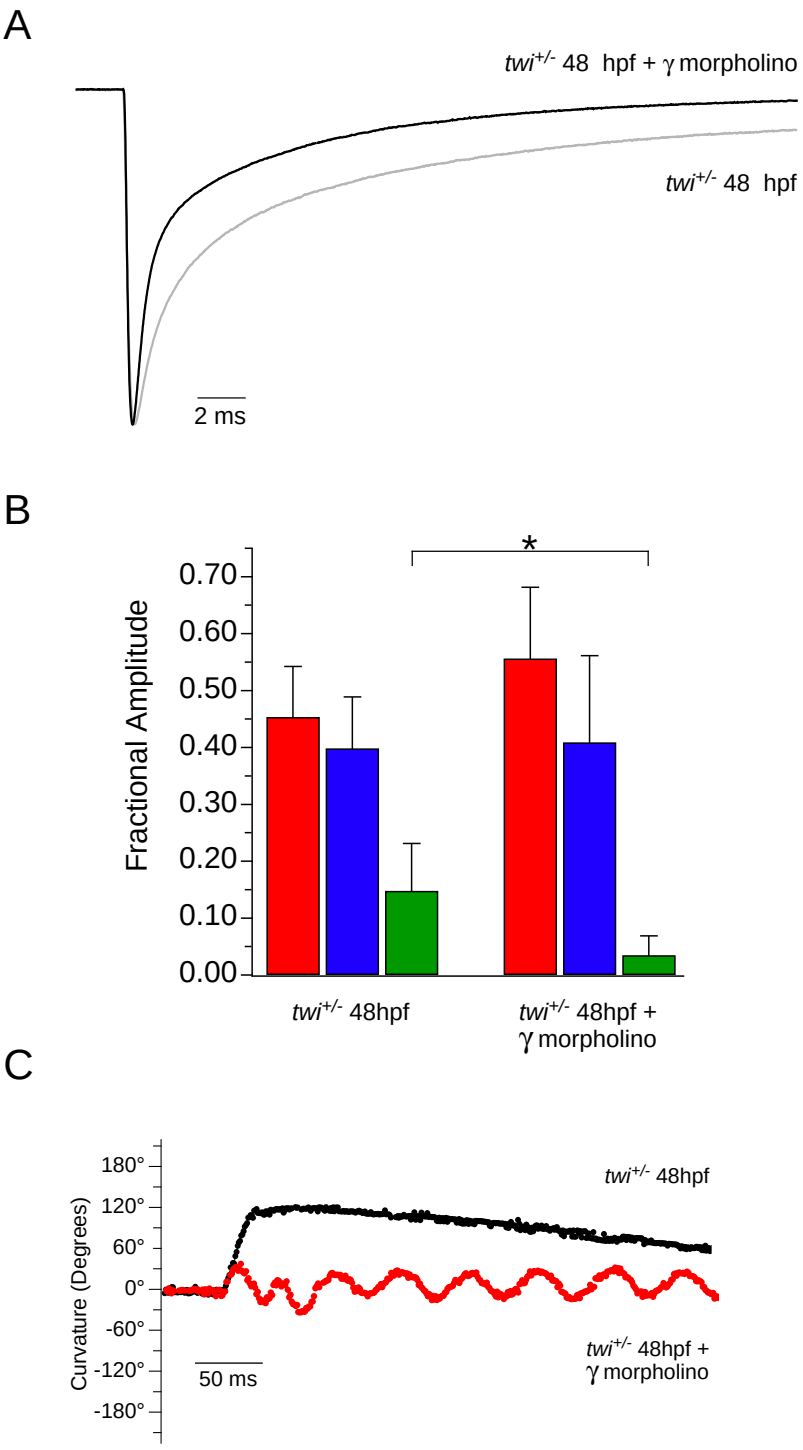
A
twi+/- 48 hpf + γ morpholino
twi+/- 48 hpf
2 ms
B
*
Fractional Amplitude
0.70
0.60
0.50
0.40
0.30
0.20
0.10
0.00
twi+/- 48hpf
twi+/- 48hpf + γ morpholino
C
Curvature (Degrees)
180°
120°
60°
0°
-60°
-120°
-180°
twi+/- 48hpf
twi+/- 48hpf + γ morpholino
50 ms

Figure 7.4. Injection of a γ subunit antisense morpholino in skeletal muscle reduces the slow component of synaptic current decay and improves swimming.

(A) Example normalized mEPCs recorded at from 48 hpf *twi* $^{+/-}$ from non-injected (gray trace) and γ morpholino injected animals. (B) The overall fractional contributions by τ_f (red), τ_i (blue) and τ_s (green) of the exponential fit. The fractional contribution of τ_s was significantly reduced by injection of the γ morpholino (**p*=0.0201 paired t-test) (C) An example spontaneous swim quantified by Flote motion tracking software for a 48 hpf non-injected *twi* $^{+/-}$ fish that is only able to perform a single sustained contraction that lasts on average 703.5 ± 291.8 ms and an 48 hpf *twi* $^{+/-}$ fish injected with 4ng of a γ morpholino. The morpholino injected animal is able to perform bilateral contractions reminiscent of normal swimming behavior.

contribution of τ_f corresponded to 0.56 ± 0.13, τ_i corresponded to 0.41 ± 0.15 and τ_s corresponded to 0.035 ± 0.034. This represents a significant reduction in the fractional contribution of τ_s between the injected and non-injected 48 hpf *twi* $^{+/-}$ (p=0.0201 paired two-tailed t-test; Figure 7.4 B), and is only slightly greater than the remaining τ_s observed in 120 hpf animals (compare Figure 7.2 G).

The effect of reduced γ expression was also examined at the behavioral level by performing motility assays on injected *twi* $^{+/-}$ fish. Non-injected *twister* fish exhibited a maintained contraction (as previously described) whereas morpholino injected *twi* $^{+/-}$ fish were able to mount rhythmic swimming that was similar to, but somewhat slower than 48 hpf wild-type fish (Figure 7.4 C). The findings from both synaptic current and motility measurements show that reduction of γ subunit expression greatly accelerates developmental recovery.

Effect of accelerated synaptic current decay on postsynaptic potential

Experiments presented in Chapter 4 demonstrated that *twi* $^{+/-}$ muscle cells exhibit a prolonged after-depolarization, presumably due to persistent current entry into the muscle cell through the ACh receptor. Acceleration of the synaptic current decay would also be expected to accelerate the repolarization phase of the synaptic potential. To test this hypothesis, Dr. Hua Wen performed paired motor neuron-muscle recordings, recorded the synaptic depolarizations in *twi* $^{+/-}$ muscle in response to neuron firing. Data from this technique at the 48 hpf time point (representing the height of the motility defect) was presented in Chapter 3, and is here compared to the

recovered time point of 120 hpf. Muscle cells were held in voltage clamp at an initial resting potential of -90 mV before switching to the current clamp configuration where a single muscle AP was triggered by stimulating the motor neuron to fire at a frequency of 1 Hz. Between 12 and 20 muscle action potentials were averaged to generate an average waveform for the pair. Repolarization was assessed by measuring the time taken for the holding potential to reach 80% and 90% of the initial resting potential. Repolarization of wild-type muscle cells was rapid, with 80% repolarization occurring in 11.40 ± 0.36 ms and 90% repolarization occurred in 17.29 ± 0.53 ms for 48 hpf animals. In 120 hpf animals, 80% repolarization occurred in 7.00 ± 0.50 ms and 90% repolarization occurred in 11.84 ± 0.71 ms. By contrast, repolarization occurred slowly in 48 hpf *twi* $^{+/-}$ animals, where 80% repolarization occurred in 80.27 ± 19.86 ms (Figure 7.5 A & B; *n*=6 pairs) and 90% repolarization occurred in 136.95 ± 41.44 ms. Repolarization was accelerated in 120 hpf animals, where 80% repolarization occurred after 41.94 ± 4.99 ms and 90% repolarization occurred after 66.40 ± 6.08 ms (Figure 7.5 A & B; *n*=3 pairs).

Effect of accelerated synaptic current decay at physiological swimming frequency

Zebrafish swimming requires muscle cells to follow high-frequency trains of action potentials that are generated by spinal motor neurons. As a test of the muscles ability to fire repetitively, the motor neuron was stimulated at a frequency of 20 Hz, the lower limit for spontaneous slow swims, and the muscle was held in current clamp at an

Figure 7.5 The effects on accelerated synaptic current decay on membrane repolarization.

(A) Averaged fast muscle cell action potential in response to motorneuron firing at a rate of 1 Hz in 48 hpf *twi* $^{+/-}$ (red) and 120 hpf *twi* $^{+/-}$ (black). Between 12 and 20 individual action potentials were averaged to generate the waveform for the pair. (B) 80 and 90% repolarization time for 48 and 120 hpf wild-type and *twi* $^{+/-}$ animals. (C) Muscle cells responses to motorneuron firing at 20 Hz. In 48 hpf animals, the repolarization rate slows with each subsequent stimulation whereas in 120 hpf animals, the rate remains the same.

Figure 7.5

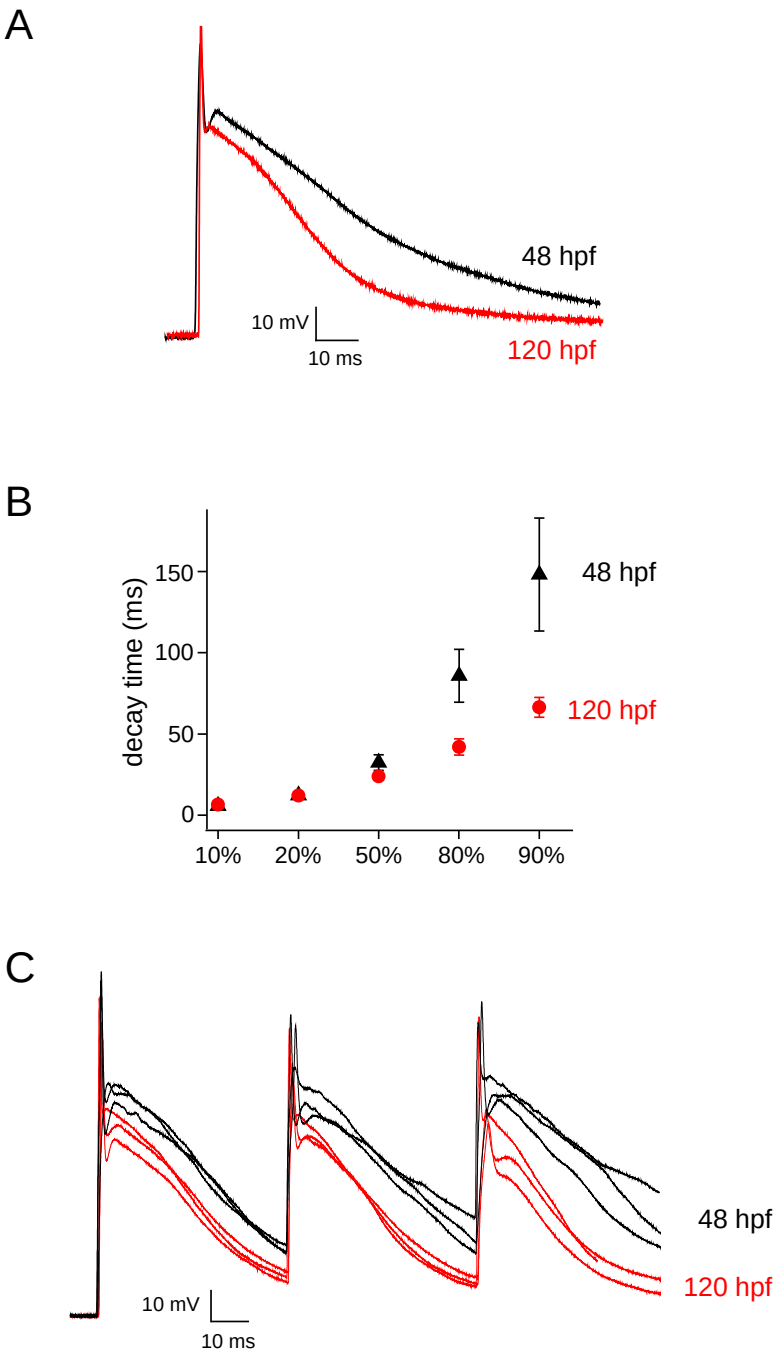
A
48 hpf
10 mV
10 ms
120 hpf
B
decay time (ms)
150
100
50
0
10%
20%
50%
80%
90%
48 hpf
120 hpf
C
10 mV
10 ms
48 hpf
120 hpf

initial holding potential of -90 mV. At 48 hpf, the repolarization rate was prolonged with each successive stimulation, resulting in a persistent standing current. By 120 hpf, the current decay accelerated and repolarization was more rapid, resulting in a faster return to baseline (Figure 7.5 C).

Quinidine effects on synaptic currents and non-liganded receptor openings.

As open-channel blockers such as quinidine are used for clinical treatment of patients afflicted with slow channel syndrome (Harper and Engel, 1998; Fukudome et al., 1998) I was interested to directly test the effects on *twi* $^{+/-}$ fish. First, the effects on swimming were tested before and after treatment with quinidine. As previously presented (Chapter 3) 48 hpf wild-type fish generated alternating contractions following stimulation (Figure 7.6 A, top panel). At this age, *twi* $^{+/-}$ fish were only able to generate a single maintained bend following mechanical stimulation (Figure 7.6 A, bottom). To test for *twi* $^{+/-}$ swimming improvement with quinidine treatment, fish were first placed in bath solution containing a high concentration (50 μM) of quinidine for 10 minutes, followed by placement in drug-free bath solution for testing. The high concentration was used in order to facilitate entry into the live animal from the bath solution. Acute treatment with quinidine markedly improved swimming in *twi* $^{+/-}$ fish, and allowed mutants to perform alternating contractions (like those seen in wild-type fish) in 7 of 10 testing groups (Figure 7.6 A, bottom).

The behavioral improvement with quinidine treatment prompted me to examined the effects of quinidine on *twi* $^{+/-}$ synaptic currents. For this purpose, I

Figure 7.6. Effect of quinidine on swimming and synaptic current decay.

(A) Swimming behavior in 48 hpf wild type (top), *twi* $^{+/-}$ (bottom; black) and *twi* $^{+/-}$ treated with quinidine (bottom; red). (B) Normalized mEPC recorded from *twi* $^{+/-}$ 48 hpf fast muscle cell before and after addition of 10 µM quinidine. Before application the decay was fit by a triple exponential function (red overlay) and after treatment was fit with a single exponential function (red overlay). (C) Scatter plot of individual decay time constants for wild type (black open circles; *n*=6 cells; 87 events), and quinidine treated *twi* $^{+/-}$ (red open circles; *n*=7 cells; 80 events) shown alongside mean ± SD (filled circles) The mean ± SD for the three *twi* $^{+/-}$ time constants (Figure 3.2) is shown as open squares for comparison.

Figure 7.6

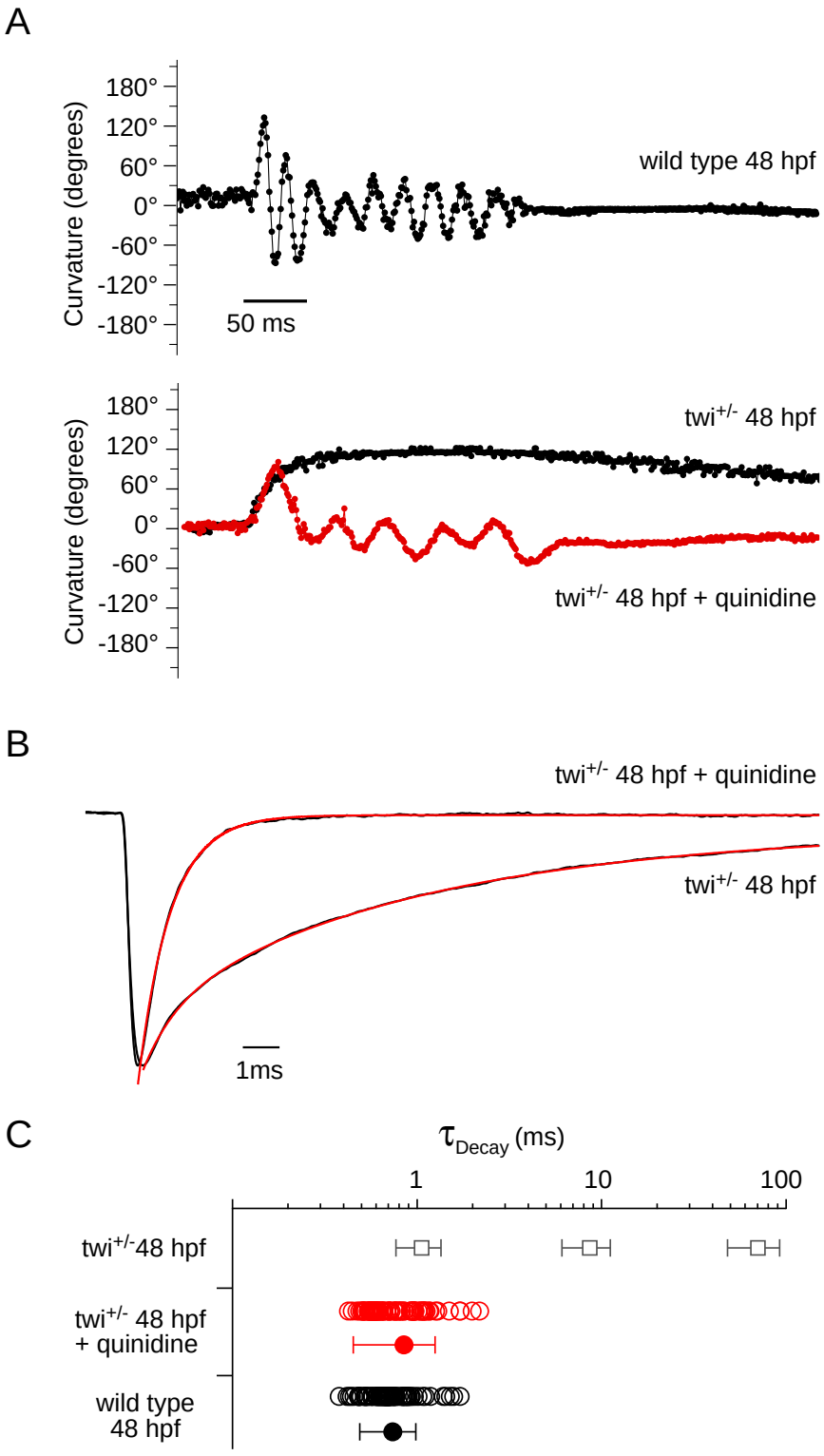
A
180°
120°
60°
0°
-60°
-120°
-180°
Curvature (degrees)
wild type 48 hpf
50 ms
twi+/- 48 hpf
twi+/- 48 hpf + quinidine
B
twi+/- 48 hpf + quinidine
twi+/- 48 hpf
1ms
C
τDecay (ms)
1
10
100
twi+/-48 hpf
twi+/- 48 hpf
+ quinidine
wild type
48 hpf

recorded mEPCs from *twi* $^{+/-}$ fast muscle before and after addition of 10 μM quinidine to the bath solution (Figure 7.6 B). The mean amplitude of spontaneous synaptic currents was reduced, on average, by 45.9% in response to quinidine. However, the most pronounced effect of the treatment was the dramatic acceleration of the decay phase of the synaptic currents (Figure 7.6 B). The triple exponential decay of synaptic currents in the *twi* $^{+/-}$ fish was converted to a decay that followed a single exponential time course with a mean time constant corresponding to 0.85 ± 0.40 ms (Figure 7.6 B & C) after application of quinidine. There was no evidence of a slow or intermediate component of synaptic current decay at this concentration.

Conclusions Chapter VII:

- *twister* behavioral recovery involves a selective loss of the third exponential component of *twi* $^{+/-}$ synaptic decay, and results in faster muscle repolarization after neuronal stimulation.
- Developmental increases in acetylcholinesterase activity does not account for the loss of the third component of synaptic decay.
- The third component of decay is likely due to openings by the $\alpha_{twi}\beta\delta\gamma$ receptor isoform since:
    a. qPCR suggests that developmental decrease in ratio of γ/ε corresponds to the time course of recovery
    b. knockdown of γ subunit expression recapitulates synaptic and behavioral recovery aspects at early ages (48 hpf) that are only normally seen later (120 hpf)
- Treatment of *twister* animals with a current SCS treatment for humans (quinidine) improves the behavioral defect and provides the first demonstration of the drug action on synaptic currents.

Chapter VIII

Discussion

Slow channel syndrome is a form of human congenital myasthenia associated with point mutations in the muscle nicotinic receptor subunits. Mutations in the α, β, δ and ε subunits have all been identified, with the majority located in transmembrane domains (Ohno et al., 1995; Sine et al., 1995; Engel et al., 1996; Gomez et al., 1996; Milone et al., 1997). The information regarding the functional consequences of individual mutations in humans has been extracted from recordings from human muscle (Sine et al., 1995; Engel et al., 1996), transgenic mouse lines (Gomez et al., 1997; Gomez et al., 2002) and single-channel studies on mutated receptors (Ohno et al., 1995; Sine et al., 1995; Engel et al., 1996; Gomez et al., 1996; Milone et al., 1997), but there are limitations to each of these techniques that have impeded further progress in our understanding of SCS. Human muscle specimens must be obtained through biopsy and recordings of synaptic current decay are bound by the limitations of the voltage-clamp of large muscle. The same technical problem applies to voltage-clamp of mouse muscle; furthermore, mouse SCS mutant subunits are overexpressed in a wild-type background and are not under the control of the native regulation machinery. The bulk of the information about SCS-causing mutations comes from single-channel studies of reconstituted receptors that have given us a more detailed look at the changes in the ACh receptor gating parameters. Primarily, it has been established that altered rate constants for channel gating lead to prolonged channel openings, the presumed underpinnings of synaptic current prolongation (Sine et al., 1995; Engel et al., 1996;

Milone et al., 1997). Additionally, some of the mutations increase the sensitivity to ACh (Sine et al., 1995; Engel et al., 1996; Milone et al., 1997) as well as alter receptor desensitization kinetics (Engel et al., 1996; Milone et al., 1997). The common outcome of these functional alterations is to enhance receptor openings, which leads to the prolonged contractions and increased calcium overload underlying the human disease (Leonard et al., 1979, 1982).

The limitations of the resolution from muscle cell physiology, however, have prevented the pairing between single-channel function and synaptic current decay kinetics. My recordings from zebrafish muscle allowed me to resolve three distinct kinetic components of the synaptic current decay, whereas previous studies, even those using α-subunit mutations, have only reported biexponential decays. I was then able to match these to the burst duration of single receptors. Additionally, I investigated the consequences of the prolonged synaptic current decay using paired motor neuron-muscle recordings with the native synaptic input. Use of this system has also allowed us, for the first time, to perform *in vivo* tests to determine the mechanism of quinidine, a common treatment for patients with SCS. Finally, the basis for the unique developmental recovery of function that the *twister* model displayed was elucidated, which was the most interesting and relevant aspect to treating patients. The significant new insights obtained for each of these aspects of *twister* are addressed in the following discussion.

Synaptic current recordings of mEPC decay revealed that during the phenotypic height of the motility defect, the mEPC decay is greatly prolonged and consists of three

distinct kinetic components. Experiments in Chapter 4 demonstrated that the prolongation was not due to a secondary conductance while experiments presented in Chapter 7 demonstrated that the prolongation was not due to low AChE activity early during development. Based on these results, I proposed that the three components represented, in part, the intrinsic gating properties of different ACh receptor isoforms. The single-channel analysis of zebrafish ACh receptors presented in Chapter 5 provided support for this hypothesis; two fast gating isoforms, $\alpha\beta\delta\varepsilon$ and $\alpha\beta\delta\gamma$, an intermediate gating isoform, $\alpha_{twi}\beta\delta\varepsilon$, and a slow gating isoform, $\alpha_{twi}\beta\delta\gamma$ were identified. Receptors with conductance and burst-durations matching the reconstituted receptors were directly identified on zebrafish muscle.

Properties of heterotypic channels

The analysis of *twister* mEPC decay kinetics distinctly revealed three kinetic components, yet 8 possible ACh receptor isoforms are predicted to be present at the synapse. The possible isoforms include 4 homotypic channels (two α_{wt} and two α_{twi} subunits with γ or ε) as well as 4 heterotypic channel types (one α_{wt} and one α_{twi} subunit with γ or ε). While I was able to directly measure the burst-duration of homotypic receptors through reconstitution in oocytes, I could not selectively express heterotypic channels for similar analysis. Concatenation of subunit RNA to force specific subunit associations in the desired position is an unreliable approach, as unspecified receptor isoforms still form by excluding subunits of a concatenated protein (PB personal communication).

Although I lack direct experimental measurements of the properties of heterotypic receptors, I have some clues regarding their function. First, I believe that heterotypic channels are functional, since two mutant α subunits are indeed able to form a functional receptor. Secondly, heterotypic isoforms likely have burst-durations that match either the wild-type or homotypic isoform. In a handful of single-channel studies not presented, I co-expressed α_{WT} and α_{twi} subunits (with β, δ and either ε or γ) in oocytes and found only single-channel events that matched the properties of the homotypic isoforms. Additionally, all of the single-channel events on *twister* muscle also matched well to the properties of homotypic isoforms. Whether heterotypic receptors adopt gating characteristics of wild-type, or mutant receptors, however, is not clear from these single-channel recordings. The fractional contribution of each receptor isoform to the synaptic current, however, may suggest that heterotypic receptors adopt either gating characteristics. The simplest case is to consider the synaptic decay in recovered *twister* animals. After the disappearance of the slow component at 120 hpf, the mEPC decay is composed equally of τ_f (0.5) and τ_i (0.5). If I assume 1) that the γ subunit containing AChRs are absent from the NMJ by 120 hpf 2) that all receptor isoforms are expressed in equal proportions (which I have not established) and 3) that receptors only open once following the release of a quantum of transmitter, then this ratio suggests that half of the heterotypic forms gate similarly to wild-type receptors and half gate similarly to mutant receptors. If all heterotypic channels gated similarly to wild-type channels, I might expect the fractional contribution of τ_f to be larger (perhaps 0.75) and the inverse fractional contribution should occur if all heterotypic channels

gated similarly to mutant receptors. This conspicuously even partitioning of heterotypic channels gating as either wild-type or mutant receptors raises the possibility that the exact position of the mutant α-subunit within the channel (either between β and δ or γ/ε and β) contributes to the gating characteristics. However, given the aforementioned assumptions and the limitations of this analysis, however, the gating characteristics of heterotypic channels remain an open question.

Enhanced twister receptor opening

The most detrimental consequence of the *twister* mutation to receptor function is an increase in the open probability (P_o) for the ACh receptor. Receptors rapidly fluctuate between open and closed states, on sub-millisecond timescales, and the average time spent in the open state over a period of time can be quantified as P_o. An increase in P_o can result from an individual opening event that is longer in duration, or from more frequent openings. Experiments in Chapter 5 demonstrated that the mean burst-duration for an individual opening was increased for both the $\alpha_{twi}\beta\delta\gamma$ and $\alpha_{twi}\beta\delta\varepsilon$ receptors. This is not surprising, because of both the location and nature of the *twister* mutation. Leucine 258 is a highly conserved residue that is located in the M2 alpha helix. The substitution by proline, an amino acid with a cyclic side chain, is expected to disrupt the secondary structure of alpha-helices by introducing kinks and straining torsional rotation (von Heijne, 1991). Because rotation of M2 helices is thought to be important in channel gating (Miyazawa et al., 2003), altering the M2 helix structure

would be expected to alter channel function either by stabilizing the open state, or destabilizing the closed state.

A second possibility is more frequent receptor opening. Single-channel measurements in Chapters 5 and 6 were not able to resolve individual closures that are briefer than 200 μs, due to the limitations imposed by my sampling frequency of 5 kHz. Therefore, it remains a possibility that I am missing brief closures in my single-channel records. Persistent reopening can result from either a receptor that has increased sensitivity to agonist, or a receptor that associates more tightly with agonist. To sort out these two possibilities, I tested several predications that were set forth by ion channel biophysicists who investigate the gating equilibrium of the ACh receptor. The concept of gating equilibrium defines the relationship between the association of the agonist and the receptor (dissociation constant) and the transition of the receptor between the open and closed states (α and β). The MWC model predicts that the ACh receptor can transition to the open state in the absence of ligand (unliganded equilibrium E_0) or when two agonist molecules are associated (di-liganded equilibrium E_2). The functional hallmarks of ACh receptor mutations that alter E_0 are a left-shifted dose-response curve, an increased sensitivity of weak agonists such as choline, and an increased frequency of spontaneous opening. Each of these properties was observed for the *twister* mutant channels as presented in Chapter 6. Taken alone, a leftward shift in the dose-response curve for an ACh receptor does not distinguish between a change in E_0 or E_2, because the open conformation is the high affinity state for the AChR. A receptor with a larger P_o (for example due to a change in α or β) will also have a higher apparent affinity for

ACh. In fact, experiments performed by Steve Sine using competitive binding assays on SCS mutations demonstrated this increased apparent affinity (Sine et al., 1995). However, gating by choline and spontaneous openings are not predicted by changes in E_2. This is because for choline, the concentration can be increased to levels that force occupation of the ACh binding site, but choline binding still cannot provide enough energy to transition the receptor into the open conformation. The same is true for spontaneous openings, which can only arise if the free energy difference between the open and closed conformations is lowered. Therefore, I favor a change in E_0, which is consistent with other studies of ACh receptor mutations (Jadey et al., 2011).

The enhanced sensitivity to ACh points towards an explanation for why the mean burst-duration of mutant channels was generally slightly briefer than the corresponding time constants for the synaptic decay. The enhanced sensitivity to ACh raises the possibility that mutant receptors may open multiple times in response to the release of a single quantum of transmitter. Estimates have placed the upper limit of acetylcholine in the range of 300-500 μM for frog neuromuscular junction (Kuffler and Yoshikami, 1975; Land et al., 1980) while the lower limit has not been experimentally determined. It is believed, however, that for wild-type NMJs, the ambient concentration is insufficient to activate the ACh receptor and my dose-response estimates suggest that this threshold is between 50-100 nM. To abolish ACh activation for the mutant $\alpha_{twi}\beta\delta\gamma$ and $\alpha_{twi}\beta\delta\varepsilon$ ACh receptors, however, my estimates suggest that ACh must be lowered to 1 nM. Without an accurate measurement of the lower limit of synaptic cleft ACh concentration, the extent of ACh receptor activation by residual ACh remains unknown.

Measurements of ambient glutamate concentration in hippocampal slices placed the lower limit of glutamate at 25 nM (Herman and Jahr, 2007). Although the mechanism of glutamate removal at central synapses differs from that of the NMJ, this concentration is sufficiently low to prevent receptor activation. If the ambient ACh concentration were similar to that of glutamate, it would result in significant activation of both homotypic *twister* isoforms. An additional source of receptor re-opening could be the gating of $\alpha_{twi}\beta\delta\gamma$ and $\alpha_{twi}\beta\delta\varepsilon$ AChRs by choline, a hydrolysis product of ACh (Zhou et al., 1999). This possibility is quite speculative, however, considering that I tested a choline concentration (10 mM) that is likely to be much larger than found *in vivo.* Therefore, the dose-response properties to choline would need to be determined in order to further examine the possibility of choline gating of mutant receptors at the synapse.

A second explanation for the difference between the mean burst-duration for the single AChR and the time constant of the synaptic decay may result from a limitation imposed by the time constant of the voltage clamp. My estimate for this value is between 286 and 530 μs (see Materials and Methods), which is similar to the fast component of the synaptic decay for 120 *twi* $^{+/-}$ fish as well as the single exponential decay of 120 wild-type fish (Chapter 7). Therefore, due to this technical limitation, my measurement of the synaptic current decay time constant may be an overestimation in these cells.

γ subunit at the heart of twister recovery

My evidence shows that synaptic current decays are accelerated throughout development and this acceleration is correlated with the phenotypic recovery process. The acceleration is due to a selective loss of the slow component of the decay, which I believe to be current flow through the $\alpha_{twi}\beta\delta\gamma$ receptor. I have identified several aberrant properties of the $\alpha_{twi}\beta\delta\gamma$ AChR that likely make it problematic for normal neuromuscular communication. First, the increased mean burst-duration results in persistent muscle depolarization as well as increased calcium entry into the muscle cell. Second, $\alpha_{twi}\beta\delta\gamma$ AChRs open in response to much lower concentrations of ACh than wild-type counterparts. Third, these receptors are also sensitive to choline, raising the possibility that the hydrolysis products of ACh can reactivate mutant receptors. Finally, a large persistent inward current was observed in oocytes expressing $\alpha_{twi}\beta\delta\gamma$ receptors which was due to spontaneous opening. This property could prolong the repolarization phase by adding an additional leak current to the muscle cell. Several attempts were made to test this hypothesis by profusion of quinidine directly onto muscle cells, but baseline fluctuations and spontaneous vesicle fusion made the results difficult to interpret.

My strongest evidence that $\alpha_{twi}\beta\delta\gamma$ is causal to the motility defect and that the developmental loss of the homotypic embryonic receptor isoform leads to functional recovery came from experiments employing the γ subunit morpholino. γ morpholino injection resulted in accelerated synaptic current decays, and improved swimming

behavior which was quantitated with the motion analysis software. Correspondingly, it reduced the persistent depolarization in the EPP that I observed under current clamp, potentially allowing relaxation of the muscle. Still, however, there may be other factors that contribute to functional recovery in addition to the loss of γ subunit, such as the characteristics of the muscle action potential. Enhanced repolarization could diminish the effect of the EPP, accelerate recovery of sodium channels from inactivation, and lead to higher frequencies of muscle action potential generation. The characteristics of *twister* muscle action potentials (in the absence of EPPs) were not examined in this work.

twister insights into SCS treatment

In addition to a more detailed understanding of the dysfunction caused by ACh receptor mutations, the *twister* model has given us insights to the treatments for slow channel syndrome. The evidence that open-channel blockers, such as quinidine, could be used as a treatment for SCS was based on single-channel studies (Fukudome et al., 1998). These drugs have been administered to SCS patients and proved to be an effective treatment (Harper and Engel, 1998). The exact effects of quinidine on synaptic transmission, however, has remained speculative. *Twister* has provided the first *in vivo* evidence of synaptic current acceleration by quinidine, and demonstrated that the intermediate and slow components that are introduced by mutant receptors can be specifically abolished with the drug, resulting in wild-type like kinetics.

Similar to other human SCS mutations, the L258P mutation showed frequent spontaneous openings; it was surprising, however, that these openings resulted in a standing current in oocytes that represented such a large portion (15%) of the total possible current. These experiments raise the possibility that a persistent inward current is also present in the muscle cell, pointing to an additional mechanism of calcium entry in addition to prolonged synaptic currents. That spontaneously open receptors are blocked with quinidine highlights a previously unappreciated aspect of this treatment that likely plays a role in its remedial effects.

Finally, and perhaps most importantly, *twister* has opened up new possibilities as to the existence and interpretation of human myasthenic disorders. *Twister* is a model for SCS as it is dominantly inherited and occurs in a subunit frequently ascribed to the disease. However, patients with SCS have not been shown to naturally recover normal function, rather symptoms such as muscle fatigue and damage become exacerbated with time. Functional recovery is unique to Escobar syndrome, a recessive myasthenic disorder involving mutations in the γ subunit; not surprisingly, recovery is to be expected on the basis of the developmental γ to ε switch. It stands out, however, that no dominantly inherited, gain-of-function mutations have been ascribed to the γ subunit. Multiple gain-of-function mutations have been found for SCS patients in all subunits except for γ. Two explanations for this observation are possible, the first is that gain-of-function γ subunit mutations are lethal, while the second is that they were missed due to recovery.

Twister is a unique model for neuromuscular disease, in that it is a genetic model for SCS because it contains a gain of function mutation in the α subunit, yet phenotypically behaves similar to Escobar Syndrome, which has been ascribed exclusively to mutations of γ subunit. The recovery we see in *twister* reveals the possibility that there are forms of SCS that benefit from the γ/ε switch that are not due to mutations in the γ subunit. It also points towards the potential existence of previously unrecognized recovering forms of SCS in the human population. It is likely that these cases would be missed, or potentially diagnosed as an alternate form of myasthenia, such as autoimmune. Although Escobar patients recover, the long lasting impacts of the early receptor dysfunction, such as scoliosis, can be severe. Therefore, like SCS patients, Escobar patients would likely benefit from quinidine therapy as well as from prenatal screening for mutations in each of the ACh receptor subunits. Quinidine treatment *in utero* may provide a similar therapeutic improvement seen for SCS treatment of children, and diminish the long-term effects of early neuromuscular dysfunction.

REFERENCES

Adams PR (1975) An analysis of the dose-response curve at voltage-clamped frog-endplates. Pflugers Arch 360:145-153.

Adams PR (1981) Acetylcholine receptor kinetics. J Membr Biol 58:161-174.

Akabas MH, Kaufmann C, Archdeacon P, Karlin A (1994) Identification of acetylcholine receptor channel-lining residues in the entire M2 segment of the alpha subunit. Neuron 13:919-927.

Anderson CR, Stevens CF (1973) Voltage-clamp analysis of acetylcholine produced end-plate current fluctuations at frog neuromuscular junction. J Physiol 235:655-691.

Auerbach A (2003) Life at the top: the transition state of AChR gating. Sci STKE 2003:re11.

Auerbach A (2010) The gating isomerization of neuromuscular acetylcholine receptors. J Physiol 588:573-586.

Auerbach A (2012) Thinking in cycles: MWC is a good model for acetylcholine receptor-channels. J Physiol 590:93-98.

Blount P, Merlie JP (1989) Molecular basis of the two nonequivalent ligand binding sites of the muscle nicotinic acetylcholine receptor. Neuron 3:349-357.

Bouzat C, Barrantes FJ (1997) Assigning functions to residues in the acetylcholine receptor channel region (review). Mol Membr Biol 14:167-177.

Brehm P, Kidokoro Y, Moody-Corbett F (1984) Acetylcholine receptor channel properties during development of Xenopus muscle cells in culture. J Physiol 357:203-217.

Brehm P, Yeh E, Patrick J, Kidokoro Y (1983) Metabolism of acetylcholine receptors on embryonic amphibian muscle. J Neurosci 3:101-107.

Brisson A, Unwin PN (1985) Quaternary structure of the acetylcholine receptor. Nature 315:474-477.

Buckingham SD, Ali DW (2004) Sodium and potassium currents of larval zebrafish muscle fibres. J Exp Biol 207:841-852.

Budick SA, O'Malley DM (2000) Locomotor repertoire of the larval zebrafish: swimming,

turning and prey capture. J Exp Biol 203:2565-2579.

Burgess HA, Granato M (2007) Modulation of locomotor activity in larval zebrafish during light adaptation. J Exp Biol 210:2526-2539.

Buss RR, Drapeau P (2001) Synaptic drive to motoneurons during fictive swimming in the developing zebrafish. J Neurophysiol 86:197-210.

Changeux JP (2011) Allostery and the Monod-Wyman-Changeux Model After 50 Years. Annu Rev Biophys.

Colquhoun D, Sakmann B (1981) Fluctuations in the microsecond time range of the current through single acetylcholine receptor ion channels. Nature 294:464-6

Colquhoun D, Sakmann B (1985) Fast events in single-channel currents activated by acetylcholine and its analogues at the frog muscle end-plate. J Physiol 369:501-57

Croxen R, Hatton C, Shelley C, Brydson M, Chauplannaz G, Oosterhuis H, Vincent A, Newsom-Davis J, Colquhoun D, Beeson D (2002) Recessive inheritance and variable penetrance of slow-channel congenital myasthenic syndromes. Neurology 59:162-168.

Damle VN, Karlin A (1978) Affinity labeling of one of two alpha-neurotoxin binding sites in acetylcholine receptor from Torpedo californica. Biochemistry 17:2039-2045.

Decker ER, Dani JA (1990) Calcium permeability of the nicotinic acetylcholine receptor: the single-channel calcium influx is significant. J Neurosci 10:3413-3420.

Del Castillo J, Katz B (1955) On the localization of acetylcholine receptors. J Physiol 128:157-181.

Del Castillo J, Katz B (1957) Interaction at end-plate receptors between different choline derivatives. Proc R Soc Lond B Biol Sci 146:369-381.

Devoto SH, Melancon E, Eisen JS, Westerfield M (1996) Identification of separate slow and fast muscle precursor cells in vivo, prior to somite formation. Development 122:3371-3380.

Dionne VE, Steinbach JH, Stevens CF (1978) An analysis of the dose-response relationship at voltage-clamped frog neuromuscular junctions. J Physiol 281:421-444.

Drapeau P, Buss RR, Ali DW, Legendre P, Rotundo RL (2001) Limits to the development

of fast neuromuscular transmission in zebrafish. J Neurophysiol 86:2951-2956.

Eccles JC, Jaeger JC (1958) The relationship between the mode of operation and the dimensions of the junctional regions at synapses and motor end-organs. Proc R Soc Lond B Biol Sci 148:38-56.

Eccles JC, Katz B, Kuffler SW (1941a) Nature of the “endplate potential” in curarized muscle. J Neurophysiol. 4:362-387

Eccles JC, Katz B, Kuffler SW (1941b) Electric potential changes accompanying neuro-musclar transmission. Biol Symp. 3:349-370

Eccles JC, Kuffler SW (1941) Inititation of muscle impulses at neuro-muscular junction. J Neurophysiol. 4:402-417

Engel AG, Hutchinson DO, Nakano S, Murphy L, Griggs RC, Gu Y, Hall ZW, Lindstrom J (1993) Myasthenic syndromes attributed to mutations affecting the epsilon subunit of the acetylcholine receptor. Ann N Y Acad Sci 681:496-508.

Engel AG, Lambert EH, Mulder DM, Torres CF, Sahashi K, Bertorini TE, Whitaker JN (1982) A newly recognized congenital myasthenic syndrome attributed to a prolonged open time of the acetylcholine-induced ion channel. Ann Neurol 11:553-569.

Engel AG, Ohno K, Milone M, Wang HL, Nakano S, Bouzat C, Pruitt JN, 2nd, Hutchinson DO, Brengman JM, Bren N, Sieb JP, Sine SM (1996) New mutations in acetylcholine receptor subunit genes reveal heterogeneity in the slow-channel congenital myasthenic syndrome. Hum Mol Genet 5:1217-1227.

Engel AG, Ohno K, Sine SM (2003) Sleuthing molecular targets for neurological diseases at the neuromuscular junction. Nat Rev Neurosci 4:339-352.

Feng TP (1937) Studies on the neuro-muscular junction VIII. The localized contraction around N-M junction and the blocking of contraction waves due to nerve stimulation. Chin J Physiol. 11:331-370.

Feng TP, Shen SC (1937) Studies on the neuro-muscular junction III. The contracture in eserized muscle produced by nerve stimulation. Chin J Physiol. 11:51-70.

Feng TP (1940) Studies on the neuro-muscular junction XVIII. The local potentials around N-m Junctions induced by single and multiple volleys. Chin J Physiol. 15:367-404.

Fischbach GD, Schuetze SM (1980) A post-natal decrease in acetylcholine channel open time at rat end-plates. J Physiol 303:125-137.

Fukudome T, Ohno K, Brengman JM, Engel AG (1998) AChR channel blockade by quinidine sulfate reduces channel open duration in the slow-channel congenital myasthenic syndrome. Ann N Y Acad Sci 841:199-202.

Gage PW, Armstrong CM (1968) Miniature end-plate currents in voltage-clamped muscle fibre. Nature 218:363-365.

Galzi JL, Devillers-Thiery A, Hussy N, Bertrand S, Changeux JP, Bertrand D (1992) Mutations in the channel domain of a neuronal nicotinic receptor convert ion selectivity from cationic to anionic. Nature 359:500-505.

Gomez CM, Maselli R, Gammack J, Lasalde J, Tamamizu S, Cornblath DR, Lehar M, McNamee M, Kuncl RW (1996) A beta-subunit mutation in the acetylcholine receptor channel gate causes severe slow-channel syndrome. Ann Neurol 39:712-723.

Gomez CM, Maselli R, Gundeck JE, Chao M, Day JW, Tamamizu S, Lasalde JA, McNamee M, Wollmann RL (1997) Slow-channel transgenic mice: a model of postsynaptic organellar degeneration at the neuromuscular junction. J Neurosci 17:4170-4179.

Gomez CM, Maselli RA, Groshong J, Zayas R, Wollmann RL, Cens T, Charnet P (2002) Active calcium accumulation underlies severe weakness in a panel of mice with slow-channel syndrome. J Neurosci 22:6447-6457.

Groshong JS, Spencer MJ, Bhattacharyya BJ, Kudryashova E, Vohra BP, Zayas R, Wollmann RL, Miller RJ, Gomez CM (2007) Calpain activation impairs neuromuscular transmission in a mouse model of the slow-channel myasthenic syndrome. J Clin Invest 117:2903-2912.

Grosman C, Auerbach A (2000a) Asymmetric and independent contribution of the second transmembrane segment 12' residues to diliganded gating of acetylcholine receptor channels: a single-channel study with choline as the agonist. J Gen Physiol 115:637-651.

Grosman C, Auerbach A (2000b) Kinetic, mechanistic, and structural aspects of unliganded gating of acetylcholine receptor channels: a single-channel study of second transmembrane segment 12' mutants. J Gen Physiol 115:621-635.

Harper CM, Engel AG (1998) Quinidine sulfate therapy for the slow-channel congenital myasthenic syndrome. Ann Neurol 43:480-484.

Herman MA, Jahr CE (2007) Extracellular glutamate concentration in hippocampal slice.

J Neurosci 27:9736-9741.

Hess A (1970) Vertebrate slow muscle fibers. Physiol Rev 50:40-62.

Hoffmann K, Muller JS, Stricker S, Megarbane A, Rajab A, Lindner TH, Cohen M, Chouery E, Adaimy L, Ghanem I, Delague V, Boltshauser E, Talim B, Horvath R, Robinson PN, Lochmuller H, Hubner C, Mundlos S (2006) Escobar syndrome is a prenatal myasthenia caused by disruption of the acetylcholine receptor fetal gamma subunit. Am J Hum Genet 79:303-312.

Imoto K, Methfessel C, Sakmann B, Mishina M, Mori Y, Konno T, Fukuda K, Kurasaki M, Bujo H, Fujita Y, et al. (1986) Location of a delta-subunit region determining ion transport through the acetylcholine receptor channel. Nature 324:670-674.

Jackson MB (1984) Spontaneous openings of the acetylcholine receptor channel. Proc Natl Acad Sci U S A 81:3901-3904.

Jackson MB (1986) Kinetics of unliganded acetylcholine receptor channel gating. Biophys J 49:663-672.

Jackson MB (1989) Perfection of a synaptic receptor: kinetics and energetics of the acetylcholine receptor. Proc Natl Acad Sci U S A 86:2199-2203.

Jackson MB, Imoto K, Mishina M, Konno T, Numa S, Sakmann B (1990) Spontaneous and agonist-induced openings of an acetylcholine receptor channel composed of bovine muscle alpha-, beta- and delta-subunits. Pflugers Arch 417:129-135.

Jadey SV, Purohit P, Bruhova I, Gregg TM, Auerbach A (2011) Design and control of acetylcholine receptor conformational change. Proc Natl Acad Sci U S A 108:4328-4333.

Karlin A (2002) Emerging structure of the nicotinic acetylcholine receptors. Nat Rev Neurosci 3:102-114.

Karlin A, Akabas MH (1995) Toward a structural basis for the function of nicotinic acetylcholine receptors and their cousins. Neuron 15:1231-1244.

Katz B (1996) Neural transmitter release: from quantal secretion to exocytosis and beyond. The Fenn Lecture. J Neurocytol 25:677-686.

Katz B, Miledi R (1971) Further observations on acetylcholine noise. Nat New Biol 232:124-126.

Katz B, Miledi R (1972) The statistical nature of the acetycholine potential and its

molecular components. J Physiol 224:665-699.

Katz B, Thesleff S (1957) A study of the desensitization produced by acetylcholine at the motor end-plate. J Physiol 138:63-80.

Kimmel CB, Patterson J, Kimmel RO (1974) The development and behavioral characteristics of the startle response in the zebra fish. Dev Psychobiol 7:47-60.

Kuffler SW, Yoshikami D (1975) The number of transmitter molecules in a quantum: an estimate from iontophoretic application of acetylcholine at the neuromuscular synapse. J Physiol 251:465-482.

Kullberg RW, Brehm P, Steinbach JH (1981) Nonjunctional acetylcholine receptor channel open time decreases during development of Xenopus muscle. Nature 289:411-413.

Kullberg RW, Mikelberg FS, Cohen MW (1980) Contribution of cholinesterase to developmental decreases in the time course of synaptic potentials at an amphibian neuromuscular junction. Dev Biol 75:255-267.

Land BR, Harris WV, Salpeter EE, Salpeter MM (1984) Diffusion and binding constants for acetylcholine derived from the falling phase of miniature endplate currents. Proc Natl Acad Sci U S A 81:1594-1598.

Land BR, Salpeter EE, Salpeter MM (1980) Acetylcholine receptor site density affects the rising phase of miniature endplate currents. Proc Natl Acad Sci U S A 77:3736-3740.

Land BR, Salpeter EE, Salpeter MM (1981) Kinetic parameters for acetylcholine interaction in intact neuromuscular junction. Proc Natl Acad Sci U S A 78:7200-7204.

Lefebvre JL, Ono F, Puglielli C, Seidner G, Franzini-Armstrong C, Brehm P, Granato M (2004) Increased neuromuscular activity causes axonal defects and muscular degeneration. Development 131:2605-2618.

Leonard JP, Salpeter MM (1979) Agonist-induced myopathy at the neuromuscular junction is mediated by calcium. J Cell Biol 82:811-819.

Leonard JP, Salpeter MM (1982) Calcium-mediated myopathy at neuromuscular junctions of normal and dystrophic muscle. Exp Neurol 76:121-138.

Leonard RJ, Labarca CG, Charnet P, Davidson N, Lester HA (1988) Evidence that the M2 membrane-spanning region lines the ion channel pore of the nicotinic receptor.

Science 242:1578-1581.

Liu DW, Westerfield M (1988) Function of identified motoneurones and co-ordination of primary and secondary motor systems during zebra fish swimming. J Physiol 403:73-89.

Liu KS, Fetcho JR (1999) Laser ablations reveal functional relationships of segmental hindbrain neurons in zebrafish. Neuron 23:325-335.

Luna VM, Brehm P (2006) An electrically coupled network of skeletal muscle in zebrafish distributes synaptic current. J Gen Physiol 128:89-102.

Magleby KL, Stevens CF (1972 a) The effect of voltage on the time course of end-plate currents. J Physiol 223:151-171.

Magleby KL, Stevens CF (1972 b) A quantitative description of end-plate currents. J Physiol 223:173-197.

Michler A, Sakmann B (1980) Receptor stability and channel conversion in the subsynaptic membrane of the developing mammalian neuromuscular junction. Dev Biol 80:1-17.

Milone M, Wang HL, Ohno K, Fukudome T, Pruitt JN, Bren N, Sine SM, Engel AG (1997) Slow-channel myasthenic syndrome caused by enhanced activation, desensitization, and agonist binding affinity attributable to mutation in the M2 domain of the acetylcholine receptor alpha subunit. J Neurosci 17:5651-5665.

Mishina M, Takai T, Imoto K, Noda M, Takahashi T, Numa S, Methfessel C, Sakmann B (1986) Molecular distinction between fetal and adult forms of muscle acetylcholine receptor. Nature 321:406-411.

Miyazawa A, Fujiyoshi Y, Unwin N (2003) Structure and gating mechanism of the acetylcholine receptor pore. Nature 423:949-955.

Mongeon R, Walogorsky M, Urban J, Mandel G, Ono F, Brehm P (2011) An acetylcholine receptor lacking both gamma and epsilon subunits mediates transmission in zebrafish slow muscle synapses. J Gen Physiol 138:353-366.

Monod J, Wyman J, Changeux JP (1965) On the Nature of Allosteric Transitions: A Plausible Model. J Mol Biol 12:88-118.

Muller UK, van Leeuwen JL (2004) Swimming of larval zebrafish: ontogeny of body waves and implications for locomotory development. J Exp Biol 207:853-868.

Nakanishi S, Masu M, Bessho Y, Nakajima Y, Hayashi Y, Shigemoto R (1994) Molecular diversity of glutamate receptors and their physiological functions. EXS 71:71-80.

Naranjo D, Brehm P (1993) Modal shifts in acetylcholine receptor channel gating confer subunit-dependent desensitization. Science 260:1811-1814.

Neher E, Sakmann B (1976) Single-channel currents recorded from membrane of denervated frog muscle fibres. Nature 260:799-802.

Noda M, Takahashi H, Tanabe T, Toyosato M, Kikyotani S, Furutani Y, Hirose T, Takashima H, Inayama S, Miyata T, Numa S (1983a) Structural homology of Torpedo californica acetylcholine receptor subunits. Nature 302:528-532.

Noda M, Takahashi H, Tanabe T, Toyosato M, Kikyotani S, Hirose T, Asai M, Takashima H, Inayama S, Miyata T, Numa S (1983b) Primary structures of beta- and delta-subunit precursors of Torpedo californica acetylcholine receptor deduced from cDNA sequences. Nature 301:251-255.

O'Malley DM, Kao YH, Fetcho JR (1996) Imaging the functional organization of zebrafish hindbrain segments during escape behaviors. Neuron 17:1145-1155.

Ohno K, Hutchinson DO, Milone M, Brengman JM, Bouzat C, Sine SM, Engel AG (1995) Congenital myasthenic syndrome caused by prolonged acetylcholine receptor channel openings due to a mutation in the M2 domain of the epsilon subunit. Proc Natl Acad Sci U S A 92:758-762.

Ohno K, Wang HL, Milone M, Bren N, Brengman JM, Nakano S, Quiram P, Pruitt JN, Sine SM, Engel AG (1996) Congenital myasthenic syndrome caused by decreased agonist binding affinity due to a mutation in the acetylcholine receptor epsilon subunit. Neuron 17:157-170.

Ono F, Higashijima S, Shcherbatko A, Fetcho JR, Brehm P (2001) Paralytic zebrafish lacking acetylcholine receptors fail to localize rapsyn clusters to the synapse. J Neurosci 21:5439-5448.

Oosterhuis HJ, Newsom-Davis J, Wokke JH, Molenaar PC, Weerden TV, Oen BS, Jennekens FG, Veldman H, Vincent A, Wray DW, et al. (1987) The slow channel syndrome. Two new cases. Brain 110 (Pt 4):1061-1079.

Owens J, Kullberg R, Brehm P (1993) Contributions of the gamma and epsilon subunit family to nicotinic acetylcholine receptor function. Receptors Channels 1:173-180.

Paradiso K, Brehm P (1998) Long-term desensitization of nicotinic acetylcholine

receptors is regulated via protein kinase A-mediated phosphorylation. J Neurosci 18:9227-9237.

Pongs O, Schwarz JR (2010) Ancillary subunits associated with voltage-dependent K+ channels. Physiol Rev 90:755-796.

Preuss T, Osei-Bonsu PE, Weiss SA, Wang C, Faber DS (2006) Neural representation of object approach in a decision-making motor circuit. J Neurosci 26:3454-3464.

Purohit P, Auerbach A (2009) Unliganded gating of acetylcholine receptor channels. Proc Natl Acad Sci U S A 106:115-120.

Reynolds JA, Karlin A (1978) Molecular weight in detergent solution of acetylcholine receptor from Torpedo californica. Biochemistry 17:2035-2038.

Saint-Amant L, Drapeau P (1998) Time course of the development of motor behaviors in the zebrafish embryo. J Neurobiol 37:622-632.

Sakmann B, Brenner HR (1978) Change in synaptic channel gating during neuromuscular development. Nature 276:401-402.

Sanger AM, Stoiber W (2001) Muscle fiber diversity and plasticity. Fish Physiology Series. 18:187-250.

Siegelbaum SA, Trautmann A, Koenig J (1984) Single acetylcholine-activated channel currents in developing muscle cells. Dev Biol 104:366-379.

Sigworth FJ, Sine SM (1987) Data transformations for improved display and fitting of single-channel dwell time histograms. Biophys J 52:1047-1054.

Sine SM, Engel AG (2006) Recent advances in Cys-loop receptor structure and function. Nature 440:448-455.

Sine SM, Ohno K, Bouzat C, Auerbach A, Milone M, Pruitt JN, Engel AG (1995) Mutation of the acetylcholine receptor alpha subunit causes a slow-channel myasthenic syndrome by enhancing agonist binding affinity. Neuron 15:229-239.

Sine SM, Quiram P, Papanikolaou F, Kreienkamp HJ, Taylor P (1994) Conserved tyrosines in the alpha subunit of the nicotinic acetylcholine receptor stabilize quaternary ammonium groups of agonists and curariform antagonists. J Biol Chem 269:8808-8816.

Steinbach JH (1989) Structural and functional diversity in vertebrate skeletal muscle nicotinic acetylcholine receptors. Annu Rev Physiol 51:353-365.

Stephenson RP (1956) A modification of receptor theory. Br J Pharmacol Chemother 11:379-393.

Takai T, Noda M, Mishina M, Shimizu S, Furutani Y, Kayano T, Ikeda T, Kubo T, Takahashi H, Takahashi T, et al. (1985) Cloning, sequencing and expression of cDNA for a novel subunit of acetylcholine receptor from calf muscle. Nature 315:761-764.

Takeuchi A, Takeuchi N (1959) Active phase of frog's end-plate potential. J Neurophysiol 22:395-411.

Tang R, Dodd A, Lai D, McNabb WC, Love DR (2007) Validation of zebrafish (Danio rerio) reference genes for quantitative real-time RT-PCR normalization. Acta Biochim Biophys Sin (Shanghai) 39:384-390.

Thorsen DH, Cassidy JJ, Hale ME (2004) Swimming of larval zebrafish: fin-axis coordination and implications for function and neural control. J Exp Biol 207:4175-4183.

van Eeden FJ, Granato M, Odenthal J, Haffter P (1999) Developmental mutant screens in the zebrafish. Methods Cell Biol 60:21-41.

Villarroel A, Herlitze S, Koenen M, Sakmann B (1991) Location of a threonine residue in the alpha-subunit M2 transmembrane segment that determines the ion flow through the acetylcholine receptor channel. Proc Biol Sci 243:69-74.

von Heijne G (1991) Proline kinks in transmembrane alpha-helices. J Mol Biol 218:499-503.

Wang HL, Auerbach A, Bren N, Ohno K, Engel AG, Sine SM (1997) Mutation in the M1 domain of the acetylcholine receptor alpha subunit decreases the rate of agonist dissociation. J Gen Physiol 109:757-766.

Wen H, Brehm P (2005) Paired motor neuron-muscle recordings in zebrafish test the receptor blockade model for shaping synaptic current. J Neurosci 25:8104-8111.

Westerfield M, Liu DW, Kimmel CB, Walker C (1990) Pathfinding and synapse formation in a zebrafish mutant lacking functional acetylcholine receptors. Neuron 4:867-874.

Wilson GG, Karlin A (1998) The location of the gate in the acetylcholine receptor channel. Neuron 20:1269-1281.

Wisden W, Seeburg PH (1992) GABAA receptor channels: from subunits to functional

entities. Curr Opin Neurobiol 2:263-269.

Witzemann V, Barg B, Nishikawa Y, Sakmann B, Numa S (1987) Differential regulation of muscle acetylcholine receptor gamma- and epsilon-subunit mRNAs. FEBS Lett 223:104-112.

Zhou M, Engel AG, Auerbach A (1999) Serum choline activates mutant acetylcholine receptors that cause slow channel congenital myasthenic syndromes. Proc Natl Acad Sci U S A 96:10466-10471.

Zottoli SJ (1977) Correlation of the startle reflex and Mauthner cell auditory responses in unrestrained goldfish. J Exp Biol 66:243-254.